NATIONAL ENERGY TECHNOLOGY LABORATORY

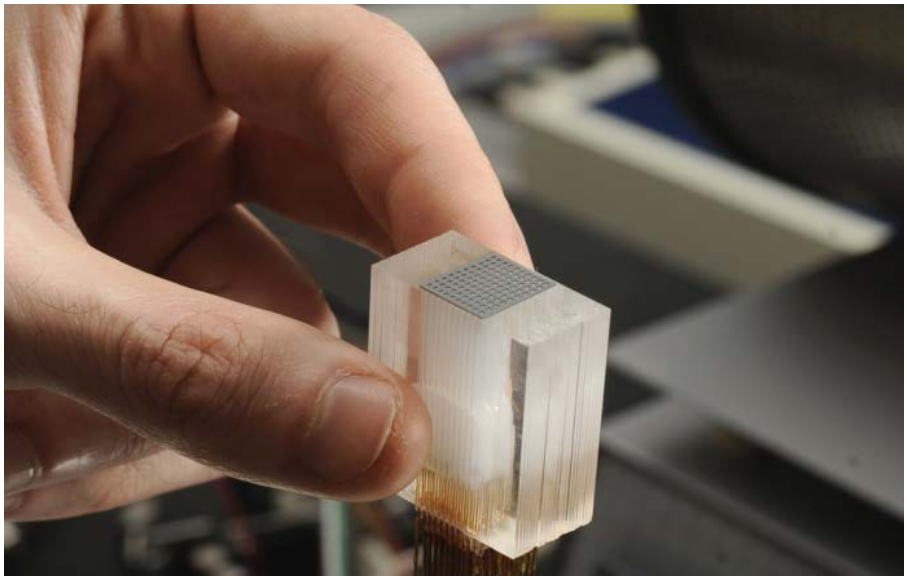

Annual Report: Advanced Energy Systems Fuels

30 September 2013

NETL Technical Report Series

U.S. DEPARTMENT OF ENERGY

Office of Fossil Energy

NETL-TRS-Fuels-2013

Disclaimer

This report was prepared as an account of work sponsored by an agency of the United States Government. Neither the United States Government nor any agency thereof, nor any of their employees, makes any warranty, express or implied, or assumes any legal liability or responsibility for the accuracy, completeness, or usefulness of any information, apparatus, product, or process disclosed, or represents that its use would not infringe privately owned rights. Reference therein to any specific commercial product, process, or service by trade name, trademark, manufacturer, or otherwise does not necessarily constitute or imply its endorsement, recommendation, or favoring by the United States Government or any agency thereof. The views and opinions of authors expressed therein do not necessarily state or reflect those of the United States Government or any agency thereof.

Cover Illustration: Multi-channel reactor array for measuring catalytic reactivity across the surface of a CSAF with a resolution of 100m.

Suggested Citation: Dirk Link, Technical Coordinator, Bryan Morreale, Focus Area Lead, Fuels Annual Report, NETL-TRS-Fuels-2103, NETL Technical Report Series, U.S. Department of Energy, National Energy Technology Laboratory, Pittsburgh, PA, 2013, p 62.

An electronic version of this report has been uploaded to the Office of Science, Technology, and Industry web site at: http://www.osti.gov/bridge

Annual Report: Advanced Energy Systems Fuels

Office of Research and Development, National Energy Technology Laboratory

NETL-TRS-Fuels-2013

30 September 2013

NETL Contacts:

Dirk Link, Technical Coordinator

Bryan Morreale, Focus Area Lead

Table of Contents

1.0 Executive Summary 1
2.0 Technology Highlights and Key Results 6
3.0 Conclusion 60
4.0 Technology Transfer 61
5.0 References 62

List of Figures

Figure 1: Mass change of the high entropy alloys and reference materials during the exposure to syngas containing various amounts of H_2S at 500°C; (a) 0% H_2S, (b) 0.01% H_2S, and (c) 0.1% H_2S. 8

Figure 2: Mass gain due to oxidation and sulfidation of $CoCrCuFeNiAl_{0.5}$ in simulated syngas containing several different levels of H_2S. The tests were conducted at 500°C for 120 hours. 8

Figure 3: XRD spectra acquired on the surface of the high entropy alloys exposed to syngas containing 0.1% H_2S at 500°C for 120 h; (a) $CoCrCuFeNiAl_{0.5}$, (b) $CoCrCuFeNiAl_{0.5}B_{0.2}$, (c) $CoCrCuFeNiAl_{0.5}B_{0.6}$, and (d) $CoCrCuFeNiAl_{0.5}B$. 9

Figure 4: SEM images of the cross sections of the $CoCrCuFeNiAl_{0.5}$ (a) and $CoCrCuFeNiAl_{0.5}B$ (b) coupons exposed to syngas containing 0.1%H_2S at 500°C for 120h. The compositions are in atomic percent. 9

Figure 5: Stability of sulfides on various metallic materials as a function of sulfur partial pressure and temperature. 11

Figure 6: Mass change of the membrane alloy coupons after 120 hour exposure to simulated syngas containing 1000 ppm H_2S at 500, 650, and 800°C. 12

Figure 7: SEM micrographs of cross-sections of CuPdMg membrane coupons exposed to the same syngas at three different temperatures. Note the extent of corrosion zone and the formation of MgS at 500°C and MgO at 650 and 800°C. 12

Figure 8: SEM micrographs of cross-sections of CuPdAl membrane coupons exposed to the same syngas at three different temperatures. No significant corrosion takes place at 500°C. Oxygen diffusion through the interdendritic regions results in oxidation of Al, first on the surface of dendrites at 650°C, then throughout the dendrites at 800°C. 12

Figure 9: Surface effects on the Cu-50Pd membrane alloy exposed to simulated syngas at 500°C, 650°C, and 800°C for 120 hours. 13

Figure 10: Membrane coupon exposure test fixture. 14

Figure 11: Preliminary results showing mass change of the membrane alloy coupons in syngas containing AsH_3, H_2Se and H_2S at 350 and 500°C. 14

Figure 12: Comparison of hydrogen flux trends for precursor coated Pd at 350°C. 15

Figure 13: SEM image of sample 50 showing corrosion free region on the sample surface. EDS shows only Pd and C in the S-free areas. 16

Figure 14: SEM image of the surface of an fcc-structured Pd-Au-Ag alloy coupon exposed during R08. 18

Figure 15: SEM image of the surface of a baseline Ta coupon exposed during R08 showing surface oxides and abundant surface particulate contamination. 19

Figure 16: General processes for Mo exchange in ZSM-5 structure with formation of $(Mo_2O_5)^{2+}$-oxo clusters according to Iglesia, et al., J. Phys. Chem. B. 1999, 103, 5787. 20

Figure 17: General processes for Mo exchange in ZSM-5 structure with formation of monomeric $(MoO_2)^{2+}$ oxo cluster bridging two acid sites and water according to Iglesia, et al., J. Phys. Chem. B. 1999, 103, 5787. 20

Figure 18: (a) The orthogonal ZSM-5 bulk structure with Pnma space group and its 12 independent locations where Si atoms can be substituted with Al. (b) Relative energies of the 48 different combinations of Al-OH-Si sites resulted upon Al substitution. Charge compensation was considered by including a proton adsorbed at a bridging oxygen site near the Al substitution. 22

Figure 19: General algorithm developed for identification and energy evaluation of Al double substitutions in ZSM-5 framework. 22

Figure 20: Relative energies of the 142 configurations of double Al substitutions in ZSM-5 structure. 23

Figure 21: Configurations of ZSM-5 with double Al site substitutions. 23

Figure 22: Effect of Si/Al ratio (SAR) on the benzene yield. 25

Figure 23: Effect of different space velocity on the benzene yield. 26

Figure 24: Ammonia TPD of three zeolite-based Mo catalyst. 26

Figure 25: Methane conversion and selectivity from MoZnM/ZSM-5 catalyst (reaction temperature 700°C and WHSV 3000 cc(STP)/g/hr) 28

Figure 26: Effect of promoters on the activity and benzene selectivity of Zn (3wt%) supported on H-ZSM-5 catalyst during MDA reaction at 700°C, 1 atm, and 3000 cc/g/h. 29

Figure 27: Effect of increasing promoters on the activity and benzene selectivity of Zn (3wt%) supported on H-ZSM-5 catalyst during MDA reaction at 700°C, 1 atm, and 3000 cc/g/h. 29

Figure 28: Plan for developing new Zn based catalyst using MWAHT method. 30

Figure 29: XRD patterns of calcined Na-ZSM-5 using different preparation methods. 30

Figure 30: Performance of Zn8-IWI catalyst under similar reaction conditions but different WHSV of (a) 3000 and (b) 6000 scc/g/h. 32

Figure 31: Comparison between the activity, benzene yield and hydrogen yield on (a) 8 and (b) 3 wt % Zn loaded on H-ZSM-5 (SAR50) under WHSV of 3000 cc/g/h 33

Figure 32: Left: XRD diffractograms for a ZSM-5 catalyst synthesized in this work (top) in comparison to a commercial ZSM-5 sample (bottom). Right: SEM images of the ZSM-5 catalyst

(big picture and top right inset) and HRTEM image showing atomically resolved zeolite structure (top left). Overall, ZSM-5 crystals with ~2-5µm size and excellent crystallinity are obtained. 34

Figure 33: Right: TEM image of ZnO nanoparticles embedded in silica shells. Left: NP size distribution (from TEM) and XRD diffractogram along with particle size calculated from Debye-Scherrer. Good agreement between two particle sizes is found..... 35

Figure 34: TEM images of ZnO@SiO_2: low weight loading (~4wt%; left) and high weight loading (~20 wt%; middle), along with HRTEM image showing lattice fringes of ZnO embedded in the silica matrix (right). 35

Figure 35: Top: SEM (top left and middle) and TEM (top right) images of ZnO@ZSM-5: The synthesis results in long-range homogeneous materials (top left), where the individual particles (in the size range of ~5 µm) are composed of stacked zeolite nanorods (top middle) into which the ZnO nanoparticles are homogeneously dispersed (top right)..... 36

Figure 36: Top left: XRD diffractograms of a commercial ZSM-5 (bottom), a pure ZSM-5 sample synthesized in this work (middle), and of a ZnO@ZSM-5 sample (top). Top right: Size distribution in the micropore range for a pure ZSM-5 and a ZnO@ZSM-5 material with 2wt% ZnO. 37

Figure 37: Pore size distribution in the mesopore size range (2-20 nm) for ZnO@ZSM-5 with ZnO NP with 3, 6, and 15 nm diameter. A direct correlation between NP size and PSD is apparent..... 38

Figure 38: First reactive evaluation of a ZnO@ZSM-5 catalysts in direct comparison to a conventionally prepared ZnO/ZSM-5 (both with 8wt% ZnO, Si:Al = 50, T=700°C). Benzene yield vs. time shows a significantly enhanced reactivity for the nanostructured catalyst..... 39

Figure 39: Stability tests for ZnO@ZSM-5: Pore size distribution before and after high-temperature exposure (1h, 700°C) to a reducing and oxidizing atmosphere, respectively. The insets show a TEM image of the sample after exposure to the reducing atmosphere, and the ZnO weight loading (determined via EDX) before and after the two treatments. 39

Figure 40: Schematic of methane conversion testing using a membrane (disc) reactor. 40

Figure 41: GC results for initial MDHA tests..... 41

Figure 42: Schematic of 125µm thick, ¼" OD palladium membrane. 42

Figure 43: Methane conversion over Mo/HZSM-5 catalyst (700°C, 3000 scc/g/hr) under different pressures with no Pd membrane..... 44

Figure 44: Products as a function of reaction pressure over Mo/HZSM-5 catalyst (700°C, 3000 scc/g/hr) with no Pd membrane. 44

Figure 45: Selectivity of aromatic products and methane conversion as a function of pressure over Mo/HZSM-5 catalyst (700°C, 3000 scc/g/hr) with no Pd membrane..... 45

Figure 46: Methane conversion over Zn/HZSM-5 catalyst (700°C, 3000 scc/g/hr) at different pressures with no Pd membrane..... 46

Figure 47: Selectivity of aromatic products and methane conversion as a function of pressure over Zn/HZSM-5 catalyst (700°C, 3000 scc/g/hr) with no Pd membrane..... 46

Figure 48: Products as a function of pressure over Zn/HZSM-5 catalyst (700°C, 3000 scc/g/hr) with no Pd membrane. 47

Figure 49: Methane conversion over 3wt%Zn/HZSM-5 catalyst (700°C, 3000 scc/g/hr) at different pressures with Pd tube membrane. 47

Figure 50: Products as a function of pressure and time over 3wt%Zn/HZSM-5 catalyst (700°C, 3000 scc/g/hr) with Pd tube membrane. 48

Figure 51: Performance of 4wt% Mo/HZSM-5 catalyst under methane DHA (700°C, 5 atm, 3000 scc/g/hr) with and without Pd membrane: (a) Methane conversion, (b) Benzene (BZ) selectivity. 49

Figure 52: Light hydrocarbon yields with 4wt% Mo/HZSM-5 under methane DHA (700°C, 5 atm, 3000 scc/g/hr) with and without Pd membrane: a) Ethane, b) Ethylene, c) Propylene. 50

Figure 53: Hydrogen production with 4wt% Mo/HZSM-5 under methane DHA (700°C, 5 atm, 3000 scc/g/hr) with and without Pd membrane. 51

Figure 54: Performance of 3wt% Zn/HZSM-5 catalyst under methane DHA (700°C, 5 atm, 3000 scc/g/hr) with and without Pd membrane: a) Methane conversion, b) Benzene (BZ) selectivity. 52

Figure 55: Light hydrocarbon yields with 3wt% Zn/HZSM-5 under methane DHA (700°C, 5 atm, 3000 scc/g/hr) with and without Pd membrane: a) Ethane, b) Ethylene, c) Propylene. 53

Figure 56: Benzene raw concentration (ppm) formed under different catalysts and temperatures during two reaction cycles. 54

Figure 57: DHAMR increment for a reactor with catalyst particles/retentate-side on the “shell” side with an example value of the low partial pressure of hydrogen on the permeate/tube side. 56

Figure 58: DHAMR increment for a reactor with catalyst particles/retentate on the “tube” side with an example value of the low partial pressure of hydrogen on the permeate side/shell. 57

Figure 59: Reactor model predictions for converstion and benzene production using a conventional reactor (no hydrogen removal by membrane). 58

Figure 60: Reactor model predictions for conversion and benzene production using significant hydrogen removal from reaction product suite using a 125 micron thick Pd membrane. 59

List of Tables

Table 1: Summary of Mo-Based Catalysts Synthesized and Tested for Methane Conversion..... 27

Table 2: Surface Properties of Mo-Based Catalysts 27

Table 3: Zn-Based Catalysts Studied for MDA Reaction..... 28

Table 4: Catalysts Evaluated in the FT Reactor and Experiment Conditions Used..... 31

Table 5: Summary of Methane Conversion Test Conditions..... 41

Table 6: Membrane Testing Results 43

Table 7: Conversions and Selectivities of 3wt% Zn/H-ZSM-5 at Different Pressures with Pd Tube Membrane 48

Acronyms, Abbreviations, and Symbols

Acronym	Descriptive Name
BTX	Benzene, Toluene, and Xylene
CBTL	Coal-Biomass to Liquids
CFD	Computational Fluid Dynamics
CMU	Carnegie Mellon University
C_6H_6	Benzene
DFT	Density Functional Theory
DHA	Dehydroaromatization
DHAMR	Dehydroaromatization Membrane Reactor
DOE	Department of Energy
EDS	Energy Dispersive X-Ray Spectrometer
EDX	Energy Dispersive X-Ray
fcc	Face Centered Cubic
FT	Fischer-Tropsch
GC	Gas Chromatograph
GHG	Greenhouse Gas
GHSV	Gas Hour Space Velocity
HPTR	High-Pressure Tubular Reactor
HRTEM	High-Resolution Transmission Electron Microscopy
HT	Hydrothermal Methods
IGCC	Integrated Gasification Combined Cycle
IWI	Incipient Wetness Impregnation
MDA	Methane Dearomatization
MDHA	Methane Dehydroaromatization
MTG	Methanol to Gasoline
MWAHT	Microwave-Assisted Hydrothermal Method
NCCC	National Carbon Capture Center
NETL	National Energy Technology Laboratory
ORD	Office of Research and Development
Penn State	The Pennsylvania State University
Pitt	University of Pittsburgh
R&D	Research and Development
RES	Research and Engineering Services
SAR	Silica to Alumina Ratio
SCC	Strategic Center for Coal

Acronym	Descriptive Name
SEM	Scanning Electron Microscopy
TEM	Transmission Electron Microscopy
TPD	Temperature Programmed Desorption
WHSV	Weight Hourly Space Velocity
WVU	West Virginia University
XRD	X-ray Diffraction
ZSM-5	Zeolite Socony Mobil–5

1.0 Executive Summary

Increasing global population and quality of life demands will continue to drive the necessity for abundant and affordable potable water, clean energy, and food supplies into the future. The thermochemical conversion of carbon-based feedstocks is a promising route for the production of affordable and clean energy commodities (heat, power, transportation fuels, chemicals, plastics, etc.) due to its flexibility to accommodate a variety of feeds, as well as the inherent nature of the process to facilitate near zero greenhouse gas (GHG) emissions when coupled with carbon capture and storage. Leveraging large domestic fossil energy resources (i.e., coal) with other opportunistic energy sources (i.e., biomass) in co-feed configurations has the potential to produce nationally derived, abundant, and affordable energy commodities, including transportation fuels through coal-biomass to liquids (CBTL) routes.

In an effort to facilitate the advancement of clean, affordable, and abundant domestic fuel technologies, this research will focus on the development of processes aimed at producing CBTL-based transportation fuels with lower cost and lower GHG footprint as compared to conventional petroleum-derived fuels. Specifically, the current National Energy Technology Laboratory Office of Research and Development (NETL-ORD) effort will be limited to exploring and developing "post-syngas production" strategies focused predominantly on the management of CBTL-based Fischer-Tropsch (FT) tail gas options including the optimization of recycle, power generation, and energy commodity production.

Several research thrusts are critical for advancing the use of coal and biomass feeds for the production of clean and affordable synthetic, drop-in transportation fuels, including:

- Development and assessment of novel process-level approaches to provide economical and clean CB-derived fuels, including novel management schemes for CBTL-based FT off-gases and integration of carbon management strategies.
- Assessment and optimization of integrated reactors systems, including thermocatalytic membrane reactors tailored for overcoming equilibrium limitations associated with CBTL.
- Development of stable, durable, and highly active thermocatalytic materials and pathways for the selective production of affordable, clean energy commodities.
- Development of stable, highly permeable, and selective separation techniques facilitating integration in CBTL pathways.
- Providing insight to the fundamental phenomena leading to the development of transformational materials, systems, and processes for CBTL technologies.

From a CBTL perspective, the hypothesis is that rather than utilizing the FT tail gases as a simple mixture from which H_2 is separated for electricity production, utilizing the gases as a feedstock for chemical production would produce a more valuable commodity (aromatics). These commodities could then be sold at a premium price, making the process economics more favorable while reducing economic risks for synthetic fuel sales.

This project will use an "Integrated Technology Development" approach; to leverage top-down computational and experimental approaches focused on providing relevant techno-economic solutions facilitating CBTL deployment. Targets of this research include:

Membrane-Based Separations

One key element behind the separations effort is to focus on more rugged separations materials that can withstand and function in "real" conditions, which may be an important paradigm shift away from focusing on a flux goal. While the material must still have desirable flux properties, thicker, more resistant materials that are more stable at higher temperatures may be of greater importance to modules

relative to the overall cost of energy delivered. The primary framework focuses on the effect of exposure to constituents and contaminants inherent to the process environment, and how that chemistry may affect the efficiency of separation and performance (i.e., flux, selectivity, stability, and lifetime).

Thermocatalytic Pathways

Another focus of the Fuels research team is to explore materials and methods for improving the conversion process for gaseous components of fossil sources, most notably methane but possibly including other light species (C2-C5) as well. The conversion of these materials into valuable chemical products and fuels would bolster the role that gas can play in the commodities and transportation sectors. Combinations of catalyst design and testing, reaction mechanism identification, as well as separation materials and modules, will be used in pursuit of this goal. Currently, reactions of methane to benzene, for example, are thermodynamically limited to roughly 12% conversion at 700 °C. Combining catalysts and separations to optimize the conversion of methane to benzene with removal of the hydrogen "by-product" produced would offer a sophisticated means of driving the reaction toward more benzene production. This, in turn, would offer a means whereby FT off-gas could be used as a feedstock for production of aromatics such as benzene.

One critical element within this work is to develop catalytic materials that enhance the conversion of relevant gas-stream components into useful products. Some pathways include syngas conversion, as well as the conversion of coal-gas components. One of the primary drivers is the limited efficiencies and selectivities of current conversion systems. The desired end-products of these conversions may include aromatics, olefins, hydrogen, or liquid fuels. Fruitful pathways for research include the improvement of existing catalyst formulations in terms of selectivity, conversion efficiency, and the development on catalysts using novel materials and design approaches. These novel designs may circumvent the primary issues that plague conventional conversion catalysts, namely shortened lifetimes due to coking and harsh regeneration procedures. Furthermore, the incorporation of catalysts and separations into reactor modules that can then be applied for process intensification opportunities for larger scale conversions will be explored.

Process and Systems Level Assessments

This effort will leverage a top-down approach in an effort to ensure that this work results in relevant solutions providing technology options facilitating the production of low GHG footprint, low cost synthetic fuels. In collaboration with NETL Program and Program Performance and Benefits (OPPB), process-level modeling and novel optimization algorithms, as well as detailed system level Computational Fluid Dynamics (CFD) modeling will be used to assess techno-economics of current technologies. This multi-scale framework, which will leverage tailored experimental data generated within the effort, will also be used to facilitate the direction of future technology options.

Major Accomplishments and Key Findings

Membrane-Based Separations

Previous results of alloy exposure tests have demonstrated that minor gas stream impurities such as As and Se are much more important than previously thought, as both of these elements were seen to play an important role in the corrosion process of Cu-Pd alloys. In order to better quantify the role played by As and Se in corrosion, an in-house apparatus was fabricated during FY13 with the ability to expose multiple alloy coupons to a variety of gas compositions containing As and Se, in addition to traditional syngas components, at temperatures up to 1000 °C. Once the rig had undergone shakedown experiments, a series of membrane alloy coupons were exposed to syngas containing contaminants using a gas composition (in mol %) of 47 H_2, 20 CO_2, 32 H_2O, 1 CO, 35 ppmv H_2S. In addition, 1 and 5 ppm of both AsH_3 or H_2Se, as single contaminant components, were introduced in the gas stream. The tests were carried out at both

350 and 500°C. Preliminary results indicated that ternary alloys (CuPdMg and CuPdAl) experienced the least amount of contaminant uptake, followed by CuPd binaries with proportions in the 50-50 range. The pure metals (Pd and Cu) experienced the most significant increases in mass change when exposed to test contaminants. These results could aid in the down-selection of materials that could be candidates for separations in syngas environments containing As and/or Se.

During FY13, a novel approach for protecting vulnerable separation materials was conceived. The approach is based on the use of thin coatings that could be functionalized to repel gas phase contaminants (such as H_2S) while allowing hydrogen transfer. Testing of this concept using a thin coating on pure palladium substrate was performed. Testing of several prototype materials in both pure H_2 and H_2 containing 1000 ppm H_2S was conducted in this quarter. A wide range of flux values were observed in pure H_2 after steady state was reached, which suggested that the coatings varied significantly in their degree of surface coverage and/or flaws. However, improvements in performance at blocking the H_2 flux were observed for samples that were subjected to a pre-exposure annealing step, suggesting that the coating could function as expected if its quality was improved. Exposure to 1000 ppm H_2S in H_2 resulted in a steadily dropping flux, as a Pd_4S surface corrosion layer was observed. However, scanning electron microscopy (SEM) identified several regions of the coated membrane surface that were free of any sign of bulk corrosion buildup, suggesting that in this region the coating demonstrated the ability to prevent H_2S from attacking the Pd surface. While it is not yet known specifically why this area was protected, possibilities include that this was an area where the monolayer coating was of high perfection or perhaps an area where there was a multilayer coating.

Thermocatalytic Pathways

The targeted reaction for Fuels research is the thermocatalytic conversion of methane to aromatics via the dehydroaromatization (DHA) reaction. This reaction is a direct conversion, yielding aromatics and hydrogen as products, and is thermodynamically limited to about 12% conversion at 700 °C. A detailed literature survey on the methane DHA reaction was completed. Manuscripts and results were summarized according to the type of catalyst and promoter type used, reaction conditions used, and catalyst synthesis methods. An EndNote-based literature database was compiled, and this database was made available for other researchers on the team. The goal of the catalyst development work is to use conventional gas conversion catalyst systems as a baseline for conversion efficiency, as well as confirm where traditional catalysts fall short in terms of lifetime, conversion efficiency, and regeneration. Then, once these areas are established, the goal is to synthesize new catalysts that may address the shortcomings and advance the conversion process toward increased formation of aromatic products. Coincident with catalyst development efforts is the application of a hydrogen membrane reactor system to the DHA reaction. Because hydrogen is produced as a co-product with the target aromatic species, the equilibrium reaction can be shifted toward formation of more products if the hydrogen can be removed. A caveat to this strategy is that forcing the reaction toward more products will place additional constraints on the catalyst in terms of coke resistance, lifetime, and regenerability.

To generate baseline data on conversion of methane to benzene using DHA, a series of Molybdenum-zeolite catalysts, which have been studied for decades, were synthesized and evaluated. The catalysts contained 6% (wt) Mo on various Zeolite Socony Mobil–5 (ZSM-5) catalysts with different silica to alumina (Si-to-Al) ratios (SARs) in order to study the effect of acid sites as well as space velocity. It was determined that a Mo/ZSM-5 catalyst with SAR of 50 was the most active in the experiments, and was most selective toward benzene formation. The optimum space velocity was 3000 cc/g/h for the SAR 50 catalyst.

Using these baseline conditions, a series of molybdenum-based catalysts with various metal promoters (MoZnM/ZSM-5 or MoM/ZSM-5, where M = Fe, Ru, or Os) were studied for the methane DHA reaction. The goal was to minimize coke formation and hence increase catalyst life time while maintaining the

catalyst activity and selectivity, and literature has shown that transition metal promoters can provide hydrogenation sites to the coke. Also, because the transition metals will be anchored on the surface Bronsted acidic sites, which are not useful for the desired reaction, it could eliminate these surface Bronsted acidic sites from participating in coke formation reactions. Over six hours of testing, there was no significant difference found in the activity for any of the catalysts, with methane conversion leveling at around 6%. The benzene selectivity from the doped Mo-catalysts was lower than the Mo only catalyst, except for the MoZnFe catalyst.

A series of more traditional Zn-based catalysts (Zn/ZSM-5 catalyst prepared by incipient wetness) were synthesized and tested for the methane DHA reaction. Catalysts with ZnO as the active phase are thought to be promising because while they react more slowly, they also deactivate more slowly and hence could be advantageous for coke resistance. Also, because the active phase is thought to be the oxide itself and not a carbide or oxy-carbide that must be re-formed after each regeneration step, the ZnO catalysts should be easier to regenerate than the corresponding Mo catalysts. One caution is that Zn may be volatilized from the catalyst at the high temperatures used for DHA reactions unless it is maintained in the oxide form.

A series of tests were conducted in a non-membrane reactor system to compare the conventional Mo catalysts to the conventional ZnO catalysts. In the non-membrane system, operating at higher pressure will increase the residence time. For the Mo catalysts, this increased residence time initially benefitted the formation of benzene. However; further increases in residence time led to formation of lesser amounts of benzene, as it appears that the reaction product had less chance of diffusing out of the pores and was susceptible to further polymerization, chain growth, and coking. The ZnO catalyst exhibited slightly lower conversion and slightly lower selectivity, but was much less affected by increases in pressure.

The regeneration performance of ZnO catalysts for multiple reaction cycles was also investigated. It was found that a potentially significant loss of the metal may be occurring due to reduction of the metal followed by vaporization of metallic species. In light of this finding, the effect of different promoters to stabilize Zn catalysts under different reaction temperatures using simulated natural gas was investigated. It was found that Ce- and Y-promoted Zn catalysts retained functionality significantly better than unpromoted Zn catalysts did, at least for two cycles of reaction-deactivation.

In addition to synthesis and testing of conventional ZnO/ZSM-5 catalysts, a novel catalyst was developed that incorporates nanoparticulate ZnO as the active site for methane activation embedded into the pores of the zeolitic framework of ZSM-5. The goal is to minimize coking by nanostructuring the catalyst to allow the aromatization products to escape from the catalyst pore network before they undergo the secondary, coke-forming reactions that are blamed for ending catalyst activity. Initial efforts on the synthesis of nanostructured metal-zeolite catalysts were able to successfully establish a good degree of synthetic control over the zeolite structure, and identified the impact of temperature and pH as key synthetic parameters. In addition, the synthesis time was shortened by about half, from 5 days down to ~2-3 days. ZnO (nanoparticles) with monodispersity in the size range targeted for the DHA catalyst were successfully obtained. These ZnO nanoparticles were successfully encapsulated in silica ($ZnO@SiO_2$), and then the silica was finally converted to zeolite, yielding the world's first ZnO@ZSM-5 structure for use in DHA reaction tests to evaluate conversion, coke resistance, and regenerability.

Additional studies of the synthesis procedure confirmed the key role of embedded ZnO nanoparticles for the emergence of mesoporosity in these zeolite materials. Both weight loading and size of nanoparticles are clearly correlated with the formation of mesopores and the resulting mesopore volume. These results point out the possibilities of structuring catalysts by being able to induce and control porosity of the materials. However, it is likely that the reactivity of the materials can be expected to constrain the range of acceptable weight loadings and NP sizes.

Testing of a baseline Pd membrane for use in a methane to benzene conversion scheme was initiated. The theory is that removal of the hydrogen produced by the reaction would drive the reaction toward the formation of products, thus circumventing the thermodynamic limitation of the reaction. The feasibility of removal of one of the products to increase the conversion was examined using a conventional Mo catalyst. The results indicated that higher hydrocarbons were formed, but a significant amount of carbon was also formed. The primary limitation of catalysts and systems used for this conversion reaction is coke formation.

In order to compare results for this same catalyst system with no membrane, a test plan was developed to match the conditions used for non-membrane testing (such as gas hour space velocity [GHSV], temperatures, pressures) to isolate the direct effect of the membrane system. It was confirmed that increased hydrogen was observed in the membrane sweep stream at higher pressures, indicating that the membrane was functioning in the presence of methane and was successfully removing the hydrogen reaction product. Testing of various catalysts in a membrane system compared to non-membrane systems showed that only a slight increase (1-2%) was observed using a membrane system, but the system had a significant effect on the product distribution. The small change in conversion was attributed to a relatively insignificant amount of hydrogen being removed compared to what would be required to observe a larger increase in conversion. The significant increase in light hydrocarbon production (ethane, ethylene, propylene) suggests that the ring formation step of the aromatization mechanism is slower than methane coupling reactions.

Process and Systems Level Assessments

The development of a simplified model for a methane DHA membrane reactor was completed. Initial efforts were to define the desirable capabilities of the simplified reactor model. The focus was on modeling of a membrane reactor unit containing a fixed bed of catalyst particles retained within hydrogen-permeable walls of the reactor. The model design incorporates a material balance, a simplified version of reaction kinetics for the selected catalyst, and hydrogen permeance as a function of palladium alloy composition and operating conditions. Following an extensive literature review, the governing equations for a simple model of a DHA reactor were derived. The configuration of the base reactor system was established. The model will aid in predicting the conversion of methane to benzene, the retentate-side concentrations of methane, hydrogen, and benzene as a function of length from the inlet and the flux of hydrogen through the membrane wall into the permeate side at constant pressure. While the simple model is not designed to compete with or replace an extensive CFD model of the reactor system, it will allow users to quickly evaluate the effect of major design parameters of the reactor on reactor performance.

After establishing the configuration of the base reactor system, several iterations of the model outputs were obtained using various input parameters. For example, the model was run using “poor hydrogen removal” conditions, where the H_2 flux was set to 0. In this configuration, the concentration of hydrogen in the reactor would expect to increase with little or no increase in benzene production. In this case, the predicted conversion of 10.5% approaches the thermodynamic limit of 11.7%, hence agreeing with thermodynamic calculations. A second iteration of the model, where significant hydrogen removal by a Pd membrane is input into the parameters, predicts a significant increase in both methane conversion (53.2%) and benzene production over equilibrium limits.

2.0 Technology Highlights and Key Results

Membrane-Based Separations

Materials development efforts focused on identifying metal alloys that are likely to withstand the severe environment associated with syngas separations. Calculations of the material's propensity for sulfidation and/or oxidation were used to determine the likelihood of corrosion, using either existing thermodynamic data or ab initio methods. When these were not feasible, exposure testing to simulated syngas at elevated temperatures was carried out. The experimental methods for identifying promising alloys were expanded to include other syngas contaminants such as As and Se.

Efforts also focused on the evaluation of a novel approach for protecting vulnerable separation materials. The approach is based on the use of thin coatings that could be functionalized to repel gas phase contaminants (such as H_2S) while allowing hydrogen transfer. Testing of this concept using a thin coating on pure palladium substrate was performed.

Elevated-Temperature Corrosion of High-Entropy Alloys in Simulated Syngas Containing H_2S

The desire to utilize hydrogen separation membranes in aggressive environments is the driving force behind the search for the alternative materials for this application. Environments such as coal-derived syngas laden with contaminants are forcing us to increasingly look at the stability of materials in these environments rather than focusing solely on the hydrogen transport properties of the membrane materials. U.S. Department of Energy's (DOE) 2015 target for durability of the membranes in syngas is 5 years. Most known metallic materials with high hydrogen permeability are far from meeting this target primarily due to the corrosive effects of impurities in syngas. As a result, metallic materials with acceptable hydrogen permeability (not necessarily high permeability) but high environmental stability can be a good candidate for membranes to separate hydrogen from syngas. The environmental stability of the new high entropy alloys in a syngas environment is investigated with this understanding.

Recently, a new alloying concept for preparing novel structural and functional alloys has been proposed. Alloys synthesized using the new strategy are termed "high-entropy alloys." High-entropy alloys are formed by synthesizing multiple principle elements in equimolar or near equimolar concentrations. The complexity of chemistry causes high mixing entropy for the alloy leading to stability of simple crystal structures of solid solution phases. $CoCrCuFeNiAl_{0.5}B_x$ (x=0, 0.2, 0.6, 1) high-entropy alloys investigated in this work contain six principal elements plus boron added at varying proportions. Microstructure of these alloys is composed of a mixture of disordered bcc and face centered cubic (fcc) phases. Because of the simplicity of their crystal structure, they may yield sufficiently high hydrogen flux should they be employed as membrane materials.

In order to determine their stability in a post water-gas shift reactor environment, coupon corrosion tests were performed in a severe environment exposure laboratory which contains tube furnaces, gas mixing facility, gas thermal oxidizer, water pumps, and automated control and safety shut-off systems. A simulated syngas mixture (representative of a composition downstream from water-gas shift reactors) containing (in vol%) 50% H_2, 30% CO_2, 1% CO, 19% H_2O, and varying amounts of H_2S was prepared using mass flow controllers. As an H_2S source, a premixed CO_2 and H_2S gas containing 1% H_2S was used in order to attain low levels of H_2S in the final mixture. The H_2S levels used in this series of experiments were 0%, 0.01%, 0.1% and 1% by volume (which resulted in sulfur partial pressure of 0, $3.6\text{x}10^{-15}$, $3.6\text{x}10^{-13}$, and $3.6\text{x}10^{-11}$ atm, respectively, at 500°C). A predetermined amount of distilled water was introduced directly into the hot zone of the furnace at a constant rate using a syringe pump. Oxygen partial pressure was calculated to be about 10^{-28} atm in all tests.

Test coupons cut from the above mentioned alloy pieces with approximate dimensions of 20 mm x 10 mm x 1 mm were surface ground by hand with 600 grit sandpaper, cleaned, and weighed on a

microbalance accurate to 10 µg. In addition to the high-entropy alloys, two reference coupons were also included in the tests. They were a pure Cu coupon and a commercially available MA956 alloy coupon. The samples were placed individually in high-density alumina crucibles on their edges in a way that more than 95% of the surface area was exposed to the gas mixture. The crucibles were situated in the hot zone of the tube furnace with the help of an alumina tray. After the ends of the tube were sealed, helium flowed through the tube for two hours to flush air out at room temperature. At this point the furnace was turned on and heated at a rate of 200°C per hour until 500°C was reached. During heating, helium flow was maintained. Once the furnace reached 500°C, the flow of helium was terminated. The simulated syngas mixture was then introduced into the system with H_2O injected using a water pump. The gas flow rate at 500°C was 500 ml/min. Calculations based on estimates for residence time distribution in a tubular reactor (7.6 cm diameter and 91.4 cm long) featuring laminar flow showed that 99.5% of the gas in the tube is exchanged in one hour. The samples were exposed to these conditions for 24 h before the gas mixture and water flow were stopped and the helium flow was restarted. After one hour in flowing helium, the furnace was allowed to cool to room temperature. The samples were then removed from the furnace and weighed to assess mass gain or loss.

After the 120 hour exposure was complete, X-ray diffraction (XRD) analysis was performed to determine the phases present on the surface of the exposed samples. An X-ray diffractometer (Rigaku Ultima III) was used to collect the XRD spectra from the exposed surfaces between 20 and 90 degrees of 2θ. The XRD data was analyzed using ICDD DDView+ software and PDF-4+ database. The surface and the cross-sections of the samples were also analyzed using SEM. A FEI Inspect F SEM with a field emission gun equipped with energy dispersive X-ray spectrometer (EDS) with Oxford INCA analysis software was utilized. For the cross-section samples, the coupons were sectioned, mounted, and polished, with the final polishing step using a 0.06 µm colloidal silica suspension with 1-2% NaOH solution for 8-16 h.

The mass change as a function of exposure time and H_2S content of the simulated syngas was plotted in Figure 1. Mass of the test coupons did not change significantly with time when the gas contained 0% or 0.01% H_2S (Figure 1[a] and ([b]). However, when the H_2S level in the syngas was raised to 0.1%, each high-entropy alloy coupon exhibited mass gain as plotted in Figure 1(c). In general, mass gain for the HEA exposure coupons was about five times less than that of the Cu coupon after 120 hours of syngas exposure at 500°C. Under these conditions, similar mass gains were recorded for the HEA-0B, HEA-0.2B, and HEA-1B coupons whereas the HEA-0.6B coupon gained mass at a slightly higher rate. The other reference material, MA956, did not gain any significant mass under these conditions. HEA-0B was the only high entropy alloy tested in syngas containing 1% H_2S (Figure 2). It gained about 20 times less mass than the Cu sample. Again, the other reference material MA956 did not show any significant mass gain at 1% H_2S.

A mixture of sulfides and oxides formed the external corrosion scale in all four high-entropy alloys exposed to syngas containing 0.1 and 1% H_2S (Figure 3). $Cu_{1.96}S$ was the primary sulfide for $CoCrCuFeNiAl_{0.5}$ and $CoCrCuFeNiAl_{0.5}B_{0.2}$, whereas $FeCo_4Ni_4S_8$ was the primary sulfide for $CoCrCuFeNiAl_{0.5}B_{0.6}$ and $CoCrCuFeNiAl_{0.5}B$ (Figure 3).

No oxides were observed on the high-entropy alloy samples exposed to syngas containing 0 and 0.01% H_2S. Sulfide formation on the surface of these alloys was a prerequisite for the formation of oxides. Fe_3O_4 formed in the external scale of the high-entropy alloys in syngas containing 0.1 and 1% H_2S. Formation of sulfides containing no or little Fe caused Fe enrichment on the surface resulting in high enough Fe activity to form Fe_3O_4 in low oxygen partial pressures.

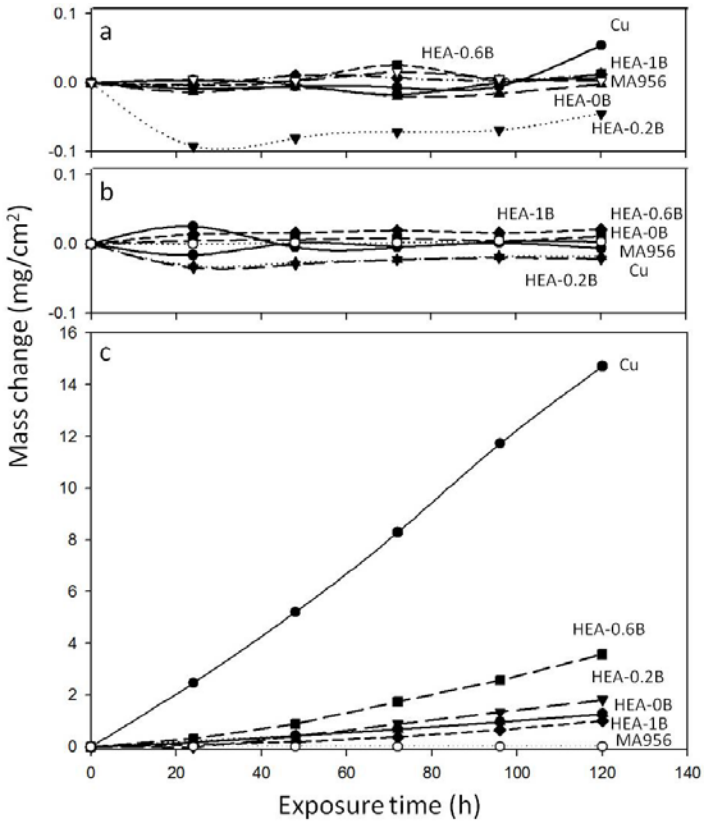

Figure 1: Mass change of the high entropy alloys and reference materials during the exposure to syngas containing various amounts of H_2S at 500°C; (a) 0% H_2S, (b) 0.01% H_2S, and (c) 0.1% H_2S.

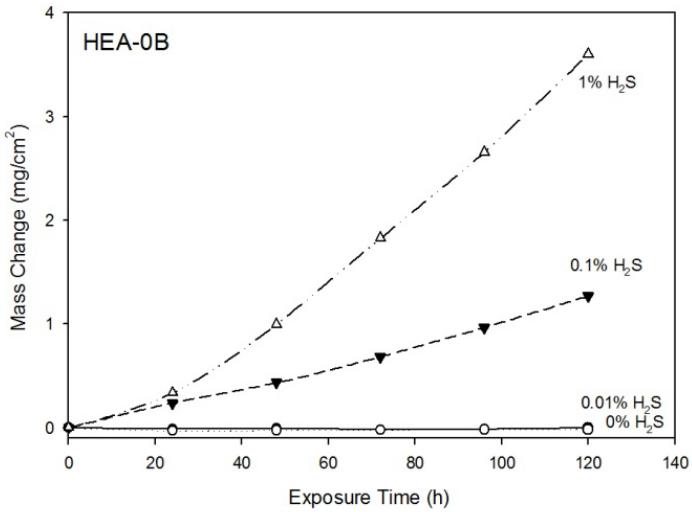

Figure 2: Mass gain due to oxidation and sulfidation of $CoCrCuFeNiAl_{0.5}$ in simulated syngas containing several different levels of H_2S. The tests were conducted at 500°C for 120 hours.

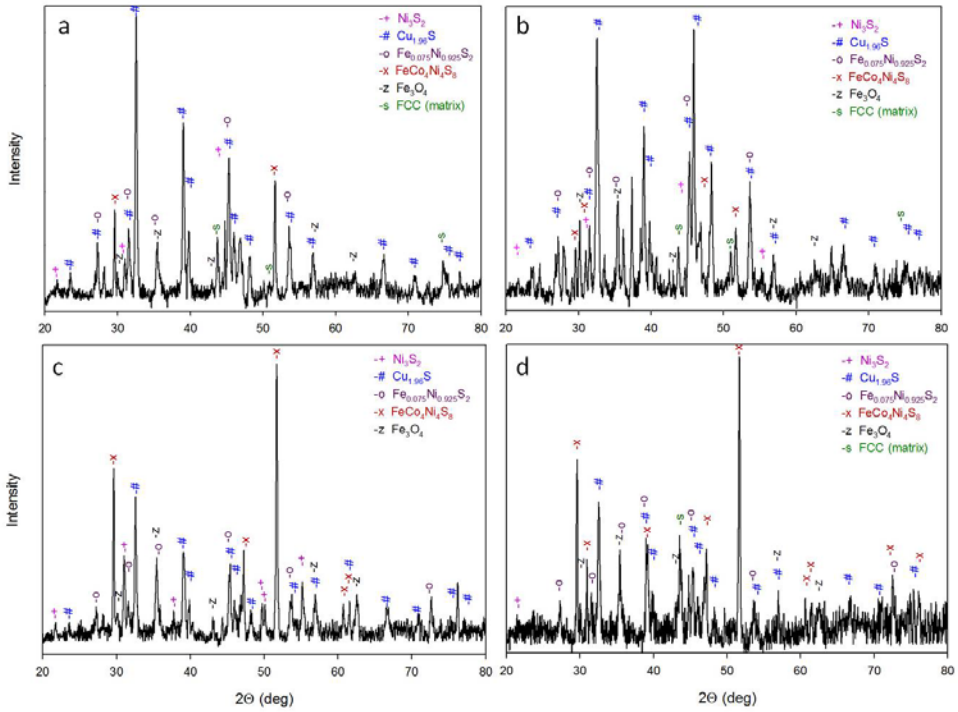

Figure 3: XRD spectra acquired on the surface of the high entropy alloys exposed to syngas containing 0.1% H_2S at 500°C for 120 h; (a) $CoCrCuFeNiAl_{0.5}$, (b) $CoCrCuFeNiAl_{0.5}B_{0.2}$, (c) $CoCrCuFeNiAl_{0.5}B_{0.6}$, and (d) $CoCrCuFeNiAl_{0.5}B$.

Multi-phase Cu-rich regions in the low B high-entropy alloys were vulnerable to corrosive attack as shown in Figure 4(a). Sulfur and oxygen diffusion via grain boundaries to these regions resulted in formation of oxides and sulfides. The main matrix phase (fcc) remained resistant to corrosion in these alloys.

Increasing B concentration in the high-entropy alloys caused an increase in volume fraction of iron-chromium borides and a decrease in volume fraction of Cu-rich regions. While the diminishing Cu-rich regions improved the corrosion resistance of $CoCrCuFeNiAl_{0.5}B_{0.6}$ and $CoCrCuFeNiAl_{0.5}B$, reduced Cr concentration of the fcc matrix due to formation of borides lowered the corrosion resistance of these alloys (Figure 4b).

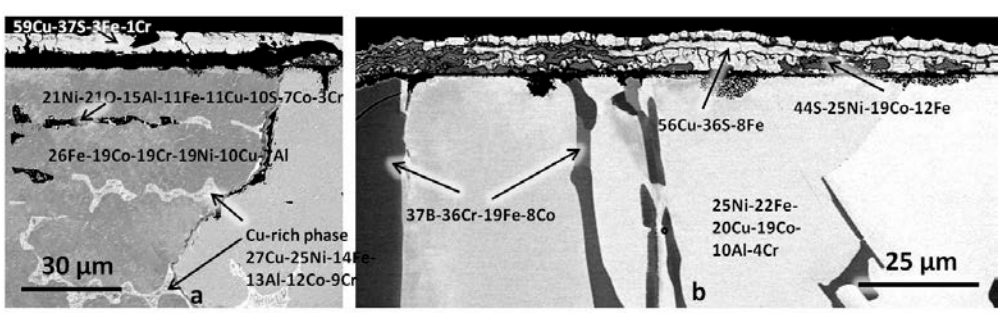

Figure 4: SEM images of the cross sections of the $CoCrCuFeNiAl_{0.5}$ (a) and $CoCrCuFeNiAl_{0.5}B$ (b) coupons exposed to syngas containing 0.1%H_2S at 500°C for 120h. The compositions are in atomic percent.

Major Accomplishments and Key Findings

- No significant corrosion of high-entropy alloys was detected at 500°C in syngas containing 0 and 0.01% H_2S whereas significant corrosion of these alloys was observed in syngas containing 0.1 and 1% H_2S.
- A mixture of sulfides and oxides formed the external corrosion scale in all four high-entropy alloys exposed to syngas containing 0.1 and 1% H_2S. $Cu_{1.96}S$ was the primary sulfide for HEA-0B and HEA-0.2B, whereas $FeCo_4Ni_4S_8$ was the primary sulfide for HEA-0.6B and HEA-1B.
- No oxides were observed on the high-entropy alloy samples exposed to syngas containing 0 and 0.01% H_2S. Sulfide formation on the surface of these alloys was a prerequisite for the formation of oxides. Fe_3O_4 formed in the external scale of the high-entropy alloys in syngas containing 0.1 and 1% H_2S. Formation of sulfides containing no or little Fe caused Fe enrichment on the surface resulting in high enough Fe activity to form Fe_3O_4 in low oxygen partial pressures.
- Multi-phase Cu-rich regions in the low B high-entropy alloys were vulnerable to corrosive attack. Sulfur and oxygen diffusion via grain boundaries to these regions resulted in formation of oxides and sulfides. The main matrix phase (fcc) remained resistant to corrosion in these alloys.
- Increasing B concentration in the high-entropy alloys caused an increase in volume fraction of iron-chromium borides and a decrease in volume fraction of Cu-rich regions. While the diminishing Cu-rich regions improved the corrosion resistance of HEA-0.6B and HEA-1B, reduced Cr concentration of the fcc matrix due to formation of borides lowered the corrosion resistance of these alloys.
- The high-entropy alloys may be stable at higher H_2S levels if their composition is modified by lowering or eliminating Cu.

Stability of CuPd Membranes in Syngas at 500, 650 and 800°C

Sulfidation and/or oxidation propensity of an alloy can be calculated and compared to the sulfur and/or oxygen partial pressure versus temperature plot at a given process point in an integrated gasification combined cycle (IGCC) system. Figure 5 shows an example of such a plot. The dark gray lines in this figure indicate the sulfur partial pressure as a function of temperature for four H_2S concentrations in syngas containing 50% H_2. The color lines indicate the critical sulfur partial pressure required to form a sulfide of a metal as a function of temperature. If the critical sulfur partial pressure required for forming a sulfide (a color line) lies above the sulfur partial pressure line (one of the gray lines) of the environment, then the metal or alloy is predicted to be stable in that environment and will not form sulfides. The plot in Figure 5, for example, demonstrates that the $Cu_{47}Pd_{53}$ alloy is stable above 700°C in syngas containing 1% H_2S. Below 700°C, the alloy forms Pd_4S on the surface.

Previous results at NETL demonstrated that 60Pd-40Cu and 53Pd-47Cu alloys resisted sulfidation at 635°C in He containing 0.1% H_2S even though they were sulfidized at 350 and 450°C. These results are in agreement with the thermodynamic predictions presented above. In Q3, a series of experiments was conducted to further demonstrate that at higher temperatures, CuPd membranes are more resistant to sulfidation in H_2S containing syngas. These tests will provide the data for utilizing the CuPd membranes more effectively in syngas streams.

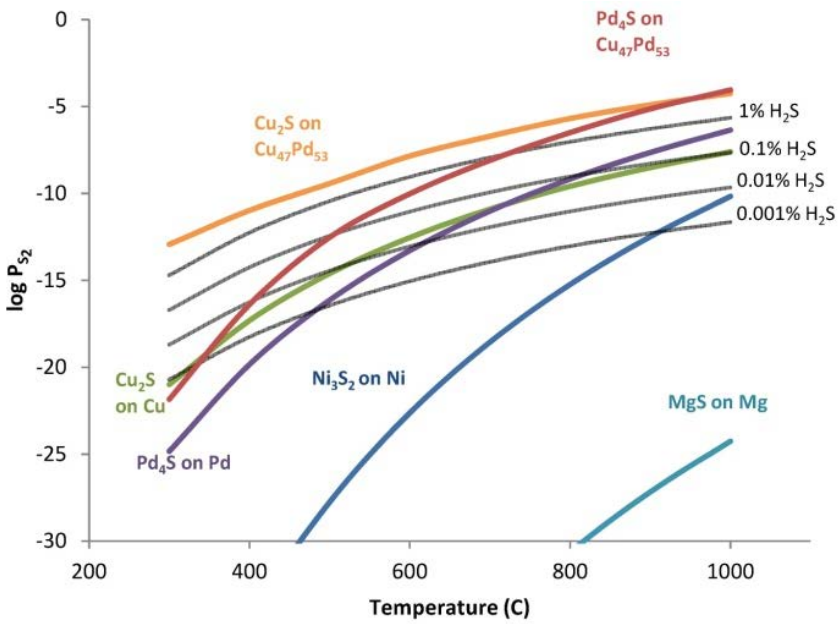

Figure 5: Stability of sulfides on various metallic materials as a function of sulfur partial pressure and temperature.

Coupon corrosion tests were performed in the severe environment exposure laboratory as described above in Section A. The coupons were exposed to the simulated syngas containing 1000 ppm H_2S at 500°C, 650°C, and 800°C.

Analysis of data in Figure 6 shows mass change of the coupons as a function of exposure temperature. In general, as the temperature increased, the mass gain of the coupons increased. The mass change of the Cu-Pd binary alloys was different at different temperatures. At 500°C, the Cu-70Pd coupon gained the most weight and the low Pd alloys (Cu-40Pd and Cu-34Pd) did not gain any mass. On the other hand, the low Pd alloys gained the most mass and the Cu-70Pd gained the least mass at 800°C. At the intermediate temperature of 650°C, none of the binary alloys changed mass significantly. Further analysis (XRD and EDS) is being carried out to better understand this behavior.

While the ternary alloys (Cu-Pd-Mg and Cu-Pd-Al) did not gain significant mass at 500°C, they did gain considerable mass at 650°C and certainly at 800°C. The SEM micrographs in Figure 7 and Figure 8 agree with this result. SEM micrographs (Figure 7) of cross-sections of CuPdMg membrane coupons exposed to the same syngas at three different temperatures show the extent of corrosion zone and the formation of MgS at 500°C and MgO at 650 and 800°C. SEM micrographs (Figure 8) of cross-sections of CuPdAl membrane coupons exposed to the same syngas show no significant corrosion at 500°C. Oxygen diffusion through the interdendritic regions results in oxidation of Al, first on the surface of dendrites at 650°C, then throughout the dendrites at 800°C.

While the Cu-50Pd membrane alloy is resistant to corrosion at 500°C as shown in the cross-section SEM image in Figure 9, it begins to form subsurface compounds at 650°C. Volume fraction of the subsurface compounds increases at 800°C. These compounds have not been identified yet due to their dissolution during sample preparation.

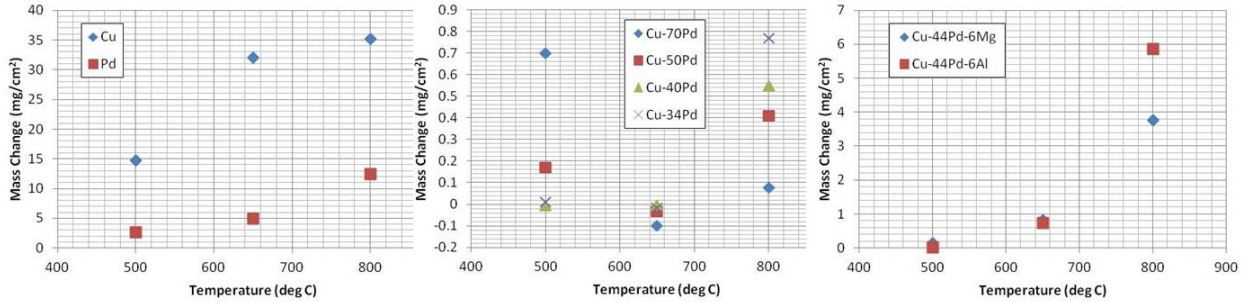

Figure 6: Mass change of the membrane alloy coupons after 120 hour exposure to simulated syngas containing 1000 ppm H_2S at 500, 650, and 800°C.

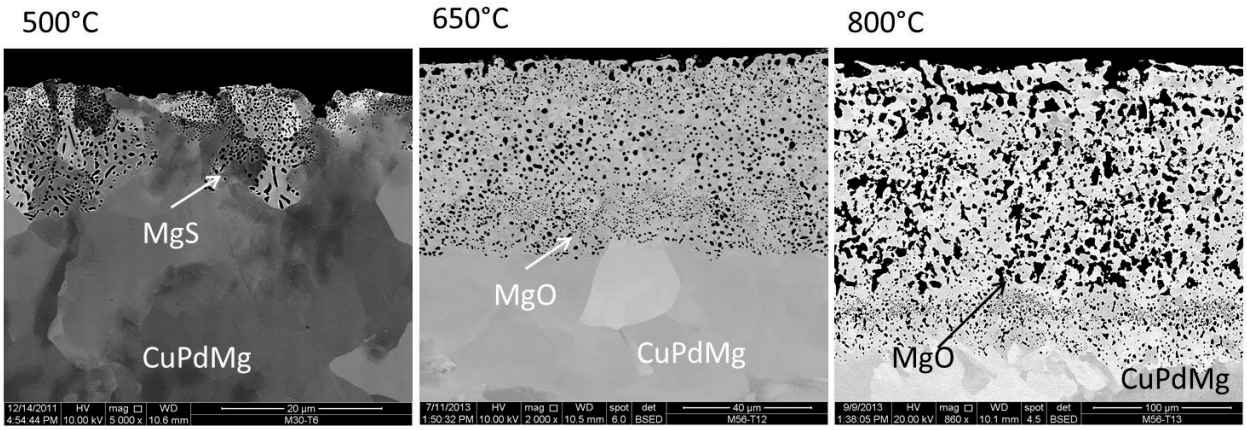

Figure 7: SEM micrographs of cross-sections of CuPdMg membrane coupons exposed to the same syngas at three different temperatures. Note the extent of corrosion zone and the formation of MgS at 500°C and MgO at 650 and 800°C.

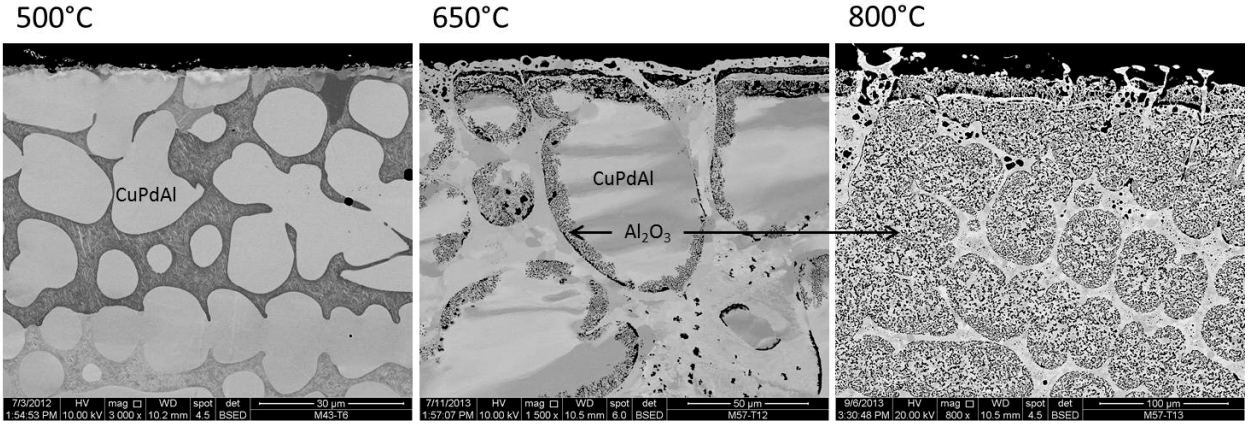

Figure 8: SEM micrographs of cross-sections of CuPdAl membrane coupons exposed to the same syngas at three different temperatures. No significant corrosion takes place at 500°C. Oxygen diffusion through the interdendritic regions results in oxidation of Al, first on the surface of dendrites at 650°C, then throughout the dendrites at 800°C.

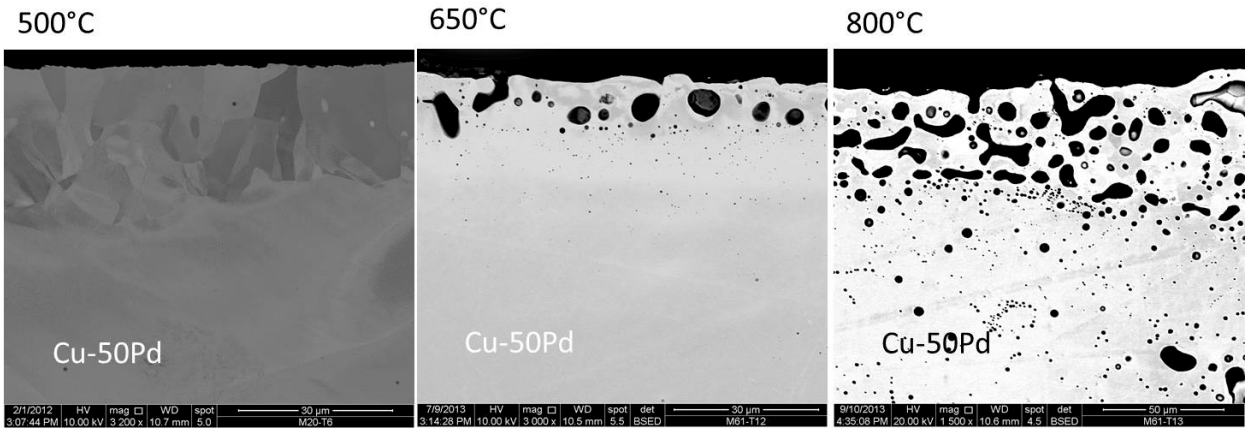

Figure 9: Surface effects on the Cu-50Pd membrane alloy exposed to simulated syngas at 500°C, 650°C, and 800°C for 120 hours.

In general, the primary corrosion reactions on the membrane alloys are sulfidation in syngas containing 1000 ppm H_2S at 500°C, whereas the oxidation reactions are more prevalent at higher temperatures in the same syngas. Analysis of the data is continuing and will be reported in the next quarter.

Exposure of Membrane Alloys to Syngas Containing As and Se

Real syngas exposures of the NETL membrane materials have been done at the National Carbon Capture Center (NCCC) in Wilsonville, Alabama, over the last several years. Palladium binary and ternary alloys for hydrogen separation membrane applications were exposed to an actual gasifier syngas effluent stream in the air-blown transport gasifier at the NCCC. The coupons were exposed to unshifted syngas containing about 250 ppm H_2S for approximately 1000 hours at about 400°C. One of the significant results of this investigation demonstrated that minor gas stream impurities such as As and Se are much more important than previously thought. Both of these elements play an important role in the corrosion process of the Cu-Pd alloys.

To aid in determining the role played by As and Se in corrosion of Cu-Pd alloys, a test apparatus (Figure 10) that had been designed and installed during first two quarters, was completed in Q3 and has undergone one shakedown run to confirm its set-up and operation. The tests started in Q3 and completed in Q4.

In these tests, a series of membrane alloy coupons were exposed to syngas containing contaminants. The gas composition (in mol %) used in these experiments was 47 H_2, 20 CO_2, 32 H_2O, 1 CO, 35 ppmv H_2S. In addition, 1 and 5 ppm AsH_3 or H_2Se were introduced in the gas stream. The tests were carried out at both 350 and 500°C. The preliminary results are shown in Figure 11. Analysis of the test results and characterization of the corroded test coupons are currently taking place.

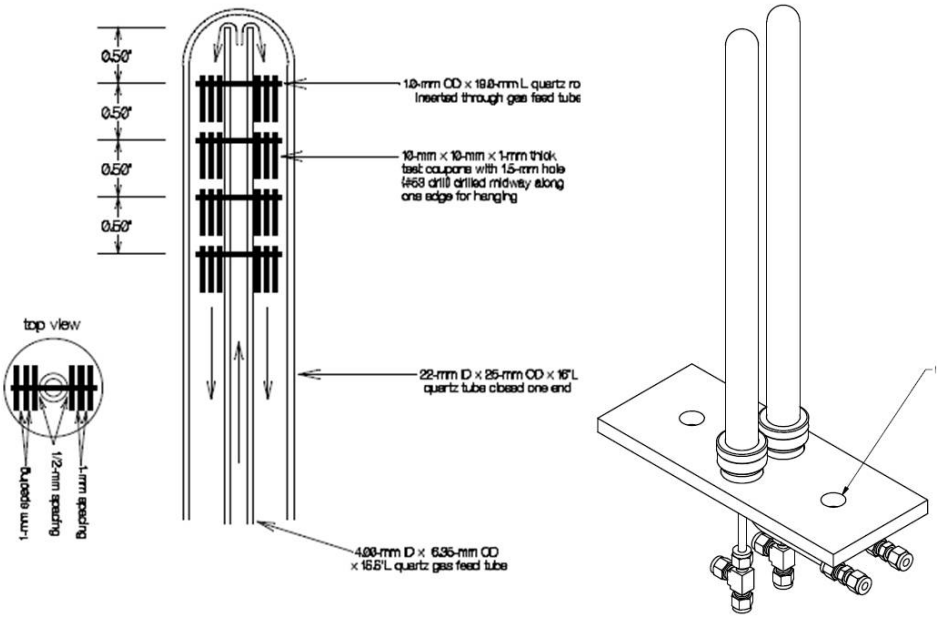

Figure 10: Membrane coupon exposure test fixture.

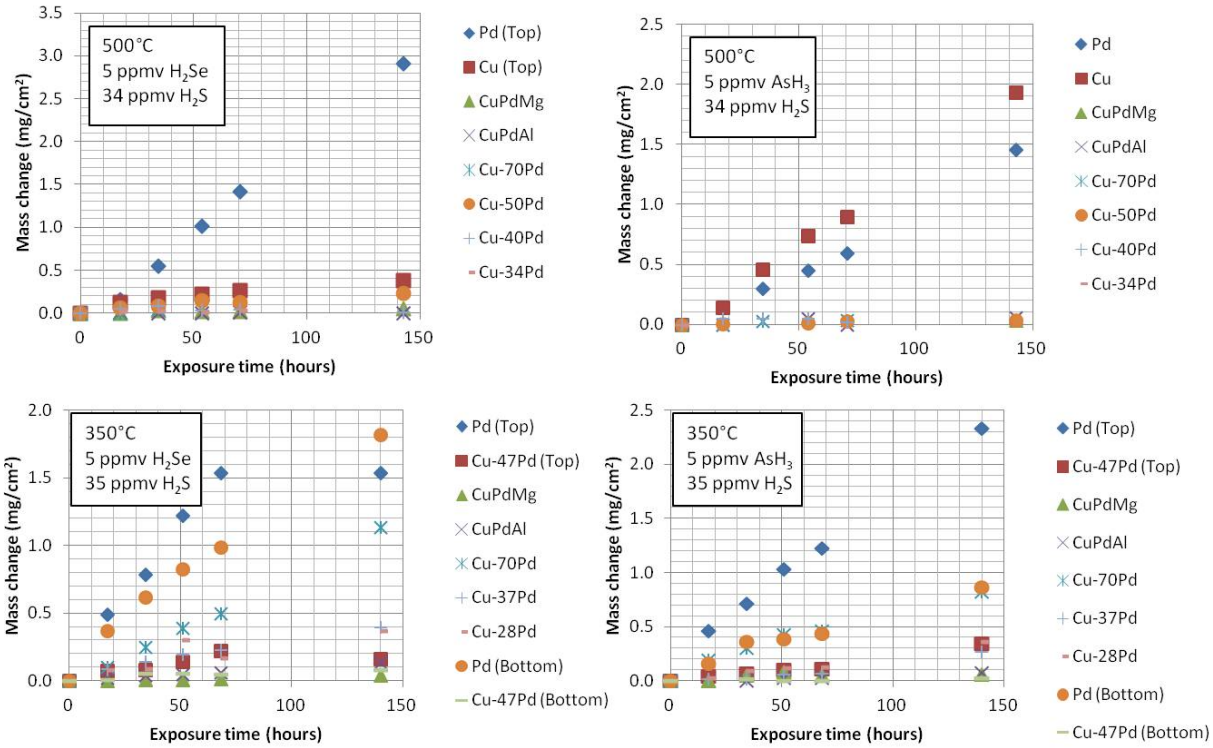

Figure 11: Preliminary results showing mass change of the membrane alloy coupons in syngas containing AsH_3, H_2Se and H_2S at 350 and 500°C.

Membrane Coating Development

A new protective coating approach for protecting dense metal-based hydrogen separation membranes, utilizing an ultrathin, protective surface layer to selectively prevent detrimental gas species from attacking and degrading the membrane surface, was conceived and evaluated. The coating is designed to repel gas species like H_2S that are highly damaging to a metal membrane surface while allowing hydrogen and other more benign gases to pass to the surface. This coating is applicable to a variety of metal-based membranes including both Pd and non-Pd alloys. Preliminary laboratory testing was carried out during FY13 using a prototype membrane which consists of a precursor monolayer coating applied to a palladium substrate. The prototype membranes (6 samples, 19 mm diameter by 100 µm thick) were delivered to a private company for coating and returned to NETL for testing.

The coating on the prototype membrane samples represents the initial deposition layer which has not been activated for H_2 selectivity/H_2S repulsion. Therefore, the initial coating is predicted to be essentially impermeable to all gases including H_2. The initial laboratory testing was designed to verify this predicted effect. During FY13, five Pd membranes with the precursor coating were tested under a number of conditions including H_2 at several temperatures and H_2 with 1000 ppm H_2S. Figure 12 compares the pure H_2 flux performance for the five samples at 350°C and 16 psig.

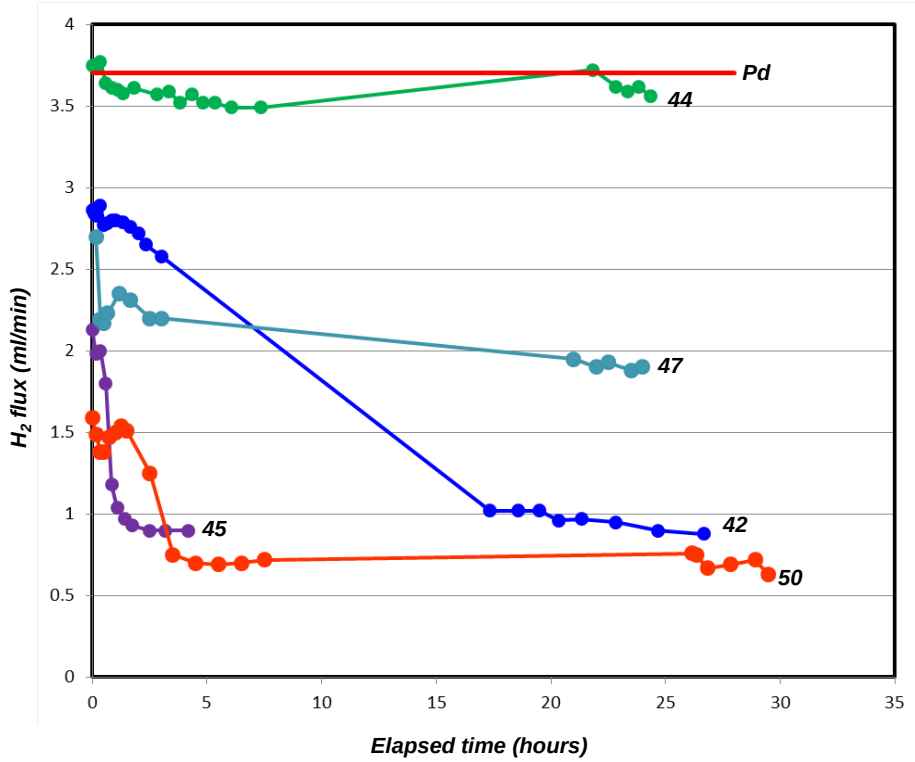

Figure 12: Comparison of hydrogen flux trends for precursor coated Pd at 350°C.

Samples 42, 44 and 47 were exposed to H_2 immediately upon reaching 350°C while 45 and 50 were held overnight at 350°C under Ar before exposing them to H_2. The wide range of flux values observed after steady state was reached suggests that the coatings vary significantly in the degree of surface coverage and/or flaws. The performance of 44 which was essentially the same as the baseline Pd suggests that this coating was very poor and had very little effect on permeability. Samples 45 and 50 were intended to be duplicate runs to verify the overnight "Ar annealing" effect. These samples performed similarly; both quickly equilibrating to a flux slightly below 1 ml/min. Samples 42 and 47 fell in between. One possible

explanation for the observed slow decline before reaching equilibrium is that the coating contains excessive defects through which H_2 can pass. The coating could be restructuring during the early part of the test period, both under Ar or H_2, blocking some defects resulting in a declining flux. However, other mechanisms could be conceived that could lead to similar performance.

Following the 350°C test period, three samples were stepped through higher temperatures under H_2. Sample 42 failed when the temperature was increased to 400°C. The failure, observed by SEM, appeared to be due to cracking near the seal area. Sample 45 was tested for five days up to 550°C. After testing at 550°C, the membrane was returned to 350°C. The permeability returned to the initial steady state flux value. This result suggests that the coating does have thermal stability under H_2 up to 550°C, however, this result needs to be verified with further tests.

Following testing under clean H_2 conditions, two of the coated samples, 47 and 50, were exposed to 1000 ppm H_2S in H_2 at 350°C for 24 hours. Because of the flawed coating suggested by the H_2 performance testing, it was expected that the membranes would degrade due to H_2S attack of the Pd. For both samples, the flux steadily dropped with exposure time as a Pd_4S surface corrosion layer grew in thickness. Following the tests, the samples were examined to determine if the coating had any effect on the surface corrosion layer. By optical microscope examination, no differences were detected for 47 versus what would be expected for an uncoated Pd membrane. However, sample 50 had several small areas that remained reflective as compared to the dull gray Pd_4S corrosion layer. These areas were examined by SEM and found to be free of any sign of bulk corrosion buildup as show in Figure 13. This result suggests that the coating does have the ability to prevent H_2S from attacking the Pd surface. It is not yet known specifically why this area was protected. Possibilities include an area of high perfection monolayer coating or a multilayer coating.

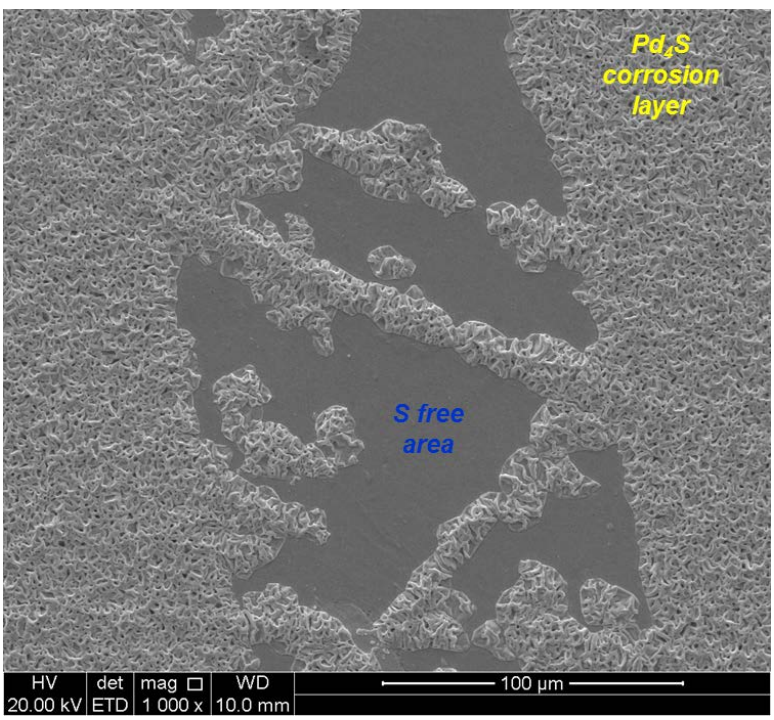

Figure 13: SEM image of sample 50 showing corrosion free region on the sample surface. EDS shows only Pd and C in the S-free areas.

Major Accomplishments and Key Findings

Overall the test series results suggest that the precursor coatings were flawed and inconsistent resulting in substantial performance variability, however, three promising results were obtained from this test series. Four samples demonstrated a large flux reduction with three equilibrating at about the same value (20% of the flux of uncoated Pd) suggesting that the coating could function as expected if its quality was improved. One sample was heated to 550°C, held for duration of about 2.5 hours and cooled back to 350°C. The flux prior to and following the high temperature exposure was nearly unchanged demonstrating some thermal stability of the coating. In addition and more encouraging, the area observed to be unaffected by the 1000 ppm H_2S exposure suggests that the precursor coating does have the ability to prevent sulfur attack on the membrane surface.

NCCC Exposure Tests

NETL continues to evaluate the corrosion resistance of potential metallic membrane materials through coupon exposures at the NCCC in Wilsonville, Alabama in addition to in-house testing. The latest series was exposed during run R08 in 2012. To evaluate the membrane material's corrosion resistance, sample coupons of selected materials were installed in the head (dust-free side) of the high temperature, high-pressure filter on the Transport Gasifier train during R08. At this location the syngas contains ~250 ppmv H_2S as well as the full suite of other coal-derived contaminants. The exposure temperature is about 400°C (750°F). The current coupons include one Pd-based alloy that has demonstrated H_2S tolerance in other studies, three super-permeable pure metals and ten primarily Fe-based structural alloys (not yet analyzed). Post-exposure evaluation is continuing, however, some findings and observations follow.

An fcc-structured Pd-Au-Ag alloy, discussed in previous reports, was exposed at the NCCC. Post exposure analysis by XRD and SEM showed that the surface was thickly covered with bulk corrosion. The corrosion layer appears to consist of primarily of two compounds; islands of Pd-arsenide on a continuous As-substituted Pd_4S layer, Figure 14. This result is consistent with the results for other similar Pd-based materials and suggests that fcc-structured Pd-based alloys are not likely to be practical in this type of environment. This result also reinforces the value of this type of testing in that this alloy showed potential in a "clean" lab test environment.

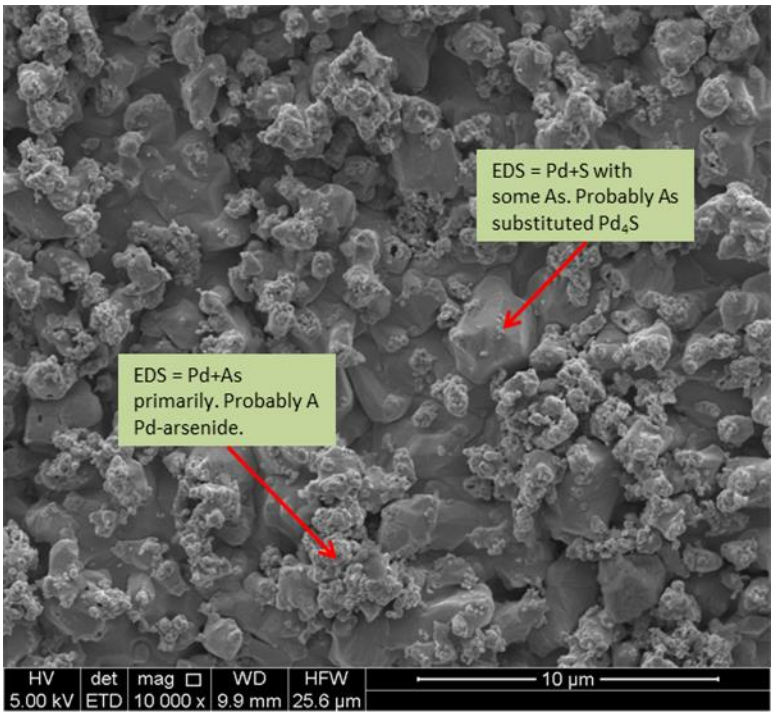

Figure 14: SEM image of the surface of an fcc-structured Pd-Au-Ag alloy coupon exposed during R08.

The super permeable metals and alloys (tantalum, niobium, vanadium, etc.) are promising for separation applications due to their permeability and lower cost, but they are very susceptible to surface degradation. Therefore, surface coatings that can protect these metals/alloys from corrosion while retaining good permeability are of interest. Several uncoated coupons (Ta, Nb, and V) of these materials were also exposed during R08 to provide a performance baseline for this coating research. Figure 15 shows an SEM image of the surface of one on these coupons following exposure. For this material, tantalum, the surface was thickly covered with a layer of corrosion products consisting only of oxides. No sulfur was detected. A somewhat similar result was found for V with a much thinner oxide deposit. The Nb sample was lost in the gasifier. These results nicely illustrate the different degradation issues that need to be solved for different groups of materials. Results such as these can only be achieved using actual coal-derived syngas and are extremely important in guiding hydrogen separation alloy development efforts.

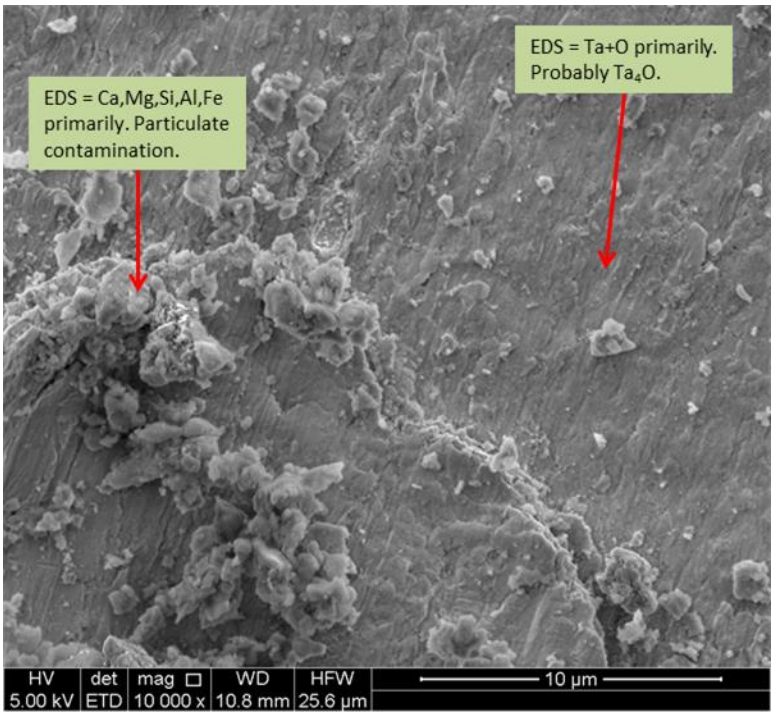

Figure 15: SEM image of the surface of a baseline Ta coupon exposed during R08 showing surface oxides and abundant surface particulate contamination.

Significant Findings

Membrane alloy coupon exposures were carried out at the NCCC under actual gasifier conditions using coal-derived syngas containing the full suite of typical gas phase impurities. The current test results show that Pd-based alloys are attacked by primarily sulfur and arsenic as previously observed while Ta and V were attacked by oxygen resulting in oxide covered surfaces. The results of these exposures clearly illustrate the different degradation issues that need to be solved for different groups of materials. Results such as these can only be achieved using actual coal-derived syngas and are extremely important in guiding hydrogen separation alloy development efforts.

Thermocatalytic Pathways

Fundamental Catalyst Research

Computational Materials Design

Conversion of natural gas to aromatics under non-oxidizing conditions represents a promising but very challenging technology. In particular, the possibility to achieve direct aromatization of methane to benzene under mild conditions with high selectivity and yields represents today one of the difficult unsolved problems in hydrocarbon chemistry.

Since discovery of catalytic transformation of CH_4 to benzene using Mo/H-ZSM-5 catalysts (Wang. T; Tao, L; Xie, M; Xu, G. Catal. Lett.1993, 21,35) significant efforts have been dedicated to optimization of this process and several review papers summarize the results in this area (Y. Xu, et al., J. Catal. 216 (2003) 386, Yu. I, M. Ichikawa, Catal. Today 71 (2001) 55, Skutil K. Fuel Proc. Techn.87 (2006), 511). A common issue recognized in all these studies is the difficulty to identify robust catalysts which can achieve activation of CH_4 under mild conditions, characteristic due in part to the high thermodynamic stability of the CH_4 molecule with no dipole molecule and no molecular asymmetry.

Among various methods considered to date conversion of CH_4 to benzene using Mo/H-ZSM-5 catalysts under non-oxidizing conditions continue to represent the optimal alternative. In this system the Mo/H-HZSM-5 displays a bifunctional role with dehydrogenation and acid sites. Within the conversion process, in the initial activation phase, the MoOx phase undergoes successive transformations leading either to molybdenum carbide or oxycarbide phases. It is believed that this molybdenum carbide system is the active specie where methane activation takes place with formation of C_2H_4 or C_2H_2 species. Further oligomerization of these species leads to formation of various aromatics (benzene, naphthalene). The fundamental limitation in this process is related to deactivation of MoCx sites due to increased coke formation. In turn this leads to a limited lifetime of the Mo/H-ZSM-5 catalyst with direct economic negative impact.

Understanding both the reaction mechanism for CH_4 activation followed by the set of C-C coupling and aromatization reactions during the entire evolution and phase transformation from MoOx to MoCy or MoOzCw phases represents another major challenge. For this purpose it is essential to determine the general factors such as the nature of MoOx sites and its chemical reactivity, to understand the dependence of the activation properties of CH_4 on MoOx and MoCy specie on various material parameters such as the Si/Al ratio or the types of additives and finally to determine the sequence of C-C coupling reactions leading ultimate to benzene formation. Only by understanding the main factors that favor transformation and reactivity of CH_4 to benzene as connected to MoOx→MoOy phase transformation additional steps can be taken to rationally modify the corresponding reaction pathways and ultimately, to achieve aromatization under mild conditions.

A first prerequisite of both these two tasks is represented by identification of the sites where formation of the active species resides and phase evolution from MoOx to MoCy takes place. Previous experimental studies performed in Iglesia group (W. Li, et al., J. Catal. 191, 373 [2000], R. W. Borry, et al., J. Phys. Chem. B 1999, 103, 5787, Y.H. Kim, et al., Microp. Mesopor. Mat. 35-36 [2000] 495) have shown that the exchange of Mo species in ZSM-5 catalysts takes place at temperatures above 773 K, where the MoOx sublimates and wets the surface of the ZSM-5 catalyst followed by diffusion into the pores of the catalyst. Within the ZSM-5 pore structure the MoOx species can interact with the existent acidic site resulted upon Al substitution at various Si sites. This reaction step leads to formation of different types of Mo-oxo species summarized in Figure 16 and Figure 17. Specifically, result obtained by Iglesia and his collaborated indicate that formation of either a dimeric $(Mo_2O_5)^{2+}$ specie (see Figure 16) or a monomeric $(MoO_2)^{2+}$ specie resulted upon reaction of $(MoO_2(OH))^{+}$ species with a zeolite OH group (see Figure 17) are possible.

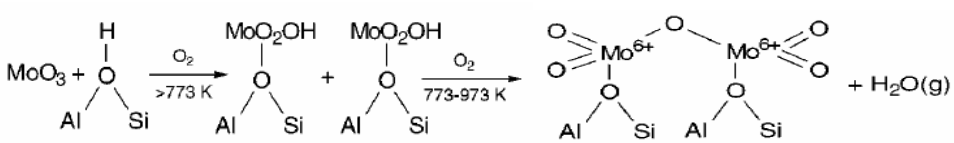

Figure 16: General processes for Mo exchange in ZSM-5 structure with formation of $(Mo_2O_5)^{2+}$- oxo clusters according to Iglesia, et al., J. Phys. Chem. B. 1999, 103, 5787.

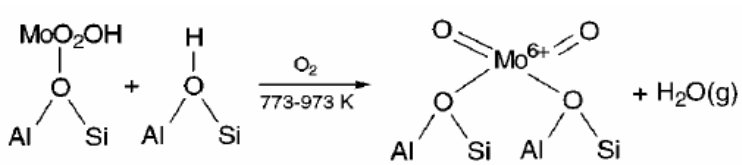

Figure 17: General processes for Mo exchange in ZSM-5 structure with formation of monomeric $(MoO_2)^{2+}$ oxo cluster bridging two acid sites and water according to Iglesia, et al., J. Phys. Chem. B. 1999, 103, 5787.

Consequently, a first initial task for understanding the reactivity of CH_4 in Mo/HZSM-5 structure is to determine the nature and location of the Mo-oxo species at various acid sites within the ZSM-5 structure. To date, there is no experimental information to indicate which specific locations or sites in the ZSM-5 network are involved for the indicated formation of Mo-oxo specie which in turn depends on location of single and double Al substitutions in Si-O framework structure.

A novel approach that can be used to determine such information and became available only in recent years is represented by the use of computational chemistry methods. Such capabilities allow a systematic analysis of the energetic differences between Al sites either in the form of single or multiple substitutions, description of their structural, energetic and electronic properties of the MoOx species as well as the activation properties of CH_4 at such sites. In the present work this approach based on the use of first principles density functional calculations was used to determine which specific sites in the unit cell of ZSM-5 are responsible for single or double Al substitution where the monomeric or dimeric Mo-oxo species can be formed. Identification of such sites is essential because the location of Al sites will determine initial location of the Mo-oxo species which in the end are responsible for the observed catalytic activity and activation of CH_4 in ZSM-5.

In order to identify the stability of Al double substitutions in the ZSM-5 unit cell first principle density functional calculations were used in conjunction with periodic slab models. The periodic nature of these models ensures that the long range interactions existent in SiO_2 framework are appropriately considered. These models eliminate the limitations of the cluster models which are not capable to incorporate reliable, long range interactions present in a bulk oxide material and to account properly for consideration of the confinement effects determined by the porous structure of ZSM-5. A second important aspect was inclusion of long range dispersion interactions within the density functional theory (DFT) formalism. Such interactions were also missing from many of previous cluster studies. Overall, these new capabilities allow for a more accurate description of both the crystalline structure of ZSM-5 and of its nano confinement effects produced upon weakly bonded systems such as CH_4 interacting with the ZSM-5 framework.

Calculations were performed in the current work using the Quickstep module of the CP2K program (VandeVondele, J.; Krack, M.; Mohamed, F.; Parrinello, M.; Chassaing, T.; Hutter, J. *Comput. Phys. Commun.* 2005, *167*, 103). These calculations were based on a mixed Gaussian and plane wave formalism. The exchange-correlation functional used in these studies were based on Perdew-Burke-Ernzeh functional while the dispersion interactions were described using DFT-D2/DFT-D3 methods of Grimme (Grimme, S. *J. Comput. Chem.* 2006, *27*, 1787 ; Grimme, S.; Antony, J.; Ehrlich, S.; Krieg, H., *J. Chem. Phys.* 2010, *132*, 154104).

The first set of calculations focused on identification of the relative energetic differences among various Al substitutions at different Si sites. This approach and the corresponding results are summarized in Figure 18(b) for the case of the orthogonal bulk structure of ZSM-5 (see Figure 18[a]).

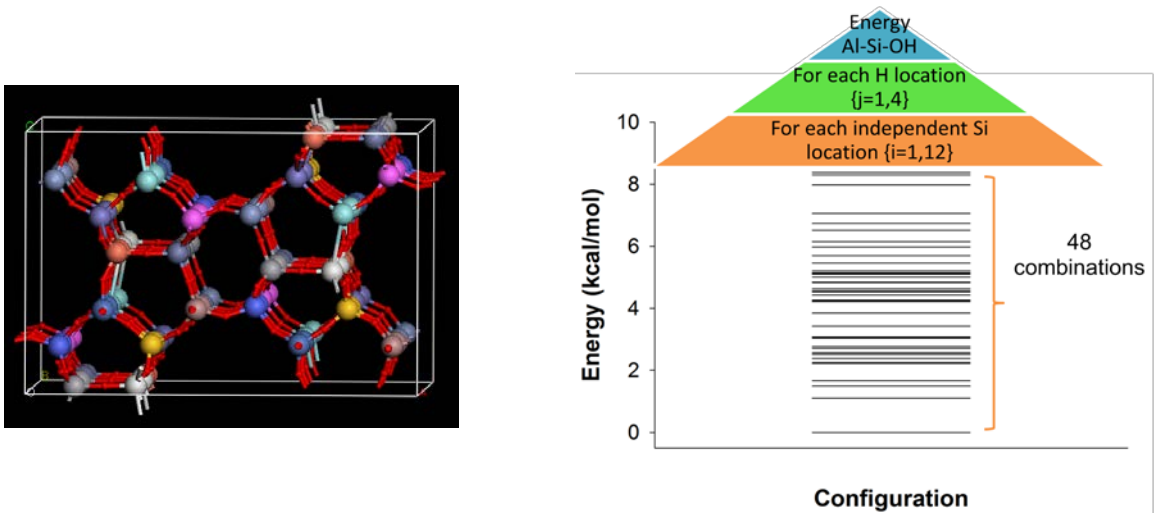

(a) (b)

Figure 18: (a) The orthogonal ZSM-5 bulk structure with Pnma space group and its 12 independent locations where Si atoms can be substituted with Al. (b) Relative energies of the 48 different combinations of Al-OH-Si sites resulted upon Al substitution. Charge compensation was considered by including a proton adsorbed at a bridging oxygen site near the Al substitution.

The results indicated in Figure 18(b) indicate the stability of various Al substitutions in ZSM-5 structure at low coverage. It can be seen that not all the sites have equal energies and consequently Al substitution is not expected to be random in practical applications.

This analysis has been also extended to the case of double Al substitutions located in close proximity. For this purpose, the Lowestein rule (Am. Mineralog. 39, 1942) related to the maximal number of substitutions was used. According to this rule, for a given Al substitution it is not possible to achieve another substitution in the first Si atom shell. Given this rule the research was focused on identification of double Al substitutions located either as next nearest neighbors (NNN), i.e., Al-O-Si-O-Al sites or as next, next, nearest neighbors (NNNN), i.e., Al-O-Si-O-Si-O-Al. In order to achieve this analysis a general software package has been developed to build all combinations of NNN and NNNN double Al substitutions in the bulk unit cell of ZSM-5. The general algorithm developed in this case is summarized in Figure 19 for the case of NNN substitutions.

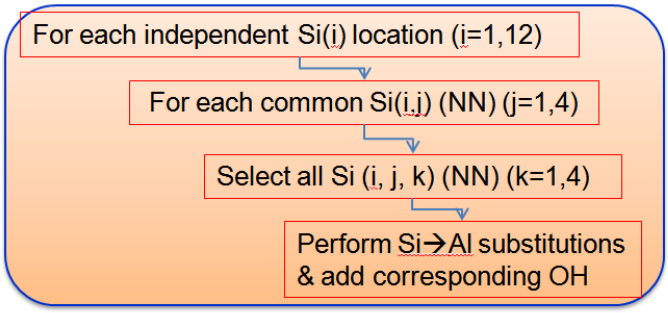

Figure 19: General algorithm developed for identification and energy evaluation of Al double substitutions in ZSM-5 framework.

According to this figure, for each of the 12 independent locations of Si atoms in the asymmetric part of the unit cell of ZSM-5 having Pbca symmetry (denoted as Si(i), i=1,12 sites), all their first nearest Si neighbors (NN) (Si(i,j)) were considered together with their own NN neighbors set of Si atoms Si(i,j,k), i=1,12; j=1,4; k=1,4). For the indicated sites the corresponding Al substitutions were performed. The overall charge of the supercell was maintained neutral by adding corresponding protons at the bridging O bonded to Al sites. The resulted number of configurations determined using the above algorithm is 142 in the case of Pbcn and for this entire set of configurations their total energies were evaluated used first principles DFT calculations.

This approach allows identification of the energetic differences resulted among various double Al substitutions. The corresponding total energies of the set of 142 configurations are shown in Figure 20. As indicated in this figure there are several sites with close energies where distribution can take place. As a result, in practical applications it is expected that several such sites will be involved in Al double site substitutions.

Examples of NNN configurations with Al double site substitutions in the ZSM-5 structure are shown in Figure 21.

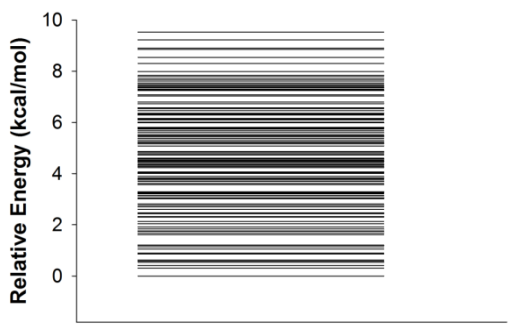

Figure 20: Relative energies of the 142 configurations of double Al substitutions in ZSM-5 structure.

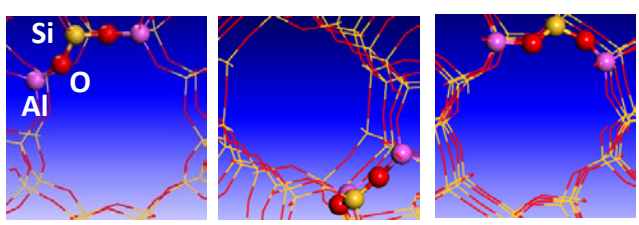

Figure 21: Configurations of ZSM-5 with double Al site substitutions.

The importance of the results obtained is that the previous gap in scientific knowledge related to specific location of single and double Al sites within ZSM-5 structure was addressed based on the use of computational chemistry methods. Moreover, the availability of the location and relative stabilities of single and double Al sites within ZSM-5 structures allows extension of the theoretical investigations to the next step, identification of the thermostability of the Mo-oxo clusters and the role played by these clusters in chemical activation of CH_4. This information is essential in order to understand processes such as CH_4 activation and the coupling CH_x-CH_y reactions of the resulted fragments.

Experimental Catalyst Design and Evaluation

Conventionally-Structured Catalyst

The goals of efforts in the catalyst synthesis and reaction testing area were to compare the reactivity of conventional Mo catalysts to a non-carbide ZnO-based catalyst under equilibrium reaction conditions backed with fresh and post reaction catalyst characterizations.

Mo-based catalyst is a conventional carbide phase used in methane-to-aromatic reactions but coke formation during the reaction results in a fast deactivation. Additionally, a problem with its regeneration where a multi-step regeneration is required (burning carbon and carburization) adds to its overall problems with commercializing DHA reaction into useful high value aromatic chemicals. ZnO based catalyst is proposed to offer a stable catalyst over reaction time and can be easily regenerated.

FY13 Accomplishments:

A detailed literature survey on converting methane into aromatic species (benzene, toluene, ethylbenzene, and xylene) was conducted, with a focus toward the methane dehydro-aromatization reaction. Manuscripts and their results were summarized according to the type of catalyst used and promoter type, reaction conditions used, and catalyst synthesis methods. An EndNote-based literature database was compiled, and this database was made available for other researchers on the team.

Modifications to the fixed bed reactor (FTR) in B25-204 were completed in order to perform methane aromatization experiments. Modifications included the addition of a heated, direct transfer line between the reactor and an on-line gas chromatograph (GC), in order to avoid the condensation of liquid products formed prior to entry into the GC system. Also, an analytical method for analysis of the reactor effluent containing unconverted methane, gaseous (C1-C5 paraffins and olefins) as well as liquid (benzene and toluene), was developed. Due to the temperature limitation of the FTR (T_{max}=700 °C), another micro reactor (NPT, B25-213) was prepared and is being modified. A new on-line GC was connected and calibrated, but the same basic analytical method was used, with the exception of adding toluene to the calibration component set for this GC.

The goal of the catalyst development work is to use conventional gas conversion catalyst systems as a baseline for conversion efficiency, as well as confirm where traditional catalysts fall short in terms of lifetime, conversion efficiency, and regeneration. It is believed that a catalyst based on a ZnO active phase could be more stable than Mo_2C catalyst in the long run and regenerate more easily. Efforts also focused on the ease of regeneration and the degree to which catalyst activity is maintained following the regeneration cycles.

Accomplishments, Mo-based catalyst include:

- Optimize Mo loading, reaction temperature, choosing the right ZSM-5 support with optimal SAR ratio, and reaction space velocity.
- Addition of promoters (Zn, Fe, Ru, Os) to increase catalyst stability.

Accomplishments, ZnO-based catalyst include:

- Evaluation of the regeneration performance of deactivated Zn catalysts under methane for multi cycles.
- Investigation of the effect of light hydrocarbons addition (ethane and propane) to decrease the activation temperature of DHA reaction.
- Investigation of the effect of different promoters to stabilize ZnO.

- Investigation of the effect of steam to stabilize ZnO and help in coke reduction during reaction Mo_2C baseline catalyst. Three different ammonium based ZSM-5 zeolite with different SARs 23, 50 and 280 were loaded with a fixed metal loading (6wt% Mo) after converting them to H-ZSM-5.

These three catalysts 6wt% Mo/ HZSM-5 with different SAR= 23, 50, 280 were tested for their ability to convert methane into benzene at 700 °C, 1 atm pressure, and 3000 cc/g/h. It was determined that the catalyst with SAR 50 was the most active and selective toward benzene formation (Figure 22). This zeolite (SAR 50) was chosen as the active baseline support.

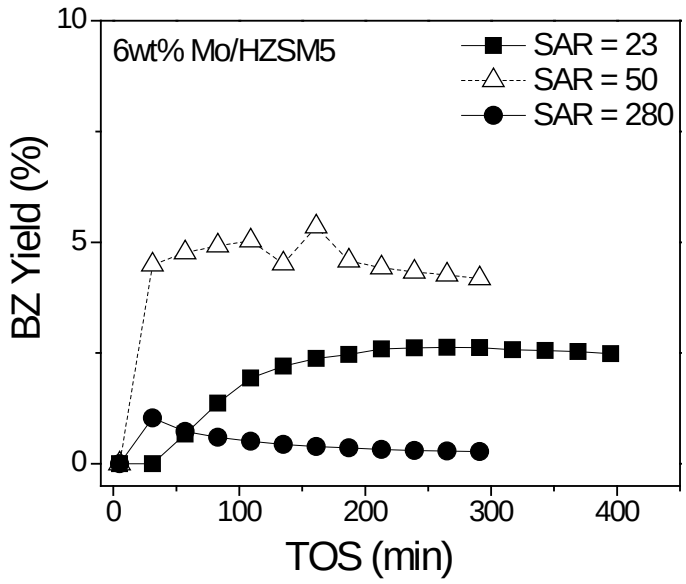

Figure 22: Effect of Si/Al ratio (SAR) on the benzene yield.

The effect of different space velocity was evaluated using (1500, 3000, and 6000 cc/g/h) the 6wt% Mo/HZSM-5 (SAR50) at 700 °C. The space velocity was varied by changing the total flow rate while keeping the catalyst mass unchanged. The optimum space velocity was found to be 3000 cc/g/h. The results of the space velocity tests are shown in Figure 23.

To find the total number of acidic sites, as well as the effect of SAR on zeolite acidity and the effect of Mo loading on these sites, ammonia temperature programmed desorption (NH_3-TPD) was performed on six HZSM-5 samples (SAR 23, 50, 280) with and without Mo loading. The results from the ammonia TPD are summarized in Figure 24. The total number of acidic sites decreases with increasing the SAR, with the number of acidic sites in this order: SAR 23 > SAR 50 > SAR 280. However, the performance (benzene, toluene, and xylene [BTX] selectivity) was in this order: SAR 50 > SAR 23 >>> SAR 280. A balanced number of acidic sites are required for the desired reaction. There was almost negligible activity with SAR 280 which has significantly lower acidic sites compared to the other two zeolites. Although, the SAR 23 is highly acidic (in terms of number of acidic sites) compared to the SAR50, but the product selectivity with the SAR 23 was slightly lower than that of the SAR 50 (both containing 6 wt% Mo). Therefore, it can be concluded that the zeolite supporting Mo has to be highly acidic but reaches a limit where being extremely highly acidic is detrimental. It should be noted that the method used here to determine the number of acidic sites does not differentiate between the type of acidity (Lewis or Bronsted); it simply gives the sum of the amount of both Lewis and Bronsted acidic sites. It is planned to use pyridine adsorption in diffuse reflectance infrared fourier transform spectroscopy (DRIFTS) to distinguish the Lewis acid sites from the Bronsted acid sites. The infrared spectra of pyridine adsorbed

onto the catalyst surface will show different IR peaks for Lewis acidities and Bronsted acidities. The results will help correlate the type of acidity with the selectivity and optimize the pretreatment of the zeolite accordingly for better activity and selectivity.

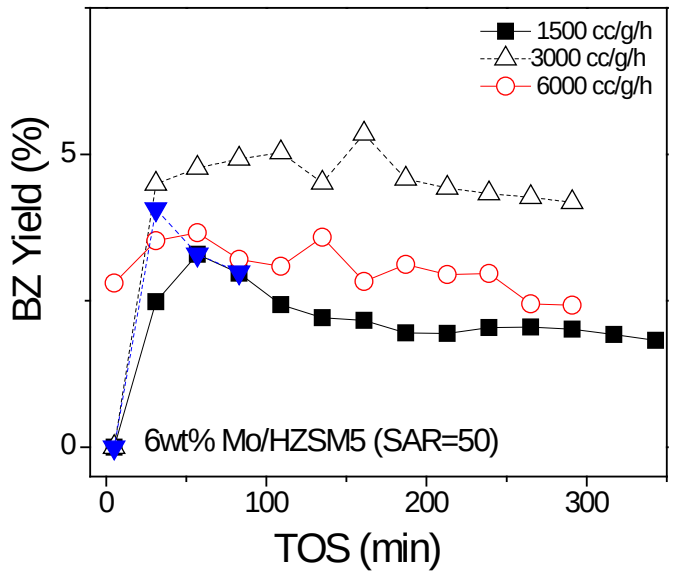

Figure 23: Effect of different space velocity on the benzene yield.

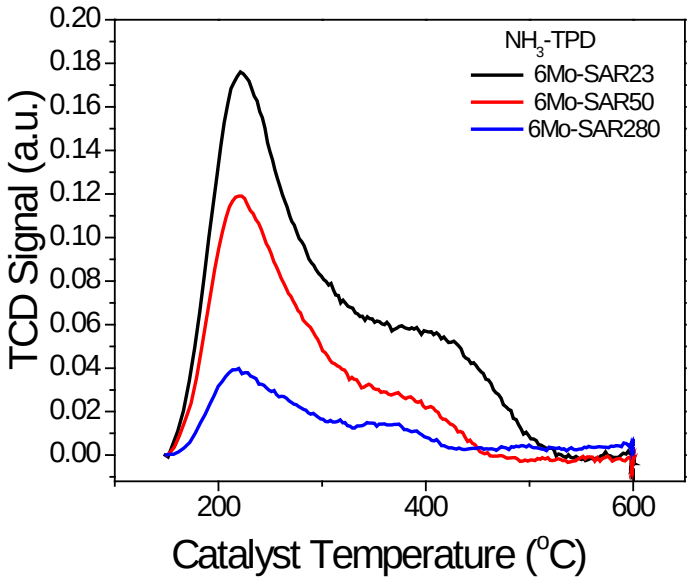

Figure 24: Ammonia TPD of three zeolite-based Mo catalyst.

Promoted Mo Catalysts

A series of molybdenum-based catalysts (MoZnM/ZSM-5 or MoM/ZSM-5, where M = Fe, Ru, or Os) were studied for the methane DHA reaction. Those catalysts are summarized in Table 1. The goal was to minimize coke formation and increase catalyst life time while maintaining catalyst activity and selectivity. Transition metal promoters can provide hydrogenation sites to the coke, having H_2 dissociation dominate over the methane decomposition, hence controlling coke formation.

Table 1: Summary of Mo-Based Catalysts Synthesized and Tested for Methane Conversion

Catalyst	T co	Mo wt%	Zn wt%	M wt%	Comments
Mo	700	4			• Mo based catalyst promoted with different transition metals) • Mo shows the highest activity and selectivity for benzene; however the deactivation rate of Mo is lowered (need long runs to confirm) • Ru promoted catalyst shows a better performance compared to Moan • H-ZSM-5 shows a negligible activity with trace amounts of BZ • Conversion of <1% and BZ selectivity of < 0.5%
MoZn		4	1		
MoZnFe		4	1	0.3	
MoZnRu		4	1	0.3	
MoFe		4	0	0.3	
MoRu		4	0	0.3	
SAR50					
Mo4@800C	800	4			• Increasing the reaction temperature 700 to 800°C results in fast deactivation of the catalyst • Mo shows a higher activity than with Zn and Ru
MoZnRu		4	1	0.3	

Surface properties of some of the Mo-based catalyst are listed in Table 2. As expected, surface area as well as pore volume of the doped Mo catalysts decreased with metal doping. Methane conversion results from different promoted Mo catalysts are shown in Figure 25. There was no significant difference found in the activity for six hours of experiments, with methane conversion settling around 6%. The benzene selectivity from the doped Mo-catalysts was lower than that of the Mo only catalyst, except in the case of MoZnFe catalyst. Longer experiments are necessary to see any effects of transition metal doping on the long-term activity and selectivity.

Table 2: Surface Properties of Mo-Based Catalysts

Catalyst	Metal(s) Loading (wt%)	BET Surface Area (m2/g)	Total Pore Volume (cc/g)	Average Pore Diameter (A)a
HZSM-5	--	327	0.208	33.30
Mo/HZSM-5	Mo(4)	310	0.195	34.93
MoZn/HZSM-5	Mo(4)Zn(1)	281	0.184	36.28
MoZnRu/HZSM-5	Mo(4)Zn(1)Ru(0.3)	266	0.177	37.41

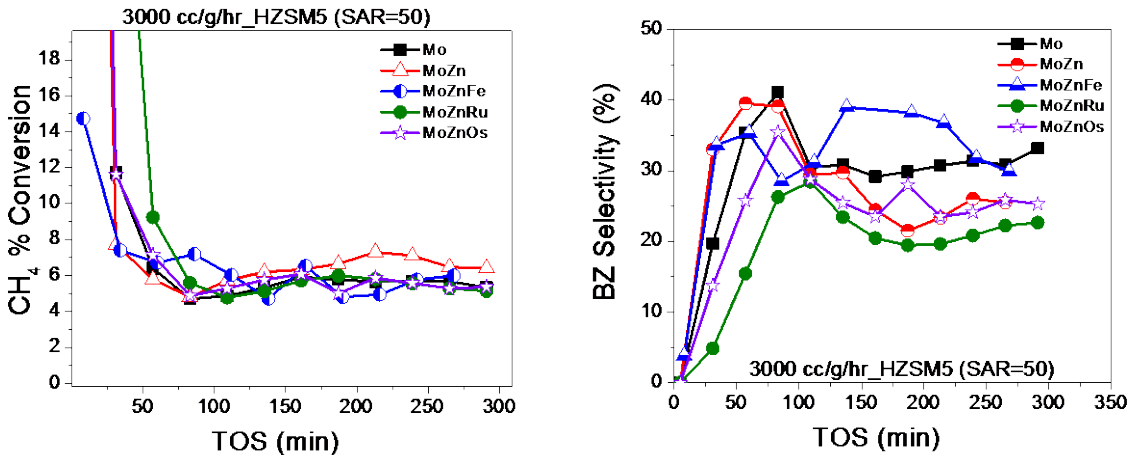

Figure 25: Methane conversion and selectivity from MoZnM/ZSM-5 catalyst (reaction temperature 700°C and WHSV 3000 cc(STP)/g/hr)

ZnO -Based Catalyst

A literature survey showed that Zn/HZSM-5 catalyst was used for aromatization of light alkenes and in methanol to gasoline (MTG) processes. A series of traditional Zn based catalysts (Zn/ZSM-5, where M = La, Zr, Ce or Y) were prepared and evaluated for methane dearomatization (MDA) reaction (the formulations are shown in Table 3). The goal was to determine whether addition of La, Zr, Ce and/or Y could promote the BTX selectivity and increase the stability of Zn/H-ZSM-5 catalyst for the MDA reaction.

Table 3: Zn-Based Catalysts Studied for MDA Reaction

Catalyst	Zn wt%	La wt%	Zr wt%	Ce wt%	Y wt%
Zn	3				
ZnLa	3	0.3			
ZnLa	3	1.0			
ZnZr	3		0.3		
ZnCe	3			0.3	
ZnCe	3			1.0	
ZnY	3				1.0

The methane conversion and benzene selectivity over the Zn-based catalysts are shown in Figure 26. All promoted Zn catalysts show a higher activity than the unpromoted catalyst. However, the selectivity of Zn is slightly better than promoted Zn catalysts. The ZnCe shows the highest benzene selectivity among promoted catalysts.

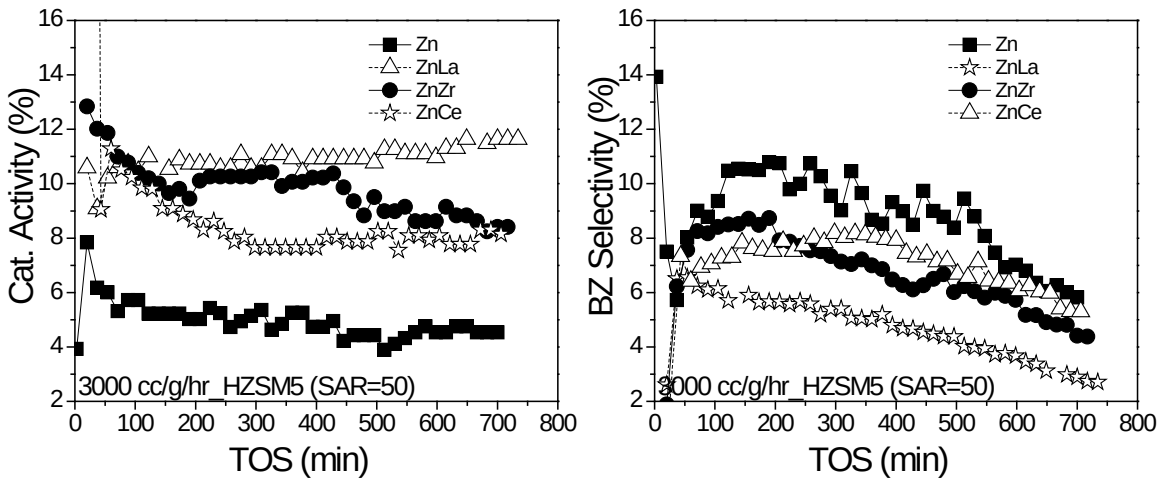

Figure 26: Effect of promoters on the activity and benzene selectivity of Zn (3wt%) supported on H-ZSM-5 catalyst during MDA reaction at 700°C, 1 atm, and 3000 cc/g/h.

The concentration of promoters (La, Ce and Y) was increased from 0.3wt% to 1.0 wt% on 3wt%Zn/HZSM-5. Figure 27 shows the catalytic performance of Zn_3, Zn_3La_1 and Zn_3Ce_1. While the Zn_3Ce_1 catalyst showed the highest activity, it also experienced a drop in selectivity over time. However, the activity of this material did not appear to decrease (and actually showed a slight increasing trend) over the duration of the test. Future test plans will include a parallel run using the best performing catalyst(s) in a membrane reactor to determine the effect of hydrogen removal on catalyst performance.

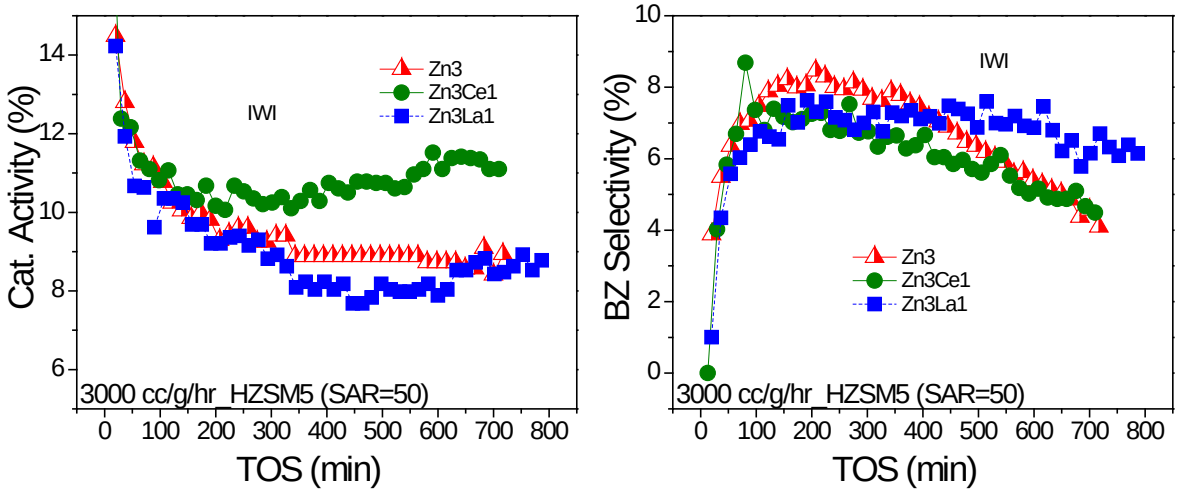

Figure 27: Effect of increasing promoters on the activity and benzene selectivity of Zn (3wt%) supported on H-ZSM-5 catalyst during MDA reaction at 700°C, 1 atm, and 3000 cc/g/h.

New Synthesis Routes to Incorporate Metal Catalyst in ZSM-5

Another area of effort during this FY2013 was the preparation of ZSM-5 with similar SAR ratio of 50 as the first step using the different routes from literature. Mainly, the ZSM-5 material was prepared using the conventional hydrothermal methods (HT) which requires days at high pressure and temperature only to yield small quantities (less than 1 gram). The new approach, given in Figure 28, begins with optimizing the HT synthesis method and then switch focus to explore a microwave-assisted hydrothermal method

(MWAHT). Microwave-assisted preparation is expected to enhance the reaction rate between ZSM-5 precursors giving uniform and homogeneously nucleated particles having high crystallinity. In addition, the reaction time is expected to be dramatically reduced from days to minutes. The final step in the synthesis route is to incorporate Zn with or without other promoters during the ZSM synthesis.

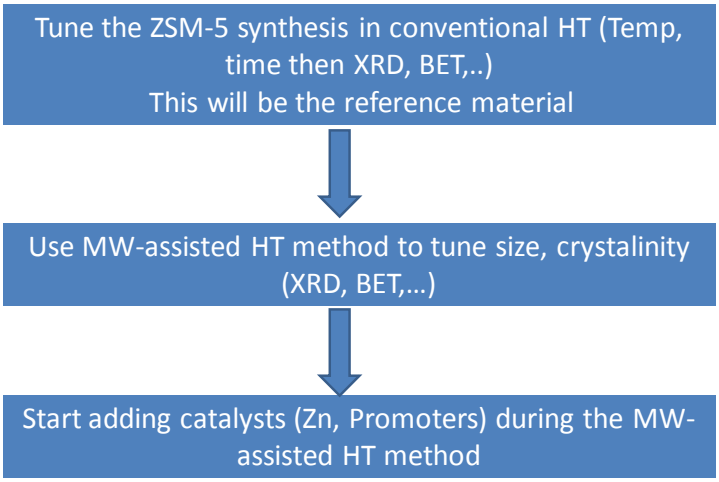

Figure 28: Plan for developing new Zn based catalyst using MWAHT method.

Figure 29 displays the XRD patterns of the initial synthesis runs compared to commercial ZSM-5. A conventional HT method was used in each run, with Method 1 being derived from *J. Nat. Gas Chem*, vol 21, 2012 and Method 2 derived from *Cat. Commun*, vol 10, 2009. The modifications to each method were to prepare the sample with a Si-t0-Al ratio (SAR) of 50. Each run was calcined at different temperature in air. Method 1 shows less crystallinity, even when a higher calcination temperature of 600°C is used. On the other hand, Method 2 shows an improvement in crystallinity, as shown by comparing the green curves at 550°C, by re-calcining the material for a longer time at 550°C. It is planned to apply the microwave-assisted synthesis method as a significant improvement to either of these two published methods.

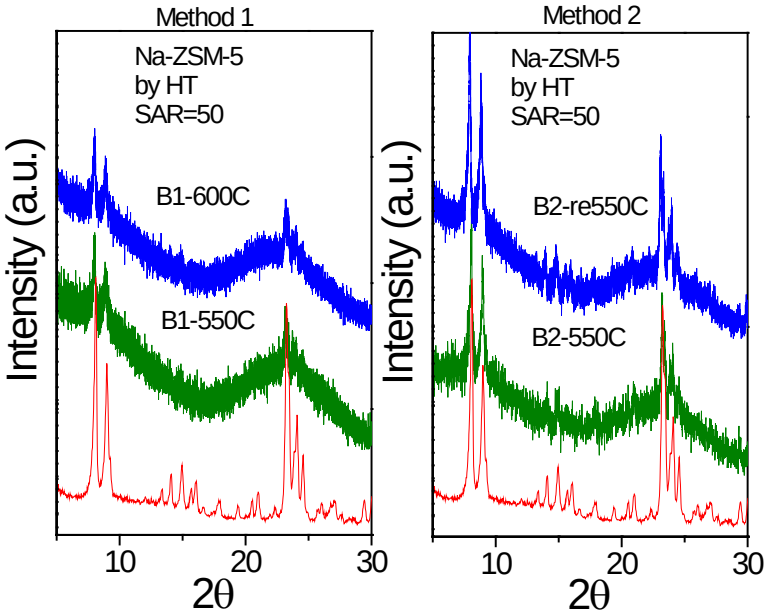

Figure 29: XRD patterns of calcined Na-ZSM-5 using different preparation methods.

Regeneration Behavior of Zn Based Catalysts for Methane Dehydroaromatization Reactions

Zn-based catalysts were evaluated to assess activity and selectivity towards aromatic compounds formation after multiple regeneration cycles in air. The Zn was loaded into the catalysts at two different Zn loadings (3% and 8%) as well as different SAR of 50 and 20 using incipient wetness impregnation (IWI) methods, two different Zn loaded catalysts were evaluated with 3 and 8 wt %. In addition, two novel nano-catalysts with nanoparticles of ZnO are embedded in the zeolite matrix with either SAR 50 and 20 with a constant Zn loading of 8wt%. Table 4 shows the catalysts that were evaluated and experimental conditions used.

Table 4: Catalysts Evaluated in the FT Reactor and Experiment Conditions Used

Catalyst	Catalyst properties			Experiment Conditions			
	Zn loading (wt%)	Method	SAR	WHSV scc/g/h	T_{rxn} °C	T_{reg} °C	No. of Cycles
Zn3-IWI	3	IWI	50	3000	700	600	3
Zn8-IWI	8	IWI	50	3000	700	600	3
Zn8-IWI	8	IWI	50	6000	700	600	3
Zn8-Pit	8	Pitt	50	6000	700	600	3
Zn8-Pit	8	Pitt	20	6000	700	600	5

Figure 30 shows that, as expected, more benzene yield was observed under lower weight hourly space velocity (WHSV) of 3000 cc/g/h compared to 6000 scc/g/h for Zn8-IWI catalyst. Maximum benzene yield was observed during the first cycle of each run and started to decay drastically during the second and third cycle, possibly due to loss of Zn. It is postulated that ZnO could be reduced to metallic Zn which can be vaporized slowly under reaction temperature and reductive atmosphere of H_2 and methane, as evidenced by the detection of CO_2 during the first cycle and at decreasing levels during the second and third cycle. Additional support for loss of Zn is the difference in concentration of Zn in fresh and after regeneration cycles (SEM/ energy dispersive X-ray [EDX]).

At low WHSV, no benzene was detected in the third cycle; however, at higher WHSV, no benzene was observed even during the second cycle using the Zn8-IWI catalyst. Toluene was only observed at lower WHSV up to the second cycle. Hydrogen yield increases and carbon balance deviates after each regeneration cycle due to decomposition of methane into carbon and hydrogen, mainly at 700 °C. Methane conversion starts high after each regeneration cycle (clean carbon free surface) but decays rapidly due to fast carbon coverage on the catalyst surface.

$$CH_4 \rightarrow 2H_2 + C$$

Yield trend of ethylene and propylene mirror imaged the yield trend of benzene possibly due to involvement of these species in the formation mechanism of benzene. Also the absence of Zn/ZnO from the catalyst surface possibly results in a major decrease in the dehydrogenation sites and decrease in the olefin species which is again involved in the benzene formation mechanism.

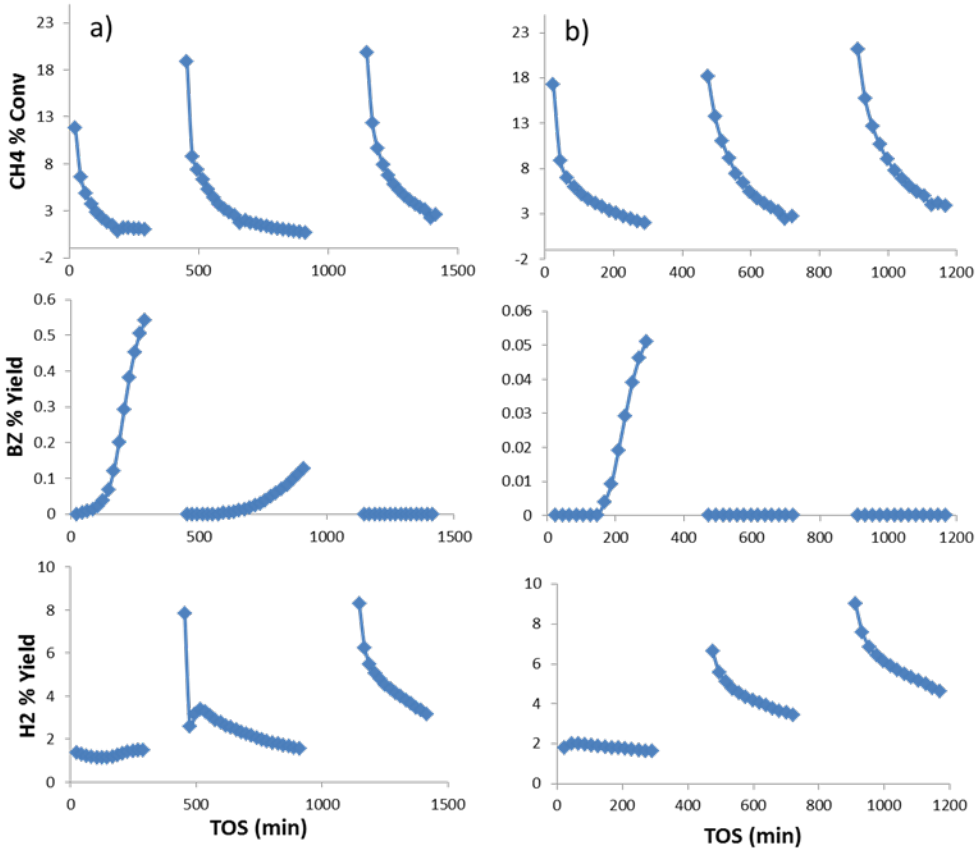

Figure 30: Performance of Zn8-IWI catalyst under similar reaction conditions but different WHSV of (a) 3000 and (b) 6000 scc/g/h.

Comparing the results for two Zn catalysts with different loading (8wt% vs. 3wt%) runs under similar reaction conditions reveals the following, as shown by Figure 31.

- Higher methane conversion and hydrogen yield were observed on the 8wt% catalyst.
- Benzene yield is higher on the 3 wt % Zn catalyst and could be seen up to the third cycle, possibly due to the following:
  - A high Zn loading (8wt%) results in a larger number of acidic sites, especially on the surface, being covered or inactive due to interaction with Zn oxide. The 3 wt% catalyst maintains more active acid sites available for oligomerization of ethylene or propylene to form benzene.
  - Zeolite pores could be blocked with excessive Zn loading.
- The main reaction that was observed during the last reaction cycle appears to be methane decomposition into carbon and hydrogen.

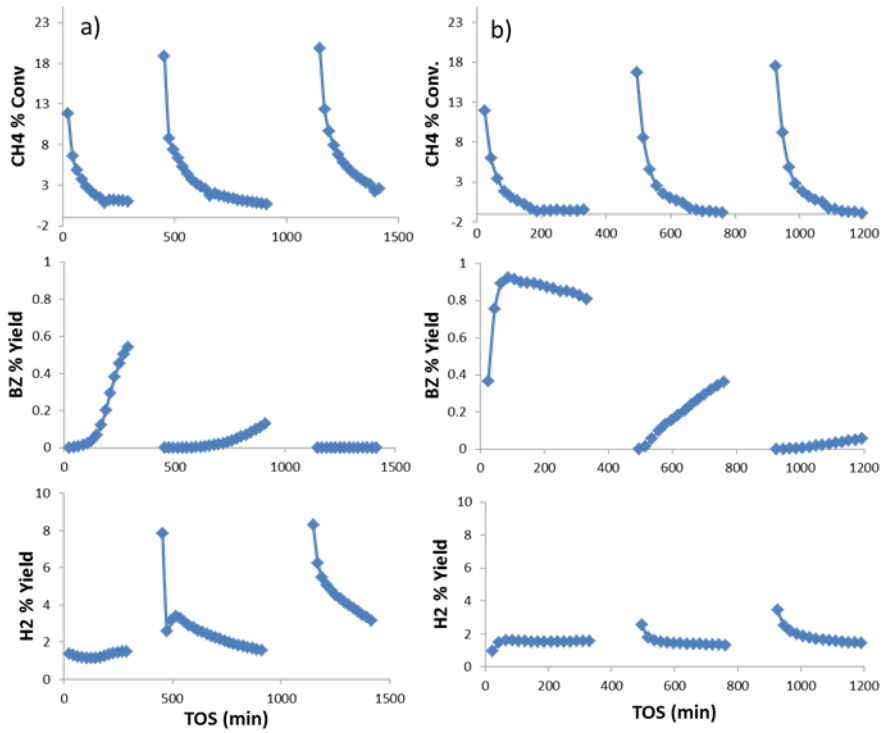

Figure 31: Comparison between the activity, benzene yield and hydrogen yield on (a) 8 and (b) 3 wt % Zn loaded on H-ZSM-5 (SAR50) under WHSV of 3000 cc/g/h

Structurally Engineered Pore-Embedded Catalysts

The DHA of small hydrocarbons—here discussed using methane as the technologically most interesting source material—is thermodynamically limited to ~15% aromatics yield at technically relevant reaction conditions (ambient pressure, ~700°C). Already at standard reaction conditions, catalyst lifetime is limited by carbon formation (coking), and when hydrogen removal is applied it is projected to strongly exacerbate this problem. This problem is further compounded for the current state-of-the-art catalyst, MoC-ZSM-5, since regeneration of the catalyst leaves Mo in the (inactive) oxide form, and therefore, requires lengthy re-activation of the catalyst. The same deactivation via oxidation of the catalyst also precludes use of standard "anti-coking" measures such as addition of mild oxidants to the feed (typically H_2O or CO_2).

The main focus of the catalyst development work was therefore on identifying and developing a catalyst that combines robustness under typical regeneration/anti-coking measures with as high resistance to coking as possible. The first requirement suggests that the catalyst should be active in its highest oxidation state in order to avoid re-activation phases after regeneration of the coked catalyst and to allow de-coking measures via co-feed of oxidants. Carbides, oxy-carbides, and low-oxidation state metals, which constitute the vast majority of catalyst systems for DHA reactions are excluded. In fact, a broad literature review identified ZnO as the only known metal oxide that shows good DHA activity in its highest (only) oxidation state.

While the first requirement can thus be met by changing the composition of the catalyst, the second requirement, coking resistance, is targeted via structural design of the catalyst. Previous reports on related reaction systems, as well as known aspects of the reaction mechanism, suggest that coking occurs at least to a significant degree via secondary reactions of the desired primary reaction products (i.e., aromatics).

Fast removal of these primary products from the catalyst pores is required to minimize undesired coking. The zeolitic pores only allow for very slow Knudsen diffusion as transport mechanism for the removal of these products, during which the products remain in close contact with the catalytic wall and are very likely to undergo further (cracking) reactions. In contrast to that, formation of mesopore as “escape pores” with diameters in the size range > 2nm will allow fast molecular diffusion to remove the products with minimal contact with the catalytic wall.

Combining these two design objectives, the target for the development of novel nanostructured catalysts was a novel catalyst which incorporates ZnO as the site for methane activation into the zeolitic framework of ZSM-5 in such a way that it maximizes activity (by using well-dispersed, highly active ZnO nanoparticles) while minimizing coking (by nanostructuring the catalyst and allow products to escape from the catalyst pore network before undergoing secondary, coke-forming reactions). A systematic “bottom-up” approach was pursued in two steps: (1) well-defined ZnO nanoparticles were synthesized and (2) were then embedded into a zeolite matrix. For all steps, simplicity of the synthetic approach and a high synthetic yield were targeted in order to assure that any develop synthetic route would have the potential for future scale-up to industrial scale production.

Zeolite Synthesis

As a first step, the synthesis of metal-free ZSM-5 materials was pursued to establish a reference material. Three hydrothermal reactors were purchased and put online in order to allow accelerated testing. Several literature recipes for zeolite synthesis were evaluated with regard to robustness, yield, and efficiency. The most promising syntheses were further investigated to identify effect of temperature and pH (as key parameters for the synthesis) on crystalinity, structure, and size of the resulting zeolite particles. By optimizing the synthesis conditions, it was possible to accelerate the synthesis from >5 days to ~1 day (greatly reducing cost for such a catalyst) and reduce the size of the zeolite crystals from ≥100 µm to ~2-5 µm (see Figure 32).

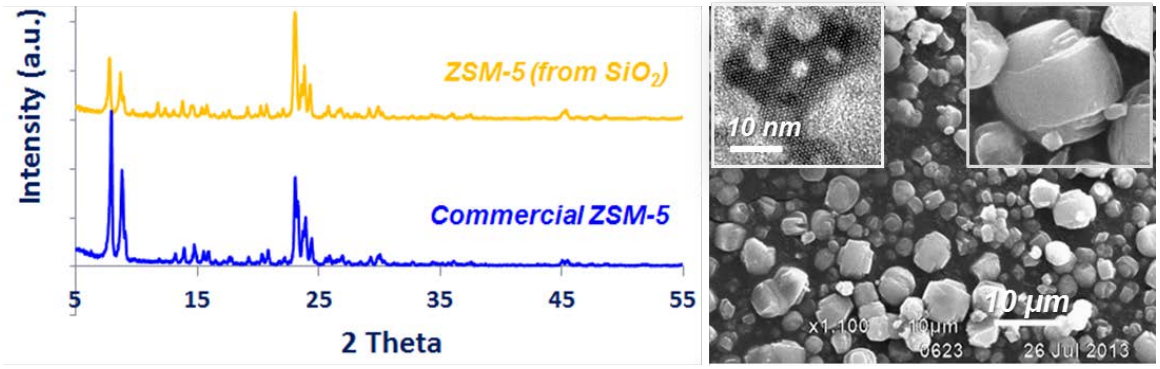

Figure 32: Left: XRD diffractograms for a ZSM-5 catalyst synthesized in this work (top) in comparison to a commercial ZSM-5 sample (bottom). Right: SEM images of the ZSM-5 catalyst (big picture and top right inset) and HRTEM image showing atomically resolved zeolite structure (top left). Overall, ZSM-5 crystals with ~2-5µm size and excellent crystallinity are obtained.

ZnO Nanoparticle Synthesis

Next, the synthesis of ZnO nanoparticles was pursued, again building on existing synthesis procedure in the open literature, evaluating several different approaches with regard to yield and simplicity. Again two

different synthesis approaches were pursued in parallel (due to the tight time constraints for the project. Typical ZnO nanoparticles resulting from this synthesis are show in

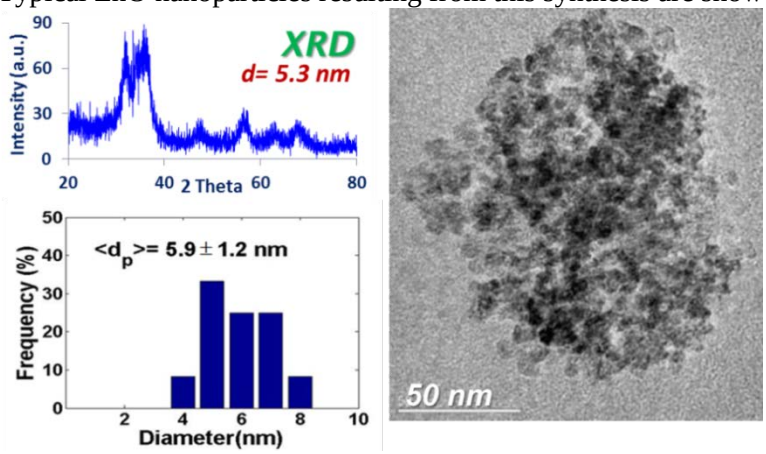

Figure 33. Through modifications of the synthesis conditions and through post-synthetic thermal treatment, it was possible to synthesize to-date ZnO nanoparticles with diameters between 3 nm and ~20 nm.

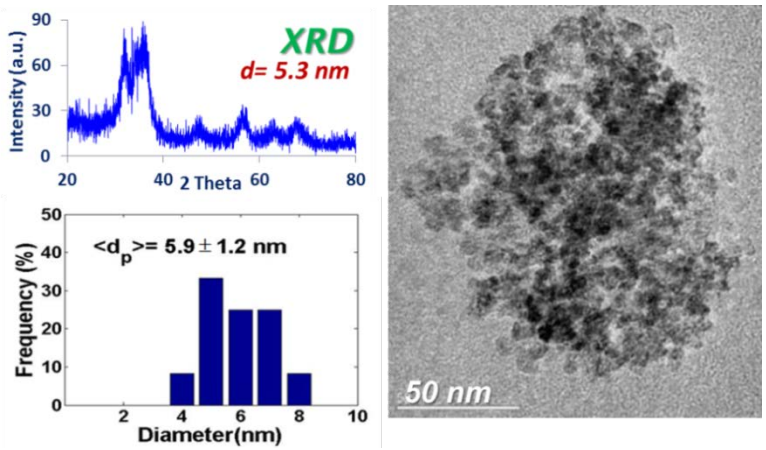

Figure 33: Right: TEM image of ZnO nanoparticles embedded in silica shells. Left: NP size distribution (from TEM) and XRD diffractogram along with particle size calculated from Debye-Scherrer. Good agreement between two particle sizes is found.

Encapsulation of ZnO Nanoparticles in Silica

A key aspect in synthesizing homogeneous core@shell materials, such as the targeted ZnO@ZSM-5 materials in this work, lies in stabilizing the nanoparticles during the synthesis. In the present work, a novel pathway to achieve this goal was pursued: Since silica is used as precursor for the formation of the zeolite matrix, and synthesis procedures for the silica-encapsulation of metal NP are well established in the literature (and routinely performed in the lab), the synthesized ZnO nanoparticles in silica shells were encapsulated in an intermediate step.

Figure 34 shows some typical transmission electron microscopy (TEM) images of these materials: One can see that a homogeneous distribution of the ZnO nanoparticles in the silica matrix can be achieved even for weight loadings as high as 20 wt%. While it is difficult to detect the crystallinity of the small nanparticles within the silica shells, high-resolution transmission electron microscopy (HRTEM) shows that the crystalline ZnO nanoparticles are not affected by the encapsulation process.

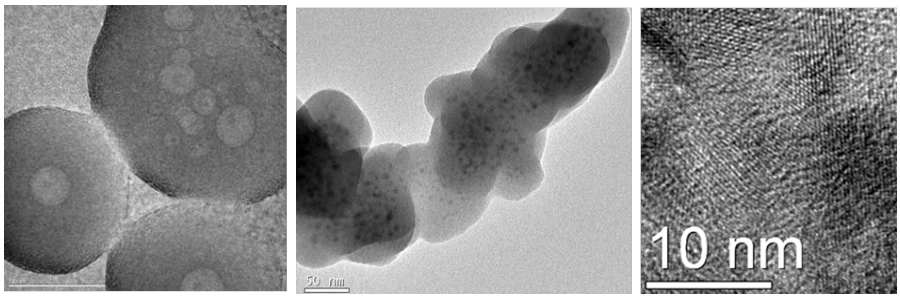

Figure 34: TEM images of ZnO@SiO_2: low weight loading (~4wt%; left) and high weight loading (~20 wt%; middle), along with HRTEM image showing lattice fringes of ZnO embedded in the silica matrix (right).

Conversion of ZnO@SiO_2 to ZnO@ZSM

In the final step of the synthesis, the ZnO@SiO_2 materials were then converted to ZnO@ZSM-5, following the same pathway that was developed for the NP-free ZSM-5 synthesis. Figure 35 (top row) shows a typical material resulting from this synthesis: SEM reveals that the ZnO@ZSM-5 particles show a striking morphology, consisting of stacked nanorods, i.e., strikingly dissimilar to typical pure ZSM-5 crystals (as shown previously, in Figure 32).

This break-up of the zeolite particles into nanorods appears to be caused by the intercalation of the ZnO nanoparticles, as further supported by another observation shown in the bottom row in Figure 35. With increasing NP weight loading of the materials, the size (width) of the nanorods decreases strongly, suggesting that the intercalation of the nanoparticle does indeed cause the break-up of the zeolite crystals into nanorods (and the increasing NP number with increasing weight loading will hence result in the formation of more nanoparticle boundaries).

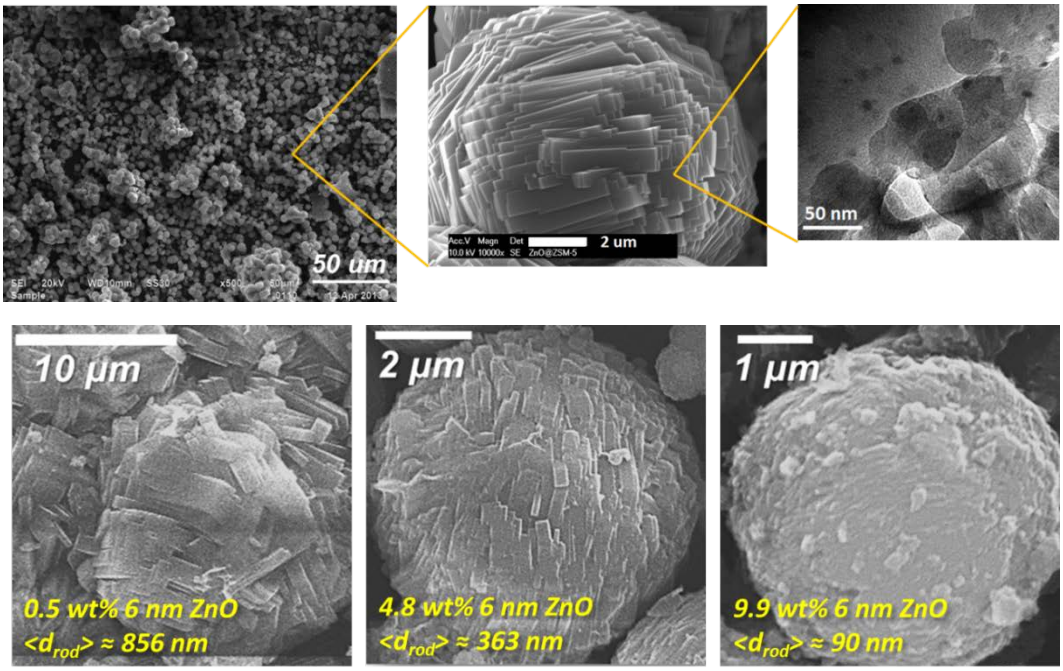

Figure 35: Top: SEM (top left and middle) and TEM (top right) images of ZnO@ZSM-5: The synthesis results in long-range homogeneous materials (top left), where the individual particles (in the size range of ~5 µm) are composed of stacked zeolite nanorods (top middle) into which the ZnO nanoparticles are homogeneously dispersed (top right).

Bottom: SEM images of ZnO@ZSM-5 with increasing weight loading from left to right. One can see that the width of the constituent nanorods decreases strongly with increasing weight loading (average rod width is indicated in the SEM image).

Despite the change in morphology, however, neither the overall crystallinity of the zeolite (Figure 36, top left) nor the micropores (Figure 36, top right) are significantly affected. However, more significantly, the embedding of the ZnO nanoparticles does result in the intended formation of mesopores: As shown in Figure 36, bottom left, the increasing slope and hysteresis of the nitrogen sorption curves with increasing ZnO weight loading indicates the increasing formation of mesoporosity in these samples. The direct correlation between embedding of ZnO nanoparticles and the formation of mesoporosity is further shown in Figure 36, bottom right: Clearly, the specific volume and surface area of the samples in the mesopore range (2-50nm) increases systematically with ZnO weight loading.

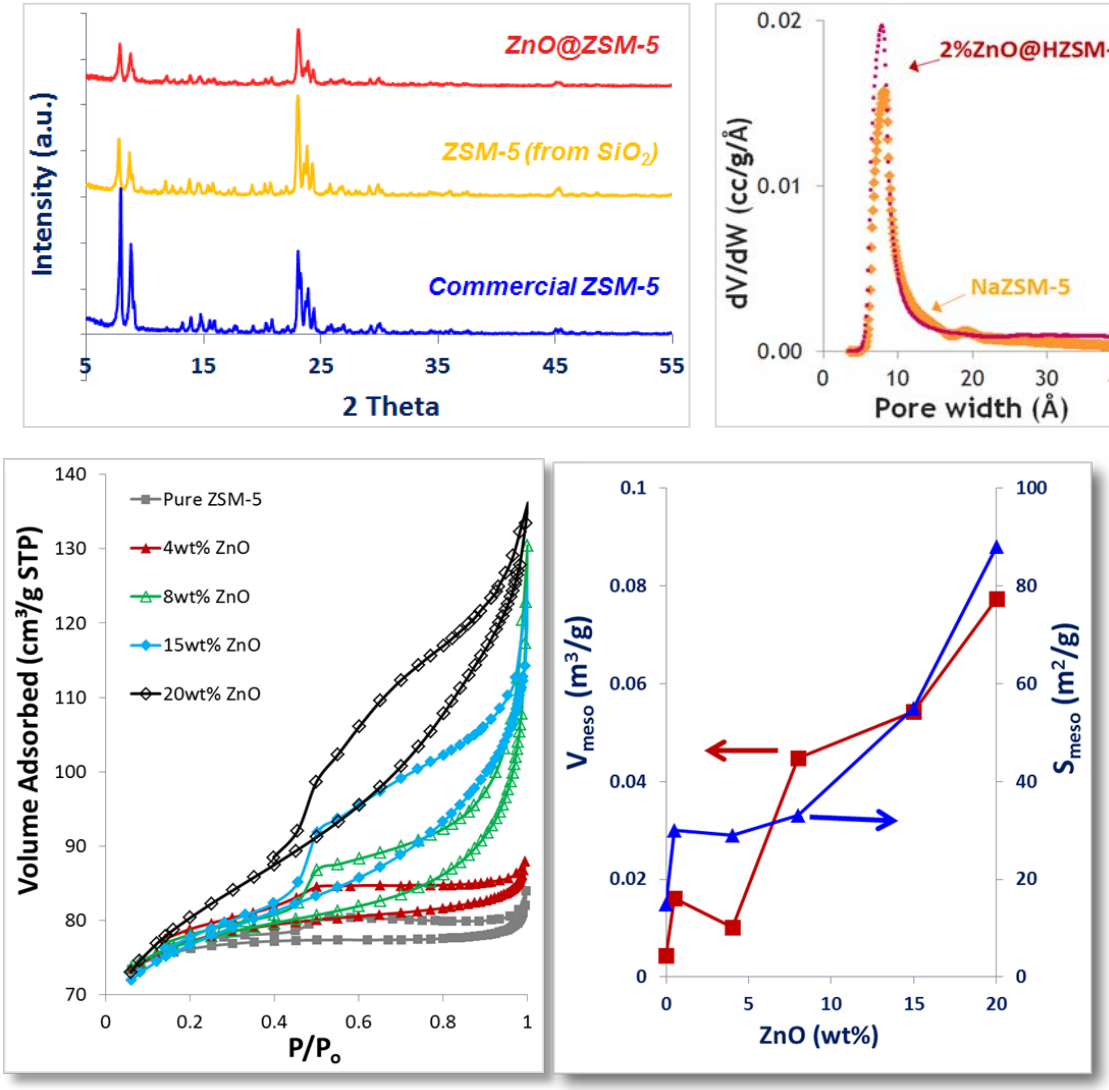

Figure 36: Top left: XRD diffractograms of a commercial ZSM-5 (bottom), a pure ZSM-5 sample synthesized in this work (middle), and of a ZnO@ZSM-5 sample (top). Top right: Size distribution in the micropore range for a pure ZSM-5 and a ZnO@ZSM-5 material with 2wt% ZnO.

Bottom left: Nitrogen sorption curves for ZnO@ZSM-5 with increasing ZnO NP weight loading from 0-20wt%, and corresponding specific mesopore volumes and surface areas (bottom right).

Interestingly, the mesoporosity can not only be tailored via the weight loading of the sample, but also via changes in nanoparticle size: Figure 37 shows the mesopore size distribution for three samples with 3, 6, and 15 nm ZnO nanoparticles embedded in ZSM-5. One can clearly see how the pore size distribution broadens towards larger pore sizes with increasing particle diameter. Overall, the newly developed synthesis path not only allows us to create ZnO@ZSM-5 nanostructured catalysts with a homogeneous distribution of embedded ZnO nanoparticles, but also allows fine control over mesoporosity by controlling the amount and size of nanoparticles embedded into the structure.

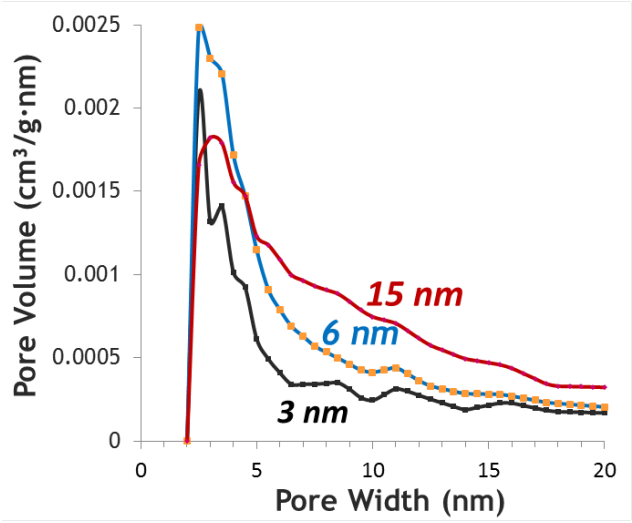

Figure 37: Pore size distribution in the mesopore size range (2-20 nm) for ZnO@ZSM-5 with ZnO NP with 3, 6, and 15 nm diameter. A direct correlation between NP size and PSD is apparent.

Reactivity Evaluation

With the successful establishment of synthetic control over the nanocatalyst composition and morphology, the project transitioned to reactive evaluation of these nanostructured catalysts in order to verify the impact of nanostructure on the coking resistence of the catalysts and establish clear structure-activity/stability correlations.

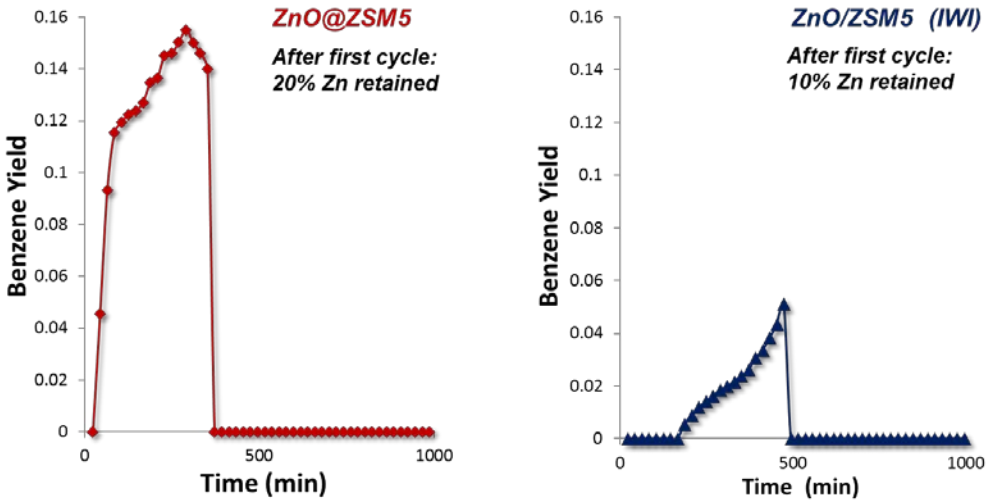

Figure 38 shows a first comparative reactive evaluation of a nanostructured ZnO@ZSM-5 catalyst and a conventional ZSM-5 catalyst (prepared via IWI of a commercial ZSM-5 sample). The catalysts were evaluated in multiple DHA cycles, comprised of methane conversion followed by regeneration in air. The data shown constitutes the measured benzene yields during the first methane cycle. Clearly, this data suggests that the nanostructured catalyst is superior in performance to the conventional catalyst, albeit a more detailed investigation is required to confirm this trend.

Interestingly, while both samples showed excessive Zn loss over the first cycle and strong of the catalysts, the tight embedding of the ZnO into the nanostructured catalyst and the extraneous ZnO on the external zeolite surface result in a significantly improved stability of the

nanostructured catalyst: The conventional catalyst retained only 10% of the original Zn content, while the nanostructured catalyst retained twice that amount. The reason for the Zn loss can be found in the reduction of ZnO to metallic Zn in the reducing atmosphere of DHA: While ZnO is high-temperature stable, Zn has very poor thermal stability (T_m= 420°C, T_b= 907°C). This is confirmed in non-reactive tests in a mode reducing (5%H_2 in N_2) and oxidizing atmosphere (air), shown in

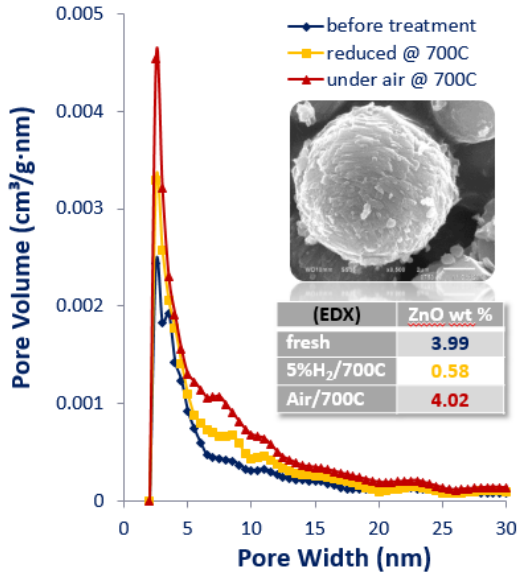

Figure 39. While in both cases the nanostructured catalyst is structurally stable (as apparent from the unchanged mesopore size distribution and the unchanged morphology in SEM), the catalyst lost almost 90% of the Zn in the reducing atmosphere, while the Zn content is unchanged under oxidizing conditions.

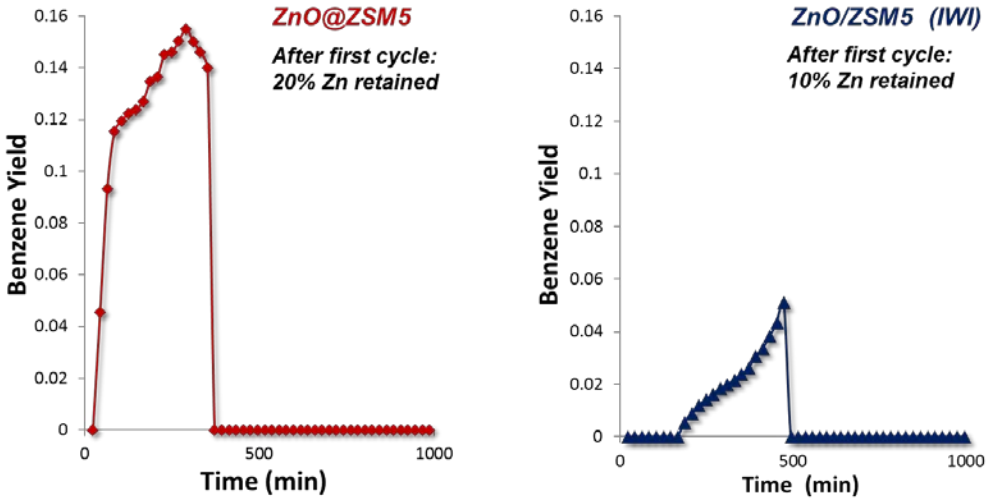

Figure 38: First reactive evaluation of a ZnO@ZSM-5 catalysts in direct comparison to a conventionally prepared ZnO/ZSM-5 (both with 8wt% ZnO, Si:Al = 50, T=700°C). Benzene yield vs. time shows a significantly enhanced reactivity for the nanostructured catalyst.

This result suggests that the catalyst could be rendered stable through multiple control measures. First, doping of oxide materials with an oxygen donor, such as ceria, has been shown previously to result in a strong stabilization of the oxide. Indeed, the first tests with conventionally prepared ceria-doped ZnO/ZSM-5 samples suggest that this results in a strong stabilization of the catalyst. Second, co-feeding

of mild oxidants, which is a measure that was initially already proposed to reduce coking of the catalyst, should result in a stabilization of the oxide phase and hence reap dual benefits for the reaction system. Finally, on a process level, terminating the DHA production phase before strong reduction of the oxide phase occurs could be a last stop-gap measure to control Zn loss.

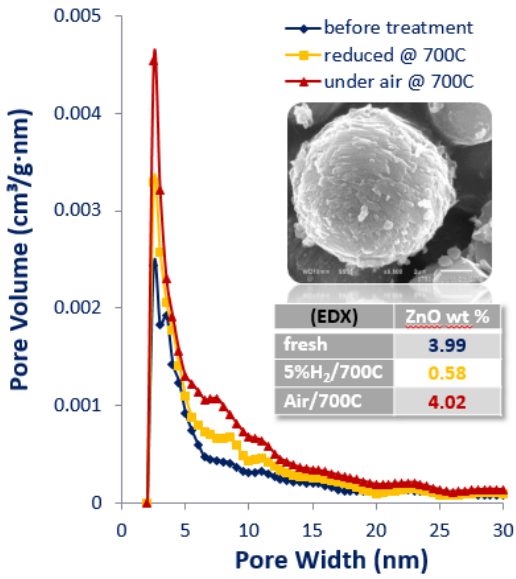

Figure 39: Stability tests for ZnO@ZSM-5: Pore size distribution before and after high-temperature exposure (1h, 700°C) to a reducing and oxidizing atmosphere, respectively. The insets show a TEM image of the sample after exposure to the reducing atmosphere, and the ZnO weight loading (determined via EDX) before and after the two treatments.

Summary

Over the course of the first project year, a novel synthesis pathway was developed that allows creation of the desired catalyst target structure for DHA in an efficient multi-step synthesis procedure: It combined the embedding of highly active, size-controlled ZnO nanoparticles into a zeolite structure with the simultaneous formation of mesopores as escape pores for desired primary reaction products in order to suppress coke formation (which is detrimental to reaction yields and limits the lifetime of the catalyst). A thorough understanding for the synthesis mechanism was established, which will allow extension of the synthesis onto other systems of interest (including Fe, Cu, and Ni as base metals for the catalysts) in FY14. First reactive evaluations support the basic premise of this work that such appropriately nanostructured catalysts can indeed result in significant performance improvements in DHA and act as critical enablers for advanced reactor concepts (such as membrane reactors) which will allow to break thermodynamic equilibrium limitations and hence remove the key hurdle towards industrial realization of DHA processes.

Membrane Reactor Studies

The main goal of this project is to convert methane to aromatic compounds, BTX, using the methane DHA reaction shown below.

$$6CH_4 \leftrightarrow C_6H_6 + 9H_2$$

This reaction is equilibrium limited to ~12% conversion at 700°C over a zeolite supported Mo catalyst in a conventional reactor. In order to achieve higher conversions a hydrogen membrane reactor can be employed to remove some of the product to shift the reaction. Figure 40 is a schematic of this process.

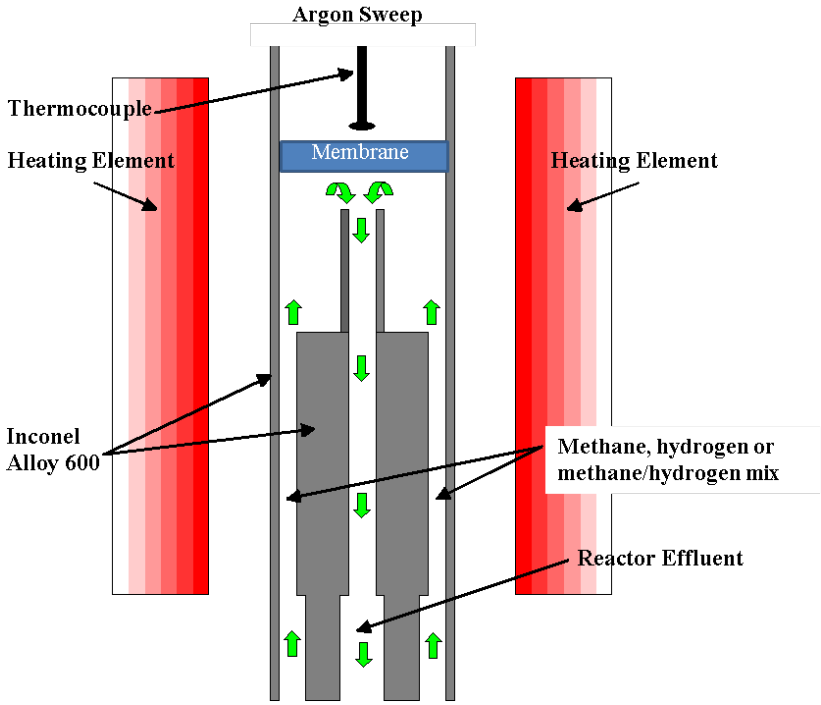

Figure 40: Schematic of methane conversion testing using a membrane (disc) reactor.

The first objective was to set up and prepare the membrane reactor. Testing of the membrane reactor began using a pure palladium (100 µm) membrane disk (0.75 in diameter). The goal of this testing was to demonstrate the viability of using a membrane reactor to improve the conversion of methane to BTX. Testing was conducted at room temperature and 750°C and atmospheric pressure with pure hydrogen, pure methane, and 50/50 (H_2/CH_4) feeds. Testing was also conducted with pure methane at a low feed rate in order to increase the residence time. At this longer residence time it appeared that there is a measurable amount of a higher hydrocarbon produced. No measurable flux of hydrogen was measured during this testing. When the membrane was removed there was a significant amount of carbon on the membrane, tubing, and thermocouple. The carbon was visually noted when the membrane was removed, however it was not possible to measure the amount of carbon produced.

Figure 41 shows the GC results for the conditions listed in Table 5. Four conditions are shown – one w/o catalyst and 3 with a loading of 0.25 g of 3%Mo/H-ZSM-5, with a SAR of 50. The time axis starts at 4 minutes due to the fact that the methane peak appears at about 2 minutes and dominates all other peaks. No hydrogen permeance was detected for the first three conditions; however, for the last condition (5atm) a slight amount of hydrogen was detected on the sweep side. The amount of hydrogen was below the calibration of the online GC.

Table 5: Summary of Methane Conversion Test Conditions

T (°C)	Pressure (atm)	Flow rate (sccm)	WHSV (scc/g/h)
750	1	50	*No Catalyst*

750	1	210	50400
750	1	50	12000
750	5	50	12000

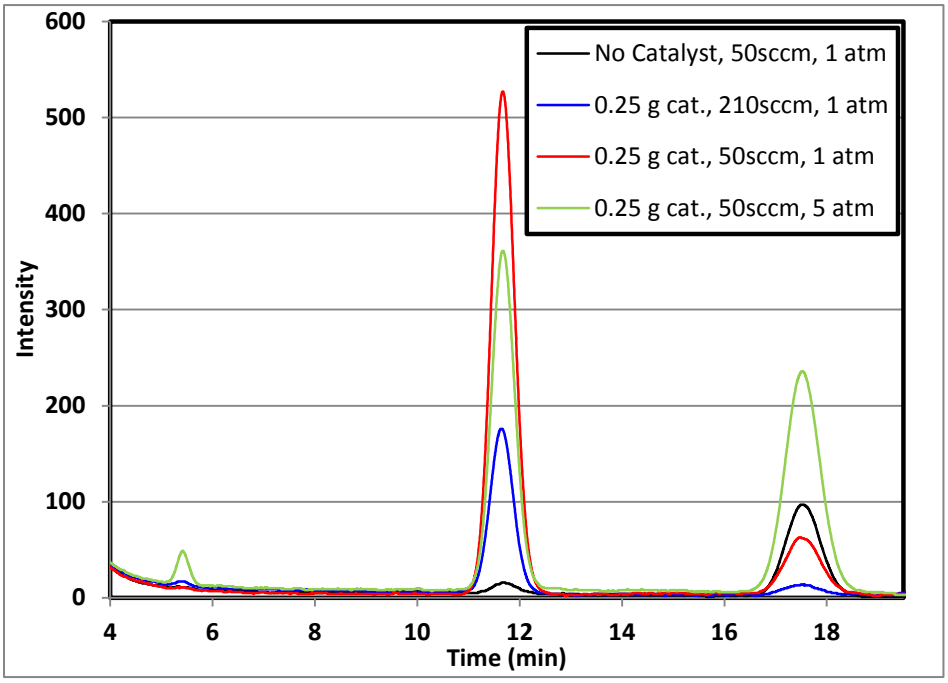

Figure 41: GC results for initial MDHA tests.

As shown in Figure 41, product peaks were noted at 5.4, 11.8, and 17.5 minutes. The relative amounts of all detected products increased when the catalyst was employed. With catalyst present when the WHSV was decreased the 17.5 minute peak increased in size. The 5.4 minute peak seems to follow the same trend. However, for the 11.8 minute peak, the 12000 scc/g/h WHSV test produced the largest peak. These two later peaks were determined to be benzene and toluene.

It was determined that the Pd disk did not provide enough hydrogen separation to achieve a significant increase in methane conversion. A 125µm thick, ¼" OD palladium tube was selected for use instead since it has over 30 times more surface area than the disk membrane. However, it was also determined that the tube needed support for higher pressure tests. The membrane tube was 6" in length, 125 µm thick palladium tube with a diameter of 0.25." A porous quartz support on the outside of the tube was used to provide some structural support. The schematic of this membrane assembly is shown in Figure 42. The argon sweep gas flow was counter-current to the feed methane flow. The argon sweep gas flow was through the annulus while the feed flow was through the inside of the membrane.

The new membrane reactor assembly was loaded with 1.2 grams of catalyst (3% Mo/HZSM-5, SAR and was installed in high-pressure tubular reactor (HPTR) 2. The testing plan matched the WHSV in the non-membrane tests conducted by other members of the group, and tests were conducted at and 10atm. The membrane failed when the pressure was increased above 10atm.

Table 6 summarizes the conditions tested and the GC results. The most promising result was the increased hydrogen in the sweep stream at higher pressures. This indicates that the membrane was functioning in

the presence of methane and the reaction products. However, all these tests were conducted prior to re-calibration of the GCs so only qualitative data could be collected.

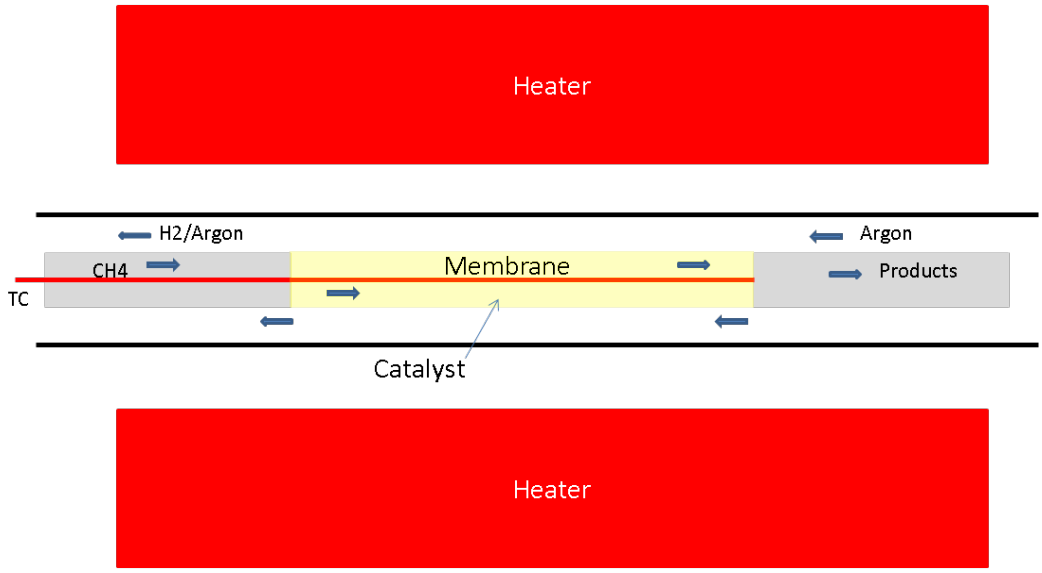

Figure 42: Schematic of 125µm thick, ¼" OD palladium membrane.

Table 6: Membrane Testing Results

T (^oC)		650	710	710	710	710	710
P (atm)		1	1	1	2	5	10
Feed		CH4	H_2	CH_4/N_2	CH_4/N_2	CH_4/N_2	CH_4/N_2
Flow (sccm)		123	267	55.8	55.8	55.8	95.2
Feed	$\%CH_4$	100%		78.5%	78.5%	78.5%	87.4%
	$\%N_2$			21.5%	21.5%	21.5%	12.6%
Sweep	$\%H_2$	0.33%	20.80%	0.33%	0.40%	0.60%	1.87%
GC Results (Peak Area)	H_2			28218	28987	25646	17372
	N_2			6887	7662	7653	4651
	CH_4	117342		88195	96307	96948	105883
	Ethylene	630		1319	1241	590	951
	Ethane	1211		1427	1772	2187	3050
	Benzene	807		5028	5485	5939	6235
	Toluene	0		303	423	550	913

Figure 43 displays the methane conversion of 4wt% Mo catalyst supported on HZSM-5 under equilibrium (non-membrane) conditions at 700°C and at different pressures (2, 15, 30, 60, and 120 psig). Each pressure data was collected for one hour before increasing the pressure. At atmospheric pressure the methane conversion was high due to carburization of Mo oxide to a mixture of Mo carbide and oxycarbide. Quickly the methane dehydroaromatization (MDHA) reaction reached the expected equilibrium limit at about 12% conversion, while the benzene concentration started to increase after a short induction period to a maximum, and then slightly decreased (Figure 44). As the reaction pressure increased to 15 psig the methane conversion decreased to about 10%. At 120 psig the conversion was fairly stable between 8 to 9%. The yield of benzene shows an enhanced effect with reaction pressure up to 30 psig. At higher pressure the benzene yield drastically decreased. The benzene yield at 60 and 120 is only slightly different. This could be explained by the residence time of methane in the reaction zone. As the pressure was increased the residence time increased, and the benzene yield increased up to 30 psig. By increasing the residence time further coking can dominate and there is no chance for benzene to diffuse from the zeolite pores quickly enough before forming coke.

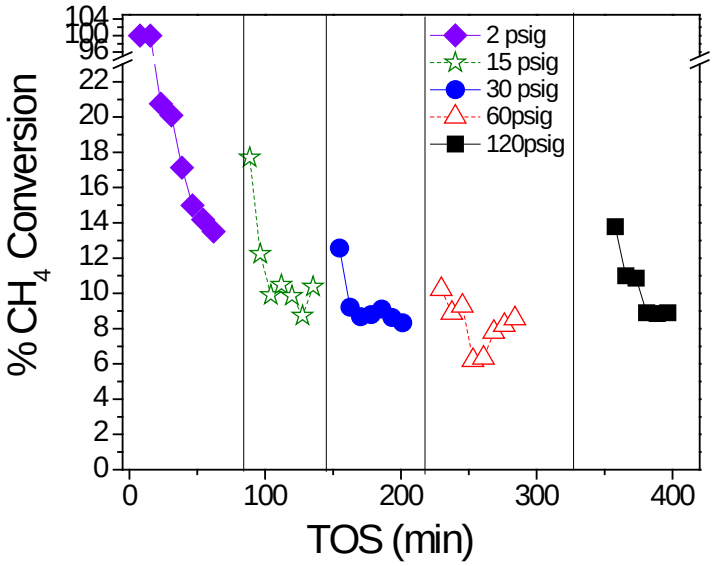

Figure 43: Methane conversion over Mo/HZSM-5 catalyst (700°C, 3000 scc/g/hr) under different pressures with no Pd membrane.

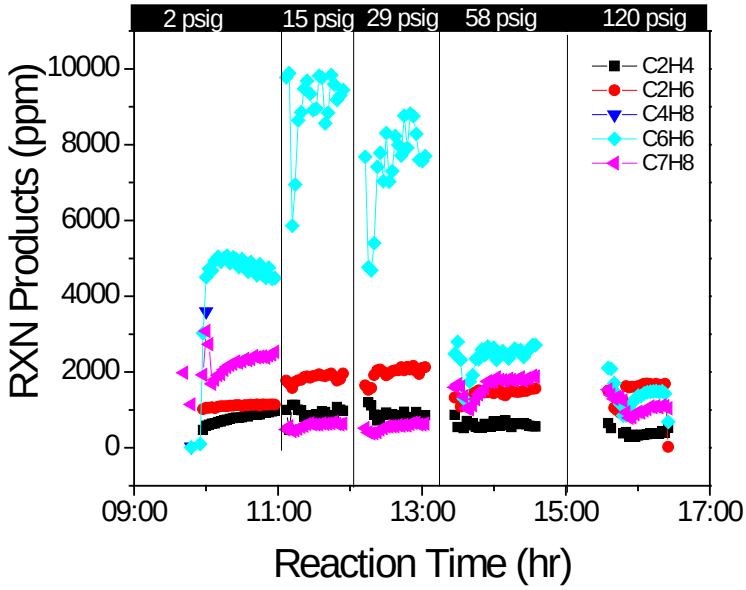

Figure 44: Products as a function of reaction pressure over Mo/HZSM-5 catalyst (700°C, 3000 scc/g/hr) with no Pd membrane.

The methane DHA reaction was tested on 3wt% Zn supported on HZSM-5. The initial reaction temperature was set at 625°C then increased to 650°C, and finally kept at 700°C until the end of the experiment. The reaction pressure was changed from 2 to 15, 60, 120 psig and then back to 2 psig. The methane conversion at 2 psig was about 6%, and slightly increased to 6.9 % at 60 psig (Figure 45). Similar to Mo catalyst, the Zn catalyst does not change much with pressure; however, as expected, the Zn catalyst has lower selectivity and slightly less conversion under equilibrium reaction conditions. In other words, most of the Zn catalyst activity is due to decomposition of methane into coke. It was observed that

the conversion and selectivity is restored once the reaction is depressurized. The benzene selectivity dropped from 9 to 3% as the pressure increased from 2 to 120 psig. An increase in benzene selectivity was observed once the reaction was depressurized to 5%. The residence time of the methane had almost no effect on Zn catalyst compared to Mo catalyst possibly due to the location of the catalyst with respect to the support. In Zn catalyst it is believed to be mostly on the surface of the zeolite with a small amount, or none, inside the zeolite pores. Therefore, C-C coupling reaction sites are mainly on the outer surface of the catalyst particles while the majority of the Bronsted acid sites are inside the zeolite pores where aromatization occurs. Mo can migrate inside pores so the C-C active sites and Bronsted acid sites are in close proximity to facilitate higher selectivity of aromatic compounds.

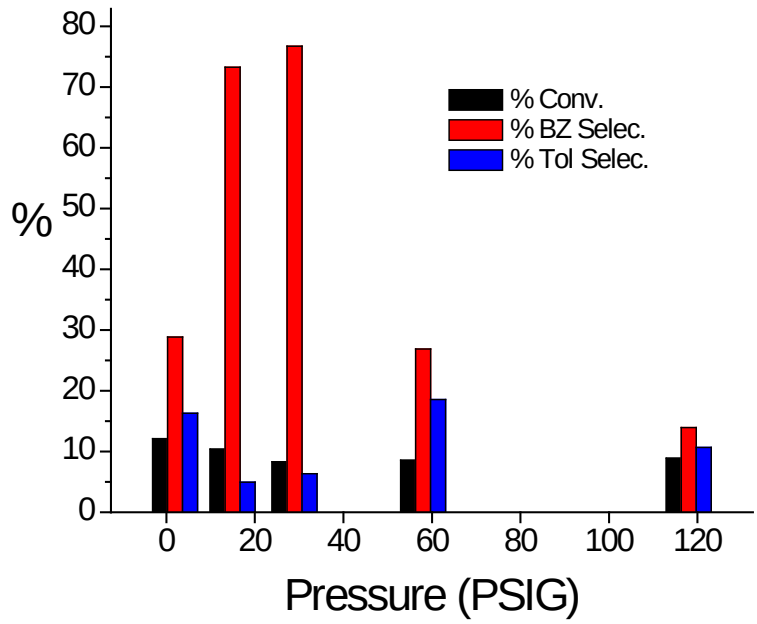

Figure 45: Selectivity of aromatic products and methane conversion as a function of pressure over Mo/HZSM-5 catalyst (700°C, 3000 scc/g/hr) with no Pd membrane.

The procedure utilized to study the 3wt% ZnO/ZSM-5 catalyst under equilibrium conditions (i.e., Pd tube membrane) was repeated for the non-equilibrium conditions (with membrane). The results non-membrane tests are presented in Figure 46, Figure 47, and Figure 48. These results were compared to testing with a Pd membrane, which are shown in Figure 49 and Figure 50, and the conversion and selectivity at the last data point at each condition are summarized in Table 7

Table 7The reaction conditions were set at 700°C and the initial pressure was 2 psig, and a space velocity of 3000 scc/g/h. Consistent with the non-membrane test, methane conversion was stable at ~6-7% (Figure 48). This indicates the effect of the membrane on conversion is insignificant at low pressure. However, as can be seen in Figure 49, there is a steady increase in benzene and toluene production over time at this pressure. This suggests a possible activation period for the Zn catalyst.

At the second pressure setting of 15 psig there is a slight decrease in conversion over time to about 5.5%, but with relatively stable benzene and toluene production. At the final pressure of 60 psig there is a noticeable increase in methane conversion from 5.5 to almost 8% before decreasing back down to 5.5%. During this period, there is a slight decrease in benzene production; however, the toluene level remains steady. This data indicates that at higher pressure, and consequently a higher level of hydrogen removal, conversion of methane improves. Due to a steady decline in conversion over time, presumably due to

catalyst deactivation, the full extent of the effect of pressure in the presence of the membrane is not obvious. Further, as mentioned in the previous section, the effect of higher residence time still needs further examination. As a final note, this test was not run at the final pressure setting used in the previous tests (120 psig) due to a leak that developed within moments of reaching this pressure. As a result the highest pressure setting for all future membrane tests will be 90psig.

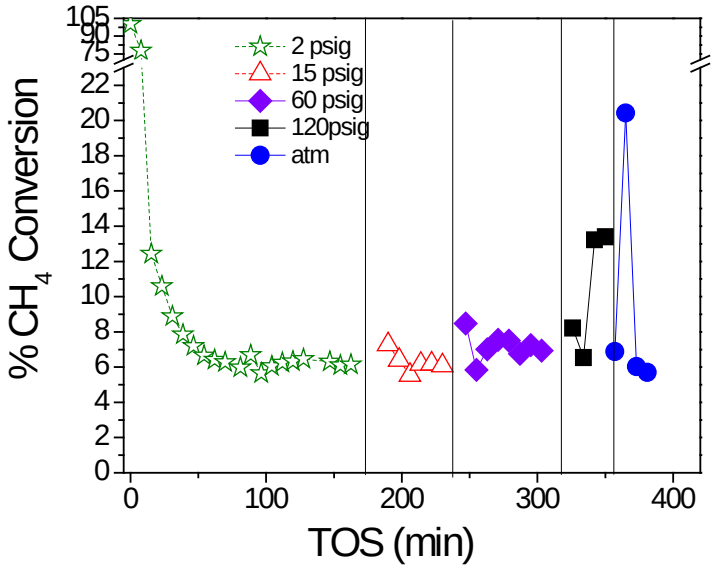

Figure 46: Methane conversion over Zn/HZSM-5 catalyst (700°C, 3000 scc/g/hr) at different pressures with no Pd membrane.

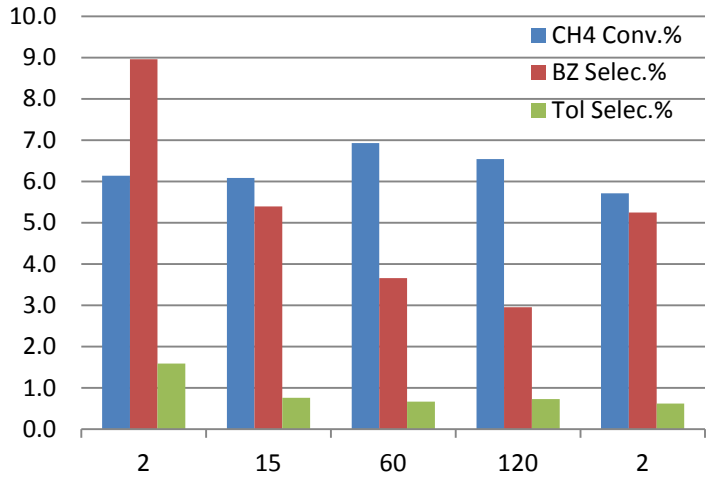

Figure 47: Selectivity of aromatic products and methane conversion as a function of pressure over Zn/HZSM-5 catalyst (700°C, 3000 scc/g/hr) with no Pd membrane.

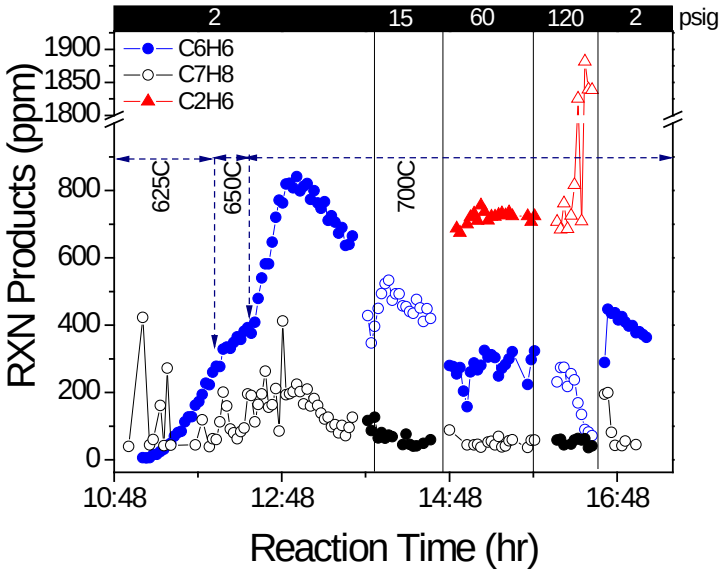

Figure 48: Products as a function of pressure over Zn/HZSM-5 catalyst (700°C, 3000 scc/g/hr) with no Pd membrane.

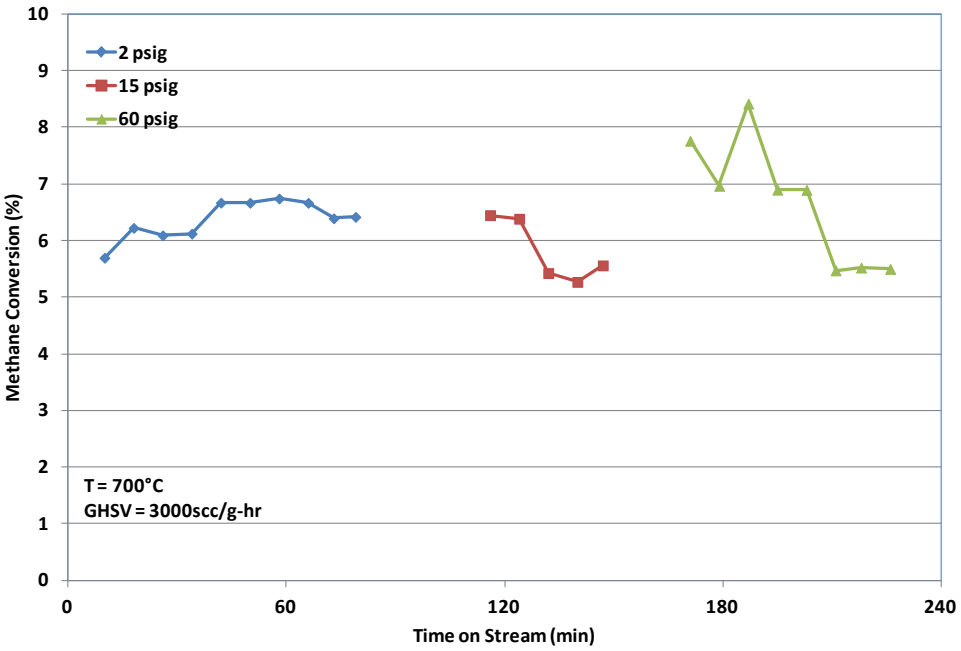

Figure 49: Methane conversion over 3wt%Zn/HZSM-5 catalyst (700°C, 3000 scc/g/hr) at different pressures with Pd tube membrane.

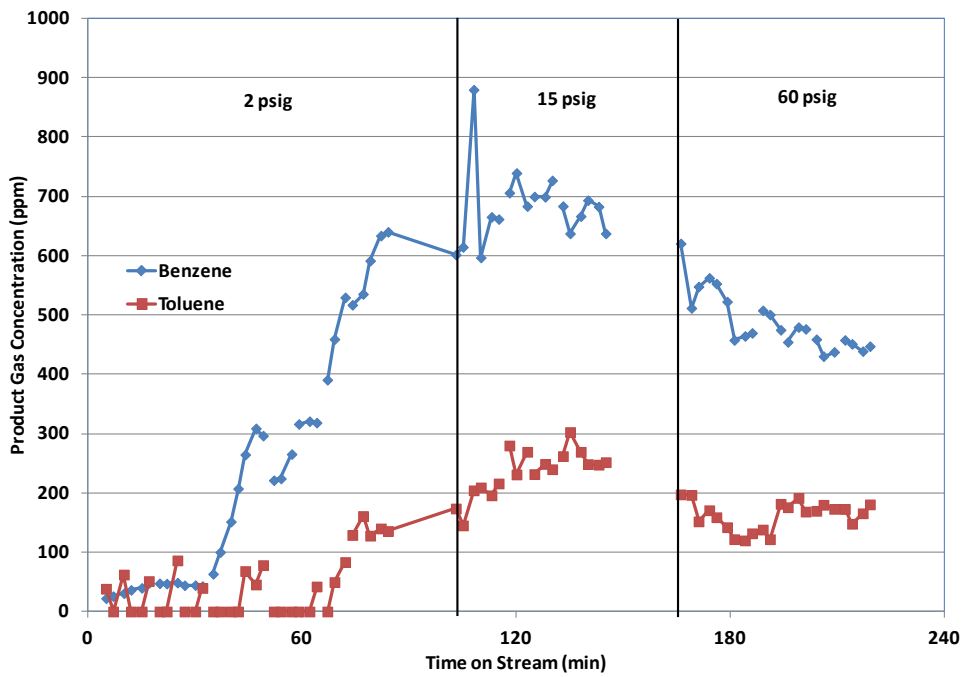

Figure 50: Products as a function of pressure and time over 3wt%Zn/HZSM-5 catalyst (700°C, 3000 scc/g/hr) with Pd tube membrane.

Table 7: Conversions and Selectivities of 3wt% Zn/H-ZSM-5 at Different Pressures with Pd Tube Membrane

P (psig)	Methane Conversion (%)	Benzene+Toluene Selectivity (%)
2	6.4	1.8
15	5.6	2.7
60	5.5	1.8

Constant pressure MDHA experiments were conducted on 4wt%Mo/HZSM-5 at a constant temperature of 700°C, 5 atm, and a space velocity of 3000 scc/g_{cat}/h. In Figure 51, the effect of the membrane on methane conversion and benzene selectivity are presented. At 5 atm the increase in methane conversion in the presence of the membrane was very small (~1-2%), while the initial benzene selectivity was lower and decreased more rapidly. Figure 52 shows that the additional methane conversion resulted in higher yields of light hydrocarbons, trending consistently up as the benzene selectivity decreased. A possible explanation for this is more rapid plugging of the pores, where ring formation occurs, from carbon deposits. Additional coke formation was expected with removal of hydrogen from the product stream. Therefore, the expected effect of the membrane, though limited, was observed experimentally. These results are also consistent with reported literature results, which experienced minimal increases in conversion. It was reported by Iglesia, et al., that they removed < 20% of the hydrogen produced and it was concluded that was not sufficient to shift the equilibrium enough to achieve significantly higher conversion. In Figure 53 it is shown that in the experiments <30% of the hydrogen produced was removed and measured in the sweep gas. This demonstrates that a significant amount of the hydrogen produced needs to be removed to break the equilibrium conversion. It is expected that future runs at higher pressure (>10 atm) will result in a more pronounced increase in methane conversion.

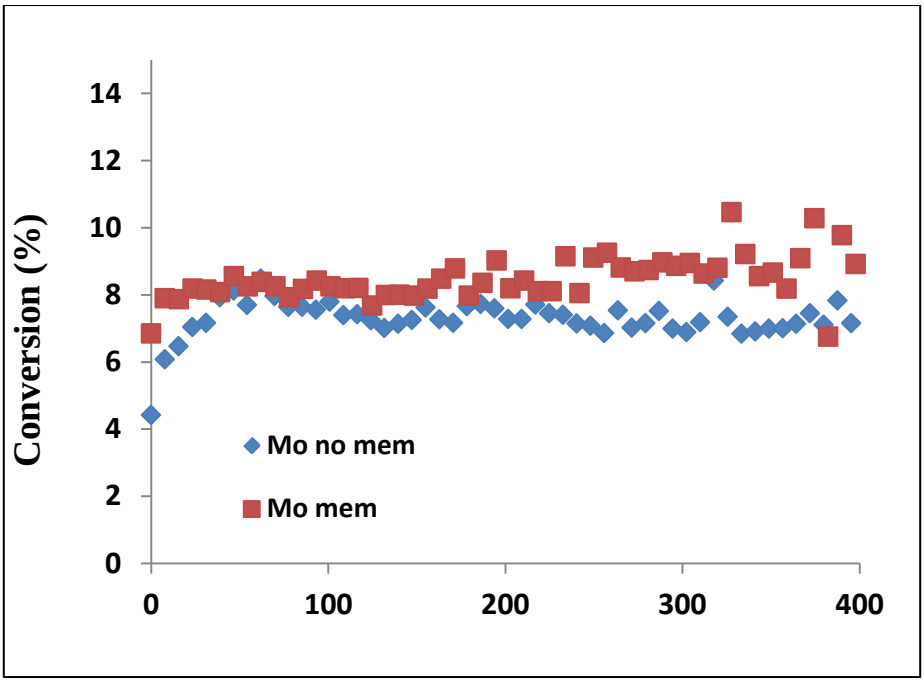

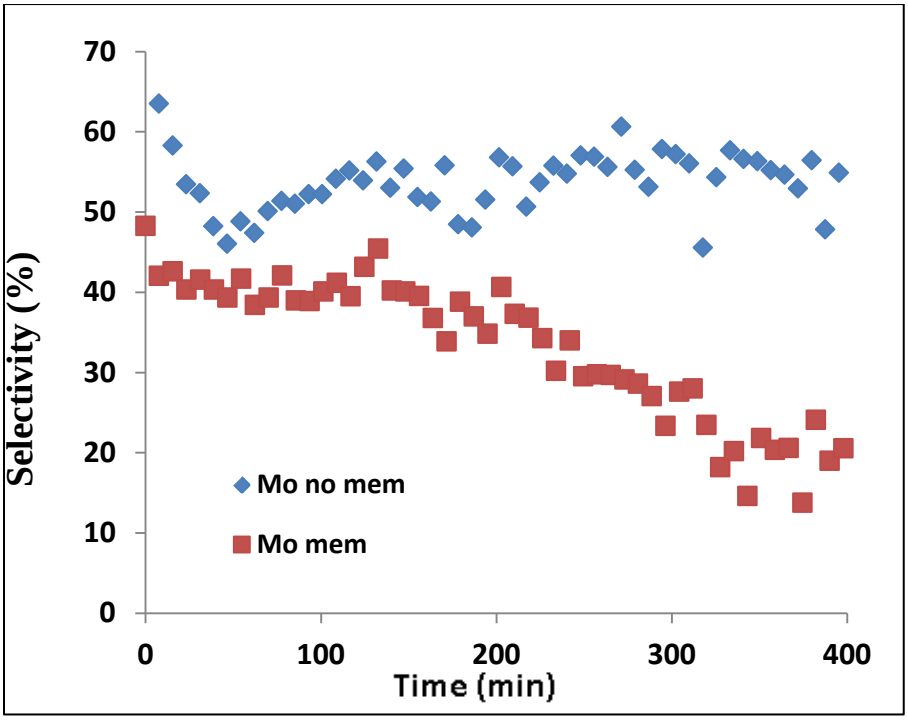

Figure 51: Performance of 4wt% Mo/HZSM-5 catalyst under methane DHA (700°C, 5 atm, 3000 scc/g/hr) with and without Pd membrane: (a) Methane conversion, (b) Benzene (BZ) selectivity.

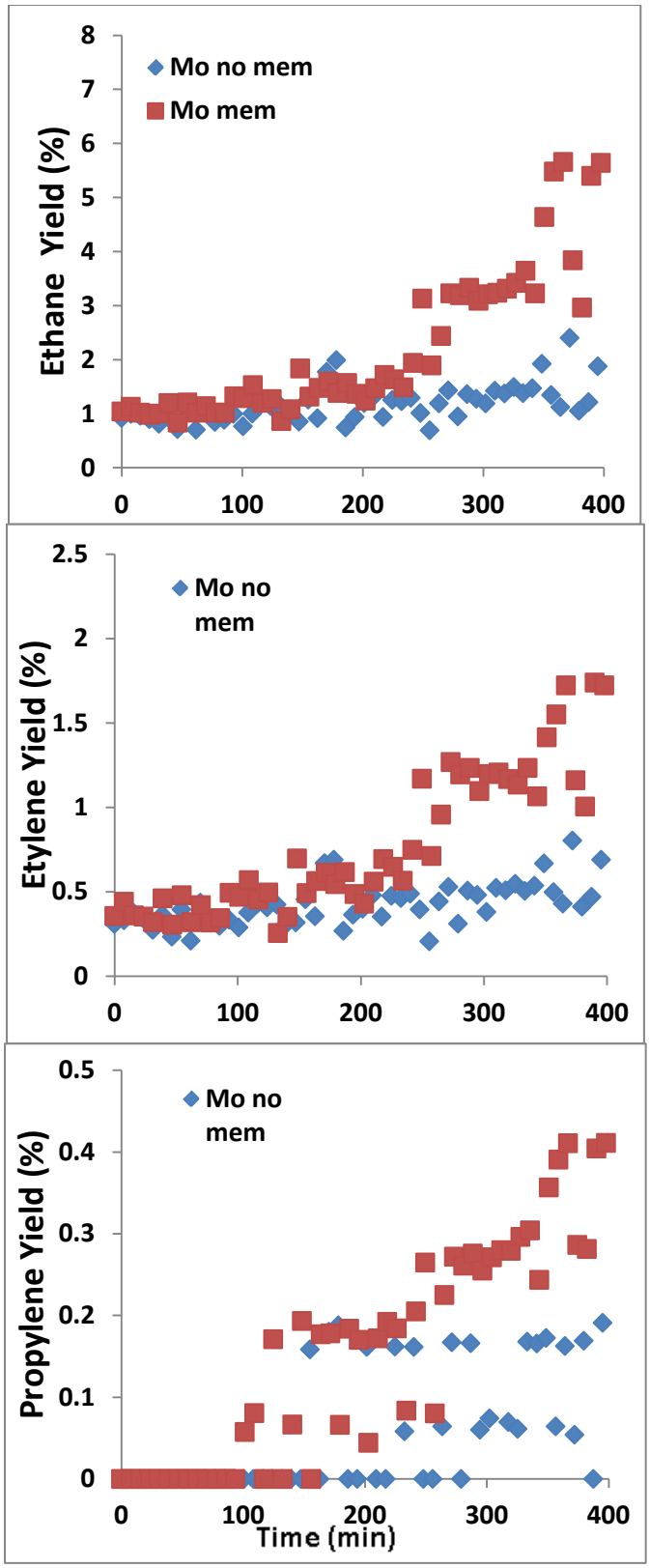

Figure 52: Light hydrocarbon yields with 4wt% Mo/HZSM-5 under methane DHA (700°C, 5 atm, 3000 scc/g/hr) with and without Pd membrane: a) Ethane, b) Ethylene, c) Propylene.

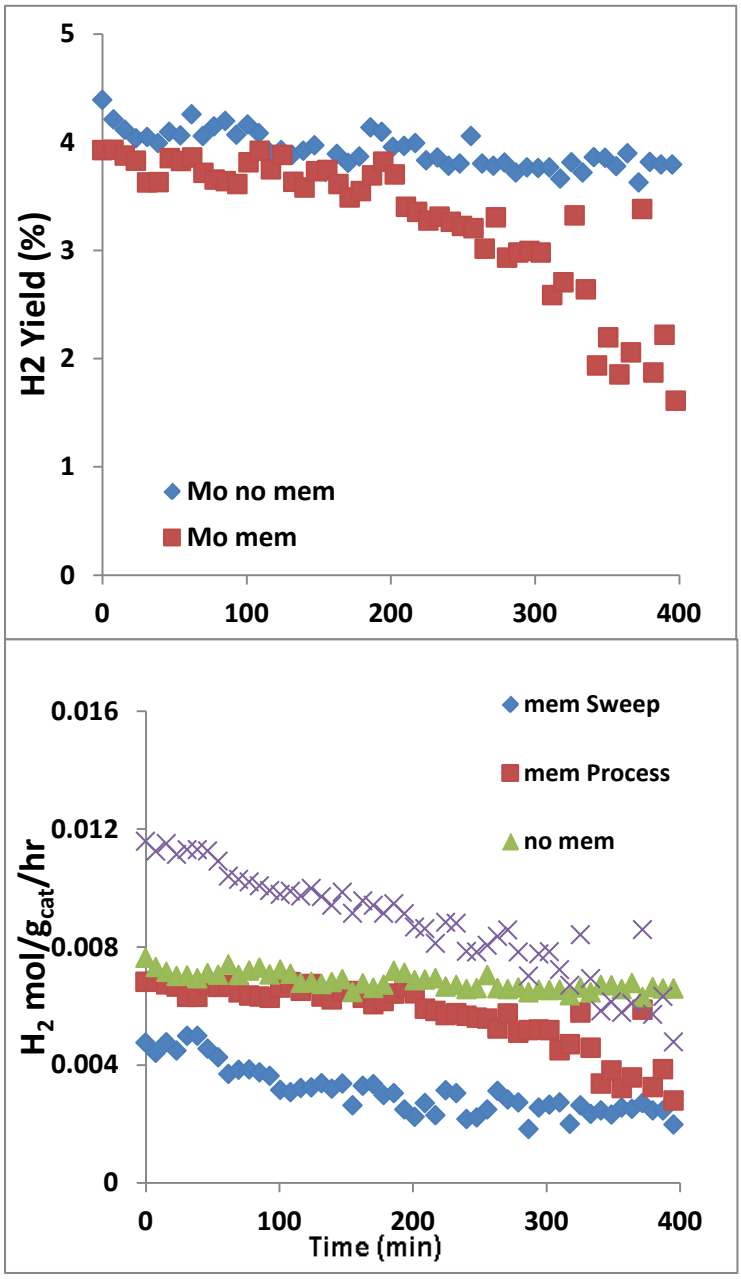

Figure 53: Hydrogen production with 4wt% Mo/HZSM-5 under methane DHA (700°C, 5 atm, 3000 scc/g/hr) with and without Pd membrane.

Figure 54 and Figure 55 present the results of the experiments conducted in the HPTR for Zn/HZSM-5 catalyst with and without the membrane tube reactor. The trends are the same as for the previously presented Mo catalyst. There was only a slight increase in methane conversion (again ~1-2%) with the membrane, compared with the non-membrane reactor. However, the Zn catalyst had lower overall benzene selectivity than Mo. Also, consistent with the Mo results, an increase in light hydrocarbons trended well with the decrease in benzene. It is interesting that the Zn catalyst had a more significant drop in benzene corresponding to a more significant increase in light hydrocarbons (C_2, C_3) than the Mo

catalyst in the membrane reactor. This gives supporting evidence to the previous suggestion that the pores, where aromatization occurs, are being blocked by carbon formation. It also supports what was expected, but has not yet been confirmed, that there is more Zn deposited on the zeolite surface than within the pores, and that more of the Mo was deposited inside the pores. Additional surface characterization (NH_3-TPD) is planned to examine this hypothesis further.

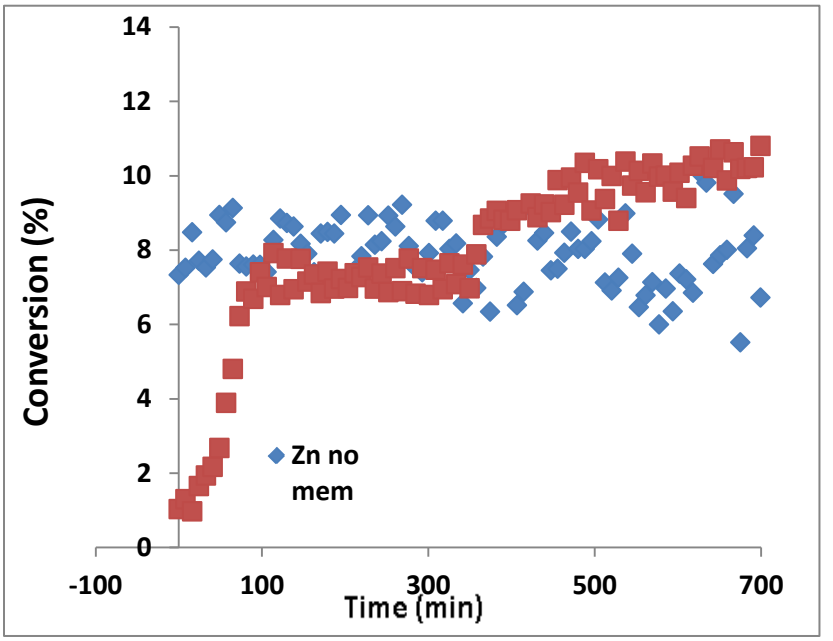

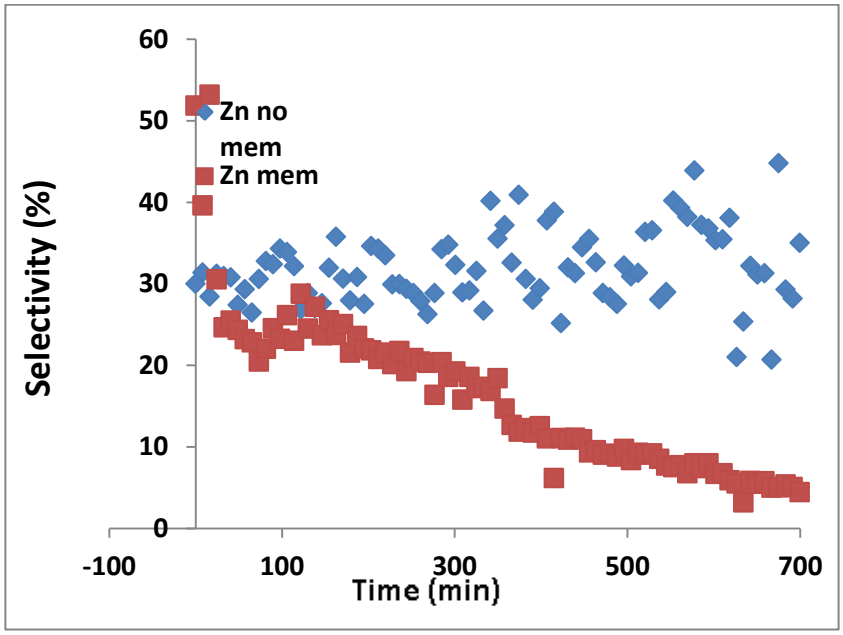

Figure 54: Performance of 3wt% Zn/HZSM-5 catalyst under methane DHA (700°C, 5 atm, 3000 scc/g/hr) with and without Pd membrane: a) Methane conversion, b) Benzene (BZ) selectivity.

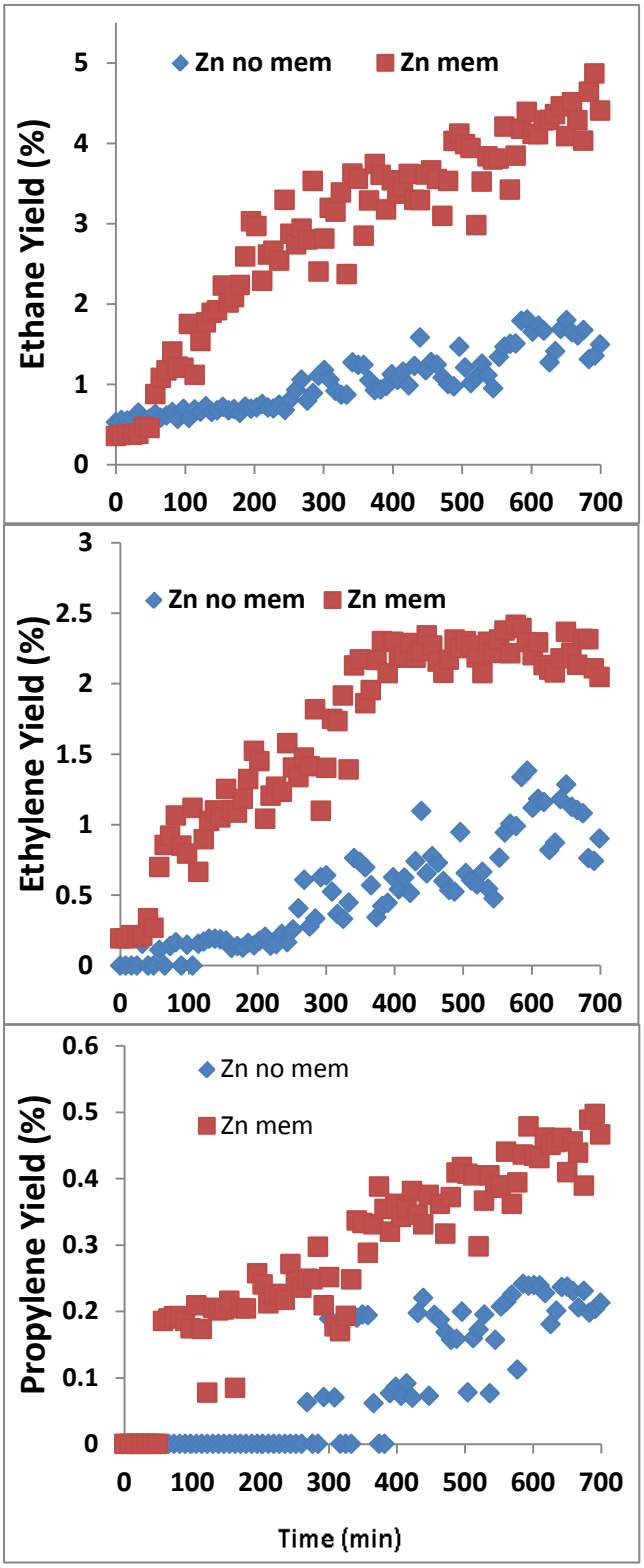

Figure 55: Light hydrocarbon yields with 3wt% Zn/HZSM-5 under methane DHA (700°C, 5 atm, 3000 scc/g/hr) with and without Pd membrane: a) Ethane, b) Ethylene, c) Propylene.

In the literature, it is reported that ZnO catalysts may perform better at lower reaction temperatures using a natural gas feed as opposed to a methane feed. Screening was completed on different conventional ZnO catalysts using simulated natural gas mixture (85% CH_4, 10% C_2H_6, and 5% C_3H_8). The objective was to evaluate ZnO catalysts at lower reaction temperature, using promoter metals to prevent reduction to metallic Zn and help in regeneration, and by adding small amounts of ethane and propane during the reaction to increase the aromatic yield. The tests were conducted at 3000 scc/g_{cat}/hr in a temperature programmed reaction from 500 to 700°C (50°C steps) with a holding time of 3 hr at each temperature. The catalyst was regenerated at 600°C with air to burn all coke formed, and then the second reaction cycle was performed.

Figure 56 shows the raw concentration of benzene (in ppm) obtained from Zn and promoted Zn catalysts. Zn does not perform as well as the promoted Zn catalyst during the second cycle. The addition of promoters helps stabilize the ZnO and minimizes its reduction to metallic Zn, which vaporizes at >600°C. Y and Ce promoters performed the best during both cycles compared to La. Regeneration does not significantly affect the benzene yield even at 700°C. The best performing temperature is 650°C using Y- or Ce-promoted Zn catalyst. These data are in the process of being fully analyzed and future testing will extend reaction times under constant temperature and multiple cycles.

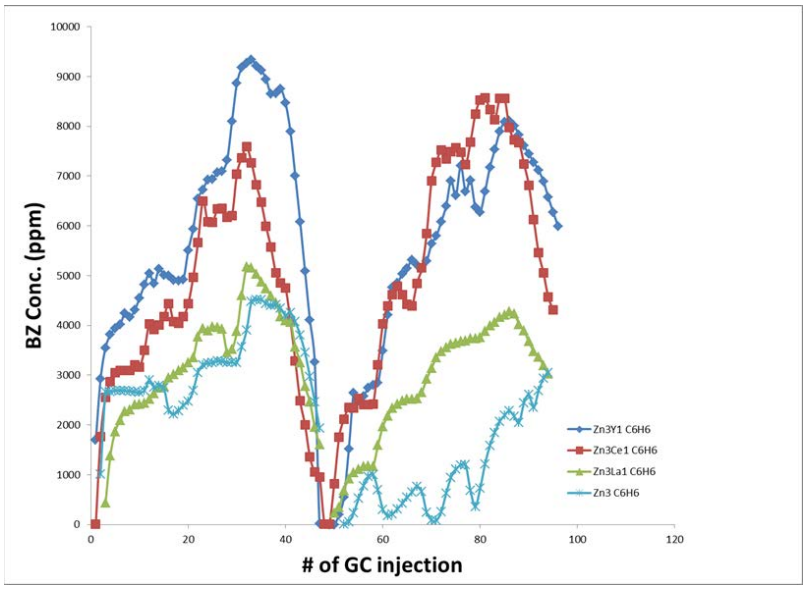

Figure 56: Benzene raw concentration (ppm) formed under different catalysts and temperatures during two reaction cycles.

Major Accomplishments and Key Findings

- A conventional Zn-based catalyst without promoters is not stable at the reaction conditions required for conducting methane DHA reactions. Significant zinc loss was observed after five hours of reaction, resulting in a significant loss of selectivity towards aromatics after the first regeneration cycle. Reduction of ZnO to metallic Zn with subsequent vaporization of metallic zinc is presumably causing this zinc loss. Some preliminary results show that the selectivity to aromatics is maintained through a first regeneration cycle for a Ce- or Y-promoted ZnO catalyst. Additional promoters for ZnO stabilization in zeolite will be explored. Several synthesis methods to incorporate promoters in the catalyst will be applied to enhance the effect of promoters.
- In addition to stabilizing the ZnO on zeolite, promoters might help enhance activity at lower temperatures, which can help reduce Zn loss at elevated temperatures.

- An optimal loading of Zn on zeolite is required for high selectivity to aromatics. A higher loading of Zn resulted in higher methane conversion, but not towards aromatics. Zn presumably anchors to Bronsted acidic sites of ZSM-5, which are also essential for oligomerization of olefins formed in earlier steps. A higher loading of Zn will most likely cover most of the Bronsted acidic sites. Very low selectivity was observed at higher Zn loading (8%). A lower loading of Zn results in lower methane activation for olefin formation, which is a precursor for aromatics. Lower loading will also occupy highly Bronsted acidic sites (in terms of strength), making them unavailable to facilitate the methane decomposition reaction.

Process and Systems Level Assessments

Membrane Reactor Model Development

The third objective of this effort was a comprehensive literature review to compile the required information needed to develop a user-friendly MatLab model of a hydrogen-permeable membrane reactor for the MDHA reaction. The model was designed such that one does *not* need either programming skills or familiarity with MatLab; it only requires the installation of Matlab on the user's computer. A brief explanation of the literature review and the current status of the MatLab model follow.

The broad, long-term objective of this literature review was to compile an exhaustive list of peer-reviewed journal article related to the manufacture of aromatics (specifically benzene, toluene or xylenes) from methane and to critically assess the state-of-the-art. About 260 papers dealing with conventional reactors and hydrogen-permeable membrane reactors have been gathered and are currently being summarized. These papers are being grouped into categories primarily related to the catalyst/support employed for the methane-to-aromatics synthesis, such as Mo/H-ZSM-5, Mo/MFI1, or ZnO/Al_2O_3. The review may be useful for those trying to identify catalysts – if any - that exhibit high selectivity for aromatics, coking resistance in a low H_2 partial pressure environment of a membrane reactor, *and* robustness in the strongly oxidizing environment used to regenerate the catalyst. For example, it is likely that the methane conversions reported for promising catalysts may be low, but it is an aspiration that higher conversions can be realized in a membrane reactor. For that reason catalysts that are selective, robust, and less likely to lead to coke formation will be considered as more promising than catalysts with high short-term conversion that are prone to coke formation that would reduce the permeance of the membrane wall. This review may assist the experimentalists in the selection of the more promising catalysts, and possibly provide them with insights into how to prepare the catalyst/support to prolong its useful life in the membrane reactor.

The short-term utility of the literature review was to provide the team with the technical information required to generate a useful Matlab model of a dehydroaromatization membrane reactor (DHAMR) for the methane-to-benzene+ hydrogen reaction.

For example, the model required the acquisition of papers with accurate expressions for:

- The reaction kinetics associated with a specific catalyst for the methane-to-benzene + hydrogen reaction over a wide temperature range.
- The thermodynamic equilibrium constant for this reversible reaction.
- The hydrogen permeance of various membrane materials.

These results in these papers have been and are currently being implemented into the current version of the MatLab model described in the following section. The literature review is also being used to extract information that will be included in the future version of the MatLab model.

For example:

- The inclusion of C-producing reactions such as methane-to-carbon + hydrogen ($CH_4 \leftrightarrow C + 2H_2$).
- Methods for estimating the effect of C formation on reaction kinetics and membrane permeance.
- Determining the pressure drop on the retentate side through the fixed bed of catalyst particles.

The objective of the MatLab modeling effort is to develop a simple-to-use program that allows the user to enter very basic information about a DHAMR, and to predict the resultant performance of an ideal membrane reactor. The main (and currently only) reaction in the model is the MDHA reaction.

Because the forward gas phase reaction (methane-to-benzene + hydrogen) produces more moles than it consumes, the thermodynamic equilibrium conversion limit is quite low (e.g. 12% at 700 ^{o}C). The ability to remove H_2 from the reaction mixture through the reactor membrane walls allows much higher levels of conversion to be achieved, therefore a hydrogen-permeable membrane is included in the model. An incremental section of the "double-pipe" DHAMR is shown in Figure 57 and Figure 58. On one side of the membrane is a volume packed with catalysts particles and the reaction gas mixture (retentate-side), while the other side provides a volume where the H_2 that diffused through the membrane wall can be removed (permeate side).

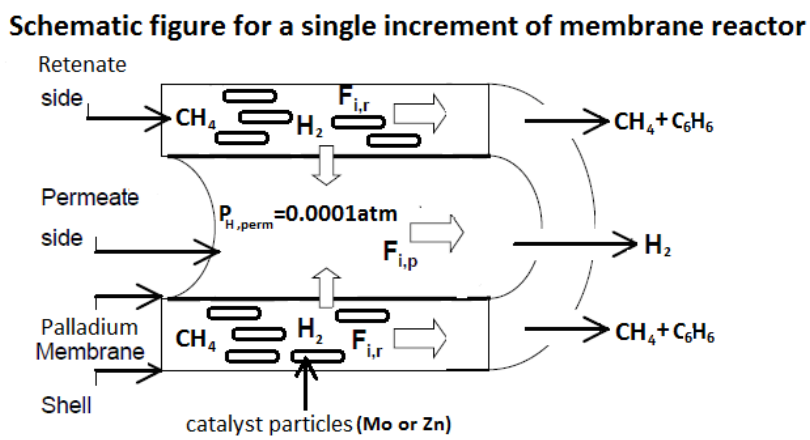

Figure 57: DHAMR increment for a reactor with catalyst particles/retentate-side on the "shell" side with an example value of the low partial pressure of hydrogen on the permeate/tube side.

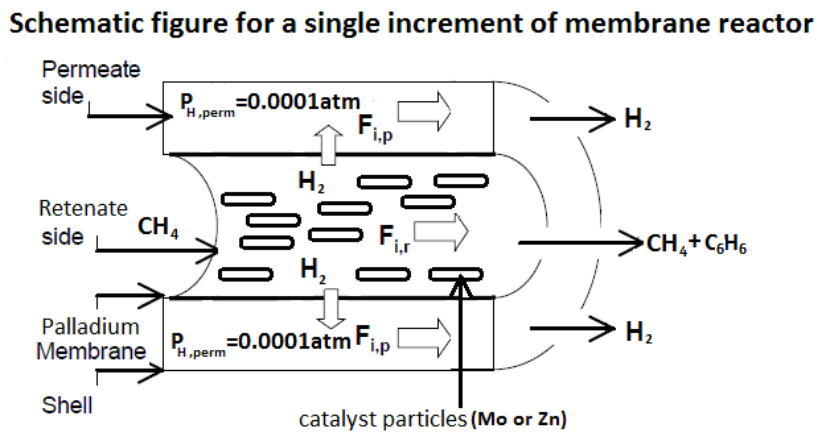

Figure 58: DHAMR increment for a reactor with catalyst particles/retentate on the "tube" side with an example value of the low partial pressure of hydrogen on the permeate side/shell.

Upon running the program (which does not require a prior knowledge of MatLab or programming), the user is prompted to enter the following information either as a number or as a selection from a menu: location of catalyst, reactor length, reactor OD, reactor ID, membrane material, membrane thickness, catalyst, porosity of the catalyst bed, literature reference for the rate expression associated with the catalyst, feed rate of methane, temperature, retentate pressure, and approximate partial pressure of H_2 in the permeate.

The output of the model includes tables of numbers and plots describing the maximum equilibrium conversion of methane in a non-membrane reactor, methane conversion as a function of reactor length, hydrogen flux as a function of reactor length, concentrations of CH_4, C_6H_6, and H_2 in the retentate as a function of reactor length, the retentate-side outlet flow rates of CH_4, C_6H_6, and H_2, the permeate-side outlet flow rate of H_2, and a mass balance on C, H and O for the entire reactor. Examples of the output are illustrated in Figure 59 (a conventional reactor) and Figure 60 (a palladium membrane reactor that is operating at identical conditions as the conventional reactor) for the Mo/HZSM-5 catalyst based, with reaction kinetics described by Yao, et al., 2008 [1] and Pd permeability described by Morreale and NETL co-workers (2003) [2].

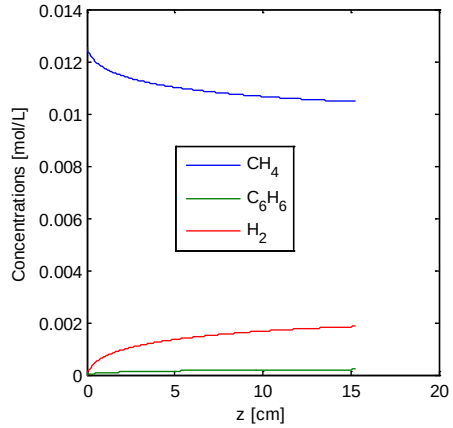

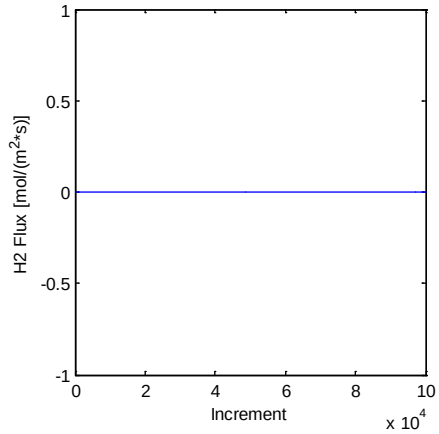

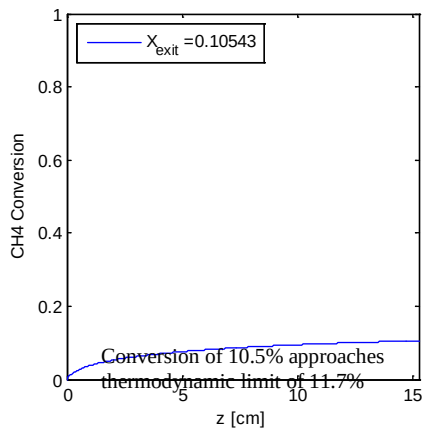

	Input [g/min]	Output [g/min]	Diffusion [g/min]
CH4	0.0148	0.0133	0
C6H6	0	0.0013	0
H2	0	2.9516e-04	0
Total	0.0148	0.0149	0

	Input [mol/min]	Output [mol/min]	Diffusion [mol/min]
CH4	9.2581e-04	8.2820e-04	0
C6H6	0	1.6268e-05	0
H2	0	1.4641e-04	0
	0	0	0

	C Error [g]	H Error [g]
	1.7347e-17	8.6736e-18

Figure 59: Reactor model predictions for converstion and benzene production using a conventional reactor (no hydrogen removal by membrane).

A second iteration of the model, where significant hydrogen removal by a Pd membrane is input into the parameters (Figure 60, top right), predicts a significant increase in both methane conversion and benzene production. This iteration mimics that which would be predicted for shifting the equilibrium toward product formation, in contrast with the above example.

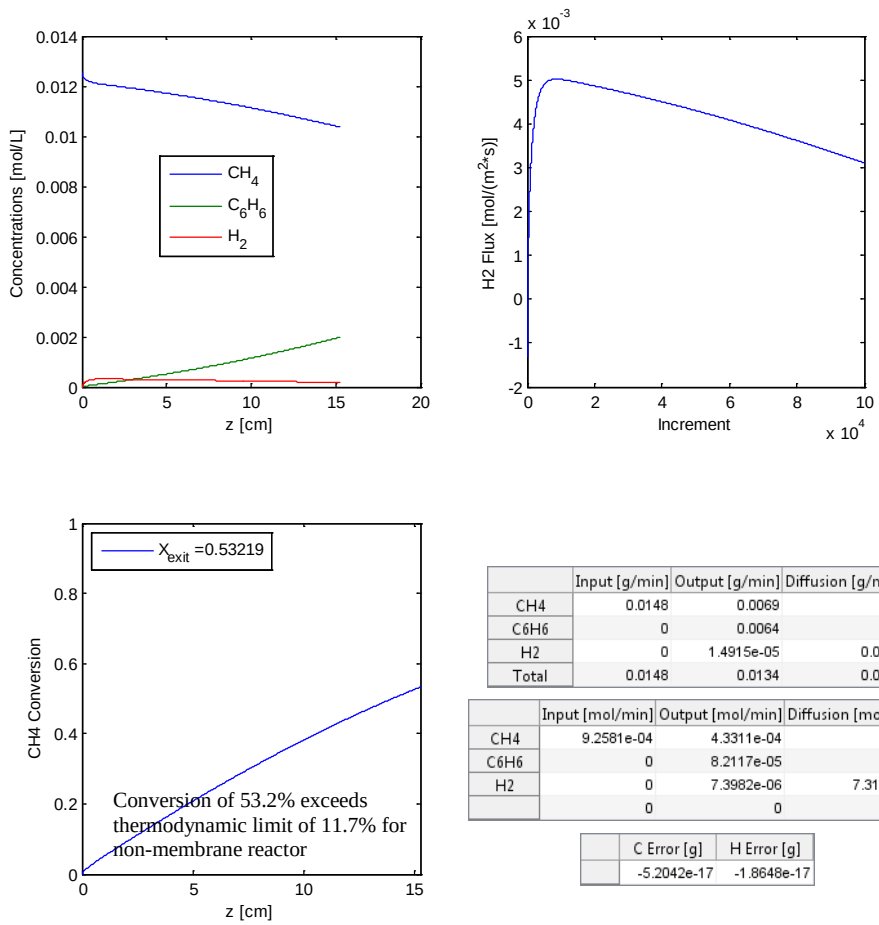

	Input [g/min]	Output [g/min]	Diffusion [g/min]
CH4	0.0148	0.0069	0
C6H6	0	0.0064	0
H2	0	1.4915e-05	0.0015
Total	0.0148	0.0134	0.0015

	Input [mol/min]	Output [mol/min]	Diffusion [mol/min]
CH4	9.2581e-04	4.3311e-04	0
C6H6	0	8.2117e-05	0
H2	0	7.3982e-06	7.3166e-04
	0	0	0

	C Error [g]	H Error [g]
	-5.2042e-17	-1.8648e-17

Figure 60: Reactor model predictions for conversion and benzene production using significant hydrogen removal from reaction product suite using a 125 micron thick Pd membrane.

This MatLab model is *not* meant to compete with or replace CFD models of membrane reactor units, nor is it intended to accurately predict the actual performance of real membrane reactor units.

Rather its utility is to provide a single predictive tool that incorporates the most crucial aspects of a DHAMR to answer questions such as these:

- What is the highest conversion expected in a conventional reactor?
- How much more conversion can be achieved in a membrane reactor?
- Is there a significant increase in performance if the membrane thickness is reduced from 100 to 10 to 1 microns?
- How low of a partial pressure of H_2 must be maintained in the permeate to get high conversion?
- Should the DHAMR be operated at very high pressure on the retentate side?
- Should low temperature catalysts be considered even if no coking occurs, or is the rate simply too low?

The MatLab model can also be used to simulate experiments conducted in the NETL labs.

Although precise agreement is not expected, the model predictions and experimental results can be compared to answer questions such as these:

- Based on a comparison of reactions in a conventional reactor and a membrane reactor, does it appear that the membrane is allowing the expected amount of hydrogen to diffuse into the permeate? Or does it appear the membrane is barely working, perhaps due to coking?
- Is it worth the time exploring temperatures 50 ^{o}C higher than the current maximum temperature, or would the resultant increase in conversion be relatively insignificant?
- Based on previously published literature for the exact same catalyst, are the expected levels of conversion being observed?

3.0 Conclusion

Work efforts during FY13 led to advancement of knowledge base in several key areas. Hydrogen separation efforts elucidated potential corrosion-resistant binary and ternary alloys as a function of temperature. Further, lab facilities were improved to explore the significance of additional contaminants such as As and Se on separation materials. This tool will allow for controlled studies of materials in conditions that may be more representative of syngas compositions.

Catalyst development efforts, from a fundamental scale and experimental scale, made several key determinations for understanding the physical nature and reactivity of metal-zeolite conversion catalysts for use in methane DHA reactions. These include the non-random nature of Al substitution sites in the zeolite and their potential effect on reactivity, the potential for promoters to increase the stability of Mo-based zeolite catalysts, as well as the importance of exploring different metal cations (such as Zn) as replacements for the oft-studied Mo catalysts. Further, efforts to synthesize a new type of catalyst material where the active metal is a nanoparticulate embedded within the pore structure of ZSM-5 were successful and produced the world's first Zn@ZSM-5 catalyst.

Reaction modeling and testing using hydrogen removal to increase the rate of DHA reaction also experienced successes. Modeling efforts were able to demonstrate using simulations what magnitude of conversion increases are obtainable given a certain hydrogen removal rate. At the same time, experimental efforts using a membrane reaction system were able to show both qualitative and quantitative effects of hydrogen removal on methane conversion, benzene production, and catalyst lifetime.

4.0 Technology Transfer

Presentations

Abdelsayed, V., Smith, M., Shekhawat, D., Natesakhawat, S., Cheng, Y., Link, D., Morreale, B. "Methane Dehydroaromatization over Mo and Zn Based Catalysts in Membrane Catalytic Reactor," Abstract submitted to the 2014 Spring AIChE Conference.

Doğan, Ö.N., "Materials Development for Fossil Fueled Energy Conversion Systems," Materials Science Seminar, Washington State University, Pullman, WA, February 22, 2013.

Doğan, Ö.N., Nielsen, B.C, and Howard, B., "Corrosion of Membrane Materials for Hydrogen Separation from Coal-Derived Syngas," TMS 142nd Annual Meeting & Exhibition, San Antonio, TX, March 3-7, 2013.

Nielsen, B., Doğan, Ö.N., and Nall, E., "Corrosion of Cu-Pd and Cu-Pd-M (M=Y or Mg) Hydrogen Separation Membrane Alloys in Simulated Syngas Containing H_2S," Proceedings of the International Pittsburgh Coal Conference, Pittsburgh, PA, October 15-18, 2012.

Publications

Doğan, Ö.N., Gao, M.C., and Hu, R., "Microstructure and Corrosion Behavior of the Cu-Pd-M Ternary Alloys for Hydrogen Separation Membranes," *Materials Challenges in Alternative & Renewable Energy II: Ceramic Transactions*, 239, 2013, p169-79.

Doğan, Ö.N., Howard, B.H., Ciocco, M., and Gao, M.C., "Structure and Hydrogen Transport Properties of a Cu-Pd-Mg Membrane Alloy," in preparation.

Doğan, Ö.N., Nall, E., and Gao, M.C., "Cu-Pd-Mg Ternary System - First Principles Calculations and Experiments," in preparation.

Doğan, Ö.N., Nielsen, B.C., and Hawk, J.A., "Elevated-Temperature Corrosion of $CoCrCuFeNiAl_{0.5}B_x$ High-Entropy Alloys in Simulated Syngas Containing H_2S," *Oxidation of Metals*, 80 (2013) 177-190.

Howard, B., Doğan, Ö.N., and Nielsen, B., "Effect of Real Syngas on the Membrane Alloys," in preparation.

Gao, M.C., Ouyang, L., and Doğan, Ö.N., "First-Principles Screening of B2 Stabilizers in CuPd-based Hydrogen Separation Membranes: (1) Substitution for Pd," *Journal of Alloys and Compounds*, 574, 2013, p368-76.

Nielsen, B., Doğan, Ö.N., Howard, B. H., and Nall, E., "Comparison of the Corrosion of $Cu_{50}Pd_{50}$ and $Cu_{50}Pd_{44}M_6$ (M=Y, Mg, or Al) Hydrogen Separation Membrane Alloys in Simulated Syngas Containing H_2S," *Corrosion Science* 76 (2013) 170-181.

Nielsen, B, Doğan, Ö.N., Nall, E., and Howard B.H., "Elevated Temperature Corrosion of Pd and Cu-Pd alloys in Simulated Syngas Containing H_2S," in preparation.

Tafen, D.N., Miller, J.B., Doğan, Ö.N., Baltrus, J., and Kondratyuk, P., "Oxygen-Induced Y Surface Segregation in CuPdY Ternary Alloy," *Surface Science*, 608, 2013, p61-66.

Tafen, D.N., Miller, J.B., Doğan, Ö.N., Howard B.H., and Baltrus, J., "Surface Segregation in Cu_8Pd_7Mg" in preparation.

5.0 References

1. Yao, B, Chen, J, Liu, D, Fang, D, Intrinsic Kinetics Of Methane Aromatization under Non-Oxidative Conditions over Modified Mo/HZSM-5 Catalysts, *Journal of Natural Gas Chemistry*, 17(2008) 64-68.

2. Morreale, B.D., Ciocco, M.V., Enick, R.M., Morsi, B.I., Howard, B.H., Cugini, A.V., and Rothenberger, K.S., "The Permeability of Hydrogen in Bulk Palladium at Elevated Temperatures and Pressures," *Journal of Membrane Science*, 212, 2003, p87-97.

The National Energy Technology Laboratory (NETL) conducts cutting-edge energy research and technology development and analyzes energy systems and international energy issues for the U.S. Department of Energy. The NETL Regional University Alliance (NETL-RUA) is an applied research collaboration that combines NETL's energy research expertise with the broad capabilities of five nationally recognized, regional universities: Carnegie Mellon University (CMU), The Pennsylvania State University (Penn State), University of Pittsburgh (Pitt), Virginia Tech, and West Virginia University (WVU), and the engineering and construction expertise of an industry partner (URS). NETL-RUA leverages its expertise with current fossil energy sources to discover and develop sustainable energy systems of the future, introduce new technology, and boost economic development and national security.

Jared Ciferno
Director
SCC, Office of Coal and Power R&D
DOE-NETL

Robert Romanosky
Deputy Director
SCC, Office of Coal and Power R&D
DOE-NETL

Shailesh Vora
Technology Manager, Fuels
SCC, Office of Coal and Power R&D
DOE-NETL

Cynthia Powell
Director, ORD
DOE-NETL

Timothy McNulty
Associate Vice-President for Government Relations, CMU

Neil Sharkey
Interim Vice President for Research, Penn State

Mark Redfern
Vice Provost for Research, Pitt

Robert Walters
Vice President for Research, Virginia Tech

Fred King
Vice President for Research and Economic Development, WVU

Kevin Donovan
RES Program Manager, URS Corporation